The Astrophysical Journal, 828:33, 2016 September 1
Preprint typeset using LaTeX style emulateapj v. 01/23/15

arXiv:1606.08088v2 [astro-ph.EP] 29 Aug 2016

IN SITU AND EX SITU FORMATION MODELS OF KEPLER 11 PLANETS

Gennaro D'Angelo[1,2] and Peter Bodenheimer[3]

The Astrophysical Journal, 828:33, 2016 September 1

ABSTRACT

We present formation simulations of the six Kepler 11 planets. Models assume either *in situ* or *ex situ* assembly, the latter with migration, and are evolved to the estimated age of the system, ≈ 8 Gyr. Models combine detailed calculations of both the gaseous envelope and the condensed core structures, including accretion of gas and solids, of the disk's viscous and thermal evolution, including photo-evaporation and disk-planet interactions, and of the planets' evaporative mass loss after disk dispersal. Planet-planet interactions are neglected. Both sets of simulations successfully reproduce measured radii, masses, and orbital distances of the planets, except for the radius of Kepler 11b, which loses its entire gaseous envelope shortly after formation. Gaseous (H+He) envelopes account for $\lesssim 18\%$ of the planet masses, and between ≈ 35 and $\approx 60\%$ of the planet radii. In situ models predict a very massive inner disk, whose solids' surface density (σ_Z) varies from over 10^4 to $\approx 10^3\,\mathrm{g\,cm^{-2}}$ at stellocentric distances $0.1 \lesssim r \lesssim 0.5$ au. Initial gas densities would be in excess of $10^5\,\mathrm{g\,cm^{-2}}$ if solids formed locally. Given the high disk temperatures ($\gtrsim 1000$ K), planetary interiors can only be composed of metals and highly refractory materials. Sequestration of hydrogen by the core and subsequent outgassing is required to account for the observed radius of Kepler 11b. Ex situ models predict a relatively low-mass disk, whose initial σ_Z varies from ≈ 10 to $\approx 5\,\mathrm{g\,cm^{-2}}$ at $0.5 \lesssim r \lesssim 7$ au and whose initial gas density ranges from $\approx 10^3$ to $\approx 100\,\mathrm{g\,cm^{-2}}$. All planetary interiors are expected to be rich in H_2O, as core assembly mostly occurs exterior to the ice condensation front. Kepler 11b is expected to have a steam atmosphere, and H_2O is likely mixed with H+He in the envelopes of the other planets. Results indicate that Kepler 11g may not be more massive than Kepler 11e.

Keywords: Planetary systems – Planets and satellites: formation – Planets and satellites: individual (Kepler 11) – Planets and satellites: interiors – Protoplanetary disks – Planet-disk interactions

1. INTRODUCTION

Numerous planetary systems have been discovered that consist of two or more planets with masses of a few Earth masses ($M_\oplus$), orbiting in the same plane within 0.5 au of the central star (e.g. Figueira et al. 2012; Mullally et al. 2015). Some properties of such systems are reviewed by Winn & Fabrycky (2015). A particularly well-studied example is the Kepler 11 system, with a central solar-type star (age $8.5^{+1.1}_{-1.4}$ Gyr) and six orbiting planets with semi-major axes ranging from 0.091 to 0.466 au. Their radii, measured through transit observations from the *Kepler* spacecraft, are 1.80–4.19 Earth radii ($R_\oplus$), placing them in the super-Earth/sub-Neptune size range. Estimates of their masses have been obtained from transit timing measurements (Lissauer et al. 2013, hereafter L13); for the five inner planets, the values range from 1.9 to 8.0 $M_\oplus$ (see also Borsato et al. 2014; Hadden & Lithwick 2014). All of these inner planets have densities that are substantially less than that of a rocky planet, implying that they could each be composed of a heavy-element core surrounded by a gaseous envelope. In the cases of planets c, d, e, and f, these envelopes are most likely composed of hydrogen and helium, in roughly solar proportions, while Kepler 11b's envelope could be composed either of H+He or H_2O steam (Lopez et al. 2012; L13). The estimated mass fractions of these envelopes range from 0.5% in the case of Kepler 11b to 15.7% for Kepler 11e (L13, see also Lopez et al. 2012). However, their volumes are substantial and play an important role in determining the observed planet radii.

One of the main issues pertinent to the understanding of this system is the formation history of the planets. While it is generally assumed that these planets formed by core-nucleated accretion (Safronov 1969), the formation location is not well established. Several studies have proposed that planets in systems of this type formed in situ (e.g., Hansen & Murray 2012, 2013; Ikoma & Hori 2012; Chiang & Laughlin 2013; Tan et al. 2015) and analytic estimates of the envelope-to-core mass ratio in the relevant mass range have also been made (Lee & Chiang 2015; Ginzburg et al. 2016). Other simulations support the alternative *ex situ* assumption, that is, that the planets formed farther out in the disk and, during or after formation, migrated inward to their present positions through interactions with the protoplanetary disks (e.g., McNeil & Nelson 2010; Rogers et al. 2011; Lopez et al. 2012; Mordasini et al. 2012; Bodenheimer & Lissauer 2014; Hands et al. 2014; Chatterjee & Ford 2015). The physical mechanisms involved in the process of orbital migration via disk-planet tidal interactions are reviewed by Kley & Nelson (2012) and Baruteau et al. (2014, pp. 667-689).

While the in situ model has been favored because the terrestrial planets in the solar system presumably formed in this way, the migration (or ex situ) model has been favored because of the difficulties in forming planets in situ in the very inner regions of disks (Bodenheimer et al. 2000), well inside the orbit of Mercury in the solar system. However, a significant argument against the ex situ picture is that in a multiple system, if the planets had undergone convergent migration, they would be expected to have been captured into mean-motion resonances (e.g., Lissauer et al. 2011a), while in fact most of the systems observed by Kepler do not appear to be in resonance. Goldreich & Schlichting (2014)

[1] NASA Ames Research Center, MS 245-3, Moffett Field, CA 94035, USA (gennaro.dangelo@nasa.gov)
[2] SETI Institute, 189 Bernardo Avenue, Mountain View, CA 94043, USA
[3] UCO/Lick Observatory, University of California, Santa Cruz, CA 95064, USA (peter@ucolick.org)

discuss a mechanism, involving an instability in resonances, that would allow the planets to move through resonances; therefore, migration is not ruled out. Deck & Batygin (2015) revisit this problem and conclude that although the instability in resonances is indeed possible, the time spent by a planet pair in resonance exceeds by a considerable amount the time during which the planets are out of resonance. Thus, they argue that the Goldreich & Schlichting process does not solve the problem that most Kepler planet pairs are not in resonance. However, there are other mechanisms that could move planets out of resonance, including dissipative effects (Delisle et al. 2012; Lithwick & Wu 2012; Batygin & Morbidelli 2013), stochastic effects during migration (Rein 2012), tidal effects caused by planet-wake interactions (Baruteau & Papaloizou 2013) and the effects of small eccentricities in the planetary orbits (Batygin 2015). Moreover, the highly complex orbital architecture of compact multiple systems, as in the case of Kepler 11, may indeed require a migration-based formation scenario (Migaszewski et al. 2012). Nevertheless, there are still many other uncertainties in the theory of planet-disk interactions, as discussed in more detail by Chiang & Laughlin (2013) and Kley & Nelson (2012), leading to legitimate questioning of whether the theoretical processes of planet formation with migration can explain the mass distribution as well as the orbital period distribution of super-Earth/sub-Neptune planets (Howard et al. 2010).

On the other hand, there are several difficulties with the picture of in situ formation of super-Earths/sub-Neptunes. First, even if the planets did form by this process, they still would be subject to orbital decay. If migration is included in simulations of in situ super-Earth formation (Ogihara et al. 2015), the semi-major axis distribution of planets does not agree with the distribution observed by Kepler. Agreement is possible only if orbital migration is suppressed. Second, for the specific case of the Kepler 11 system, a very high surface density of solid material in the inner disk is required, well above that of the minimum-mass solar nebula and even above that of minimum-mass extrasolar nebulae (Chiang & Laughlin 2013; Schlichting 2014). This problem may be alleviated if it is assumed that solid material migrates inwards from the outer disk, in the form of either protoplanetary cores (Ward 1997), planetesimals (Hansen & Murray 2012), or small pebbles (Tan et al. 2015), and collects at the appropriate locations. Third, Kepler data show an excess of planet pairs just exterior of the 2:1 and 3:2 mean-motion resonances, compared to the pairs just interior to these resonances (Lissauer et al. 2011b; Fabrycky et al. 2014; Chatterjee & Ford 2015), which is not easily accountable by in situ formation. Fourth, it has often been assumed that in the inner disk the temperatures are too high for an appreciable concentration of solid material to exist. In fact, the simple assumption that the ratio of sound speed to orbital speed, i.e., the ratio of disk scale height to radial distance, H/r, is 0.03 at 0.15 au gives a temperature of about 1500 K for a solar-mass central star. However, this objection is not necessarily significant. Many disk models give cooler temperatures at 0.1–0.4 au. The evolving two-dimensional models of Dodson-Robinson et al. (2009) give mid-plane temperatures in the inner disk of about 1000 K at an age of 10^5 years, with cooling at later times. The models of Chiang & Goldreich (1999) give even cooler temperatures in the disk interior at these distances.

This paper considers all the observed planets in the Kepler 11 system and asks whether they formed in situ or ex situ, i.e., including orbital migration. In spite of the difficulties mentioned above, both of these possibilities remain viable options. Detailed formation and evolution models are numerically simulated for both scenarios with the same or very similar physical assumptions used in the construction of the planet models. In both cases, the simulations are advanced to an age of 8 Gyr, where the computed masses, radii, and semi-major axes are compared with observations. The general physical and numerical aspects of the calculations are reported in Section 2. The in situ and ex situ models are presented, respectively, in Section 3 and 4 while results are discussed in Section 5. The conclusions are drawn in Section 6.

Table 1
List of Symbols

Symbol	Definition
M_c	Planet's condensed core mass; Section 2.1
R_c	Planet's condensed core radius; Section 2.1
$R_{\rm A}$	Accretion radius; Equation (1)
$R_{\rm B}$	Planet's Bondi radius; Equation (1)
$R_{\rm H}$	Planet's Hill radius; Equation (1)
L_p	Planet total luminosity; Equation (2)
$T_{\rm eff}$	Planet effective temperature; Equation (2)
R_p	Planet radius; Equation (2)
M_p	Planet mass; Equation (3)
$\kappa_{\rm R}$	Rosseland mean opacity; Equation (3)
P	Pressure; Equation (3)
$T_{\rm eq}$	Irradiation equilibrium temperature; Equation (4)
$T_\star$	Stellar effective temperature; Equation (5)
$R_\star$	Stellar radius; Equation (5)
a	Planet orbital radius; Equation (5)
M_e	Planet's gaseous envelope mass; Section 2.1
$\dot{M}_e$	Planet's mass accretion rate of gas; Section 2.1
$\dot{M}_c$	Planet's mass accretion rate of solids; Equation (6)
σ_Z	Disk's surface density of solids; Equation (6)
Ω	Orbital frequency; Equation (6)
F_g	Gravitational enhancement factor; Equation (6)
$M_\star$	Stellar mass; Equation (7)
$L_\star$	Stellar luminosity; Section 2.3
$\dot{M}_e^{\rm iso}$	Gas mass-loss rate during isolation; Equation (8)
$F_{\rm XUV}$	XUV radiation flux during isolation; Equation (8)
$R_{\rm XUV}$	XUV radiation absorption radius; Equation (8)
ε	XUV absorption efficiency; Equation (8)
r	Stellocentric distance; Equation (9)
Σ	Disk's surface density of gas; Equation (9)
$\mathcal{T}$	Gravitational torque; Equation (9)
$\mathcal{T}_\nu$	Viscous torque; Equation (9)
ν	Gas kinematic viscosity; Equation (10)
T	Temperature; Equation (14)
$T_{\rm irr}$	Irradiation temperature; Equation (15)
H	Disk scale height; Equation (16)
$\dot{M}_{\rm scat}$	Scattering rate of solids; Equation (18)
$\dot{\Sigma}_{\rm pe}$	Disk photo-evaporation rate; Equation (23)
$r_{\rm crt}$	Critical radius for photo-evaporation; Section 2.6

2. NUMERICAL PROCEDURES

In this section, we outline the numerical methods applied in the models presented herein, highlighting major differences between in situ and ex situ calculations. As a reference, Table 1 contains a list of some of the symbols used in the paper and the equation in which they appear or the section in which they are first mentioned (physical constants are omitted). In order to simplify labels, some quantities apply to both the disk and the planet, e.g., T for gas temperature or $\kappa_{\rm R}$ for the Rosseland mean opacity, and shall be distinguished by the context in which they are used.

2.1. *Envelope Structure Calculation*

The calculation of the structure and evolution of the planetary gaseous envelope is based on the assumption that the envelope is spherically symmetric around its center and evolves through states of hydrostatic equilibrium (e.g., Kippenhahn et al. 2013). The envelope lies on a core of condensed matter, whose total mass M_c and radius R_c are both functions of time. The core radius is determined as explained below. The envelope structure is calculated by solving the equations for mass conservation, hydrostatic equilibrium, energy conservation, and radiation diffusion (see Bodenheimer & Pollack 1986). The energy equation includes heating produced by in-falling planetesimals, the work done by gravity, cooling from the release of internal heat, and heating by stellar radiation (when applicable). In convective unstable shells, where the radiative temperature gradient exceeds in magnitude the adiabatic gradient (Kippenhahn et al. 2013), the actual gradient of temperature is set equal to the adiabatic gradient.

The chemical composition of the envelope gas is assumed to be uniform, with hydrogen and helium mass fractions $X = 0.74$ and $Y = 0.24$, respectively. The equation of state for this gas mixture is that computed by Saumon et al. (1995), which accounts for the partial degeneracy of electrons and for non-ideal effects in the gas. (Strictly speaking, this equation of state neglects heavier elements and uses $Y = 1 - X$.)

The envelope opacity arises from the combined contributions of dust, atoms, and molecules. Dust opacities are calculated as described in D'Angelo & Bodenheimer (2013), assuming the presence of a number of different grain species, and grain size distributions with a minimum radius of 0.005 μm and a maximum radius of 1 or 10 mm. The number density of dust grains is proportional to the -3 power of the grain radius. Low-temperature gas opacities are taken from Ferguson et al. (2005), whereas high-temperature gas opacities are taken from the OPAL tables (Iglesias & Rogers 1996). Figure 1 illustrates the Rosseland mean opacity for the two grain size distributions considered here, along with gas opacity. Dust grains are supposed to be present in the envelope only if solids are supplied via gas and/or planetesimal accretion. In the absence of a steady supply, dust grains quickly sediment to deeper layers and evaporate. When this happens, i.e., during phases of zero gas and solids' accretion, low-temperature opacities are replaced with the molecular opacities of Freedman et al. (2008).

The planetary evolution code is largely the same as that used by Pollack et al. (1996), Bodenheimer et al. (2000), Hubickyj et al. (2005), and Lissauer et al. (2009). The structure equations are solved by means of the Henyey method (e.g., Bodenheimer et al. 2006), supplemented with boundary conditions at the core-envelope interface, R_c, and at the top of the envelope, R_p. At R_c, the mass is set equal to M_c and the luminosity is set to zero (i.e., there is no energy flux through the core-envelope interface, see the discussion in Bodenheimer & Lissauer 2014). The planet radius, R_p, is assumed to have an upper bound R_A, the accretion radius, defined by

$$\frac{1}{R_A} \equiv \frac{4}{R_H} + \frac{1}{R_B}, \quad (1)$$

where R_H and R_B are the Hill and Bondi radius, respectively. The limiting envelope radii, $R_A \approx R_H/4$ and $R_A \approx R_B$, were estimated from first principles by means of three-dimensional (3D) calculations of the flow dynamics around planets in disks (Lissauer et al. 2009; D'Angelo & Bodenheimer 2013).

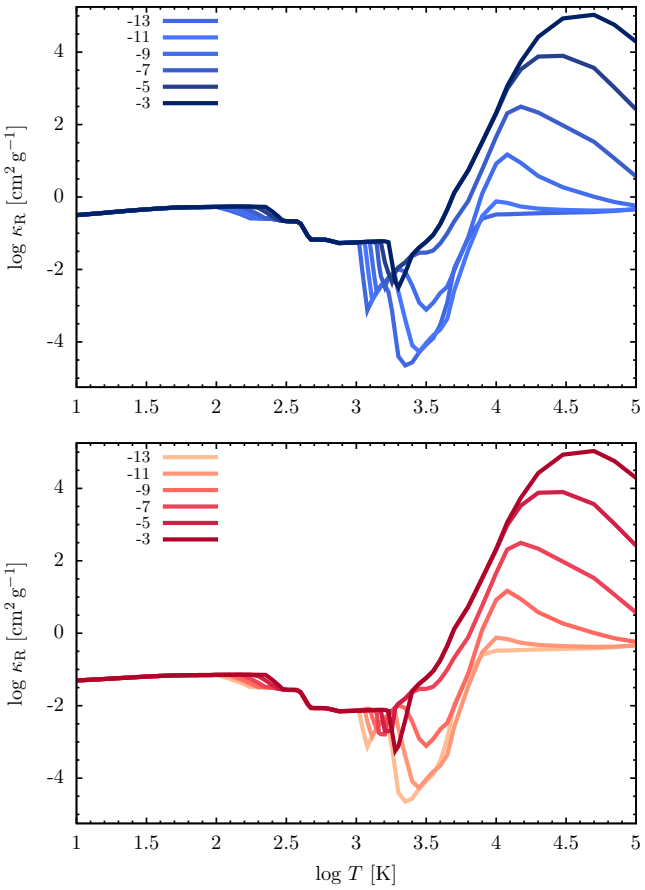

Figure 1. Rosseland mean opacity versus temperature applied in the envelope, when there is a supply of dust grains (via accretion of gas and/or solids), for various gas densities (the legends refer to the logarithm of ρ in g cm^{-3}). The distribution of grains has a minimum radius of 0.005 μm and a maximum radius of 1 (top) and 10 mm (bottom). The gas-to-dust mass ratio is 71.5.

At early stages of evolution, the planet is "in contact" with the disk (the so-called *nebular* stage), and the density and temperature at the top of the envelope are taken as the local disk values. During the nebular stage, gas is added to the envelope in order to restore the condition $R_p \approx R_A$ (see Pollack et al. 1996). Once this condition can no longer be maintained, the envelope contracts inside R_A, entering a *transition* stage, which coincides with the run-away gas accretion phase if the gas accretion rate is sufficiently large. In fact, the gas accretion rate of the envelope, $\dot{M}_e$, is limited by the maximum rate at which the disk can deliver gas to the planet's vicinity. If tidal perturbations by the planet are negligible, the disk-limited accretion rate can be described in terms of simple analytical arguments (D'Angelo & Lubow 2008). If tidal perturbations are not negligible, the problem becomes highly complex and depends on the interplay among viscous torques, tidal torques, and close-range flow dynamics around the planet. Disk-limited accretion rates were derived from 3D hydrodynamics high-resolution calculations, as described in Bodenheimer et al. (2013), extending the parameter space covered by the fitting functions reported therein to include a larger disk viscosity range. It is important to stress that $\dot{M}_e$ cannot exceed the disk-limited accretion rate, and there are in-

stances in which this limit sets in during the nebular stage of evolution. The boundary conditions applied at R_p during the transition stage are discussed in Bodenheimer et al. (2000).

Eventually, the disk's gas around the planet's orbit is dispersed, typically via photo-evaporation by stellar radiation, gas supply ceases, and the planet enters the *isolation* stage. Note that the process of gap formation in the disk by tidal torques alone, under typical disk conditions of viscosity and temperature and for planetary masses up to several times Jupiter's mass ($M_{\rm J}$), does not lead to isolation (e.g., D'Angelo & Lubow 2008; Bodenheimer et al. 2013, and references therein). During the isolation stage, standard photospheric boundary conditions are applied at R_p (e.g., Cox 1968)

$$L_p = 4\pi\sigma_{\rm SB} R_p^2 T_{\rm eff}^4 \tag{2}$$

$$\kappa_{\rm R} P = \frac{2}{3}\frac{GM_p}{R_p^2}, \tag{3}$$

where $\sigma_{\rm SB}$ is the Stefan-Boltzmann constant, G is the gravitational constant, and $\kappa_{\rm R}$ and P are, respectively, the photospheric values of the Rosseland mean opacity and pressure. In Equation (2), the luminosity on the left-hand side comprises both the internal power generated by the planet and the re-radiated power that arises from the absorption of stellar radiation. Hence, the planet's effective temperature is given by (Bodenheimer & Lissauer 2014)

$$T_{\rm eff}^4 = T_{\rm int}^4 + T_{\rm eq}^4, \tag{4}$$

where $T_{\rm int}$ depends on R_p and on the luminosity internally generated by the planet. The equilibrium temperature is such that (e.g., Guillot 2010)

$$T_{\rm eq}^4 = \frac{1}{4} T_\star^4 \left(\frac{R_\star}{a}\right)^2 (1 - A_b), \tag{5}$$

which assumes full redistribution of the incident radiation. The albedo A_b is taken as a constant equal to 0.1. In Equation (5), $T_\star$ and $R_\star$ are the effective temperature and the photospheric radius of the star, respectively.

In calculations that allow for orbital migration, a distinction can be made between isolation from the disk's gas and from the disk's solids. Isolation from the planetesimals' disk occurs when the migration speed $da/dt \approx 0$ and $\dot{M}_p = \dot{M}_c + \dot{M}_e \lesssim 0$, or when the solids' surface density at the planet's location becomes very small. Isolation from the solid disk occurs prior to isolation from the disk's gas or shortly thereafter. However, the consequences of this delay are negligible. Thus, when a planet enters the isolation phase, it is basically isolated from both the disk's gas and solids.

During all stages, if $R_p > R_{\rm A}$, mass is gradually removed from the envelope. In a more realistic context, during the nebular and transition stages, an inflated planet would lose unbound mass hydrodynamically, carried away by the surrounding disk flow (D'Angelo & Bodenheimer 2013). This mechanism of mass loss is different from those operating during the isolation stage (see Section 2.3). As a result of gas loss, while M_c is a monotonic function of time, M_e and M_p may not be.

Accretion of solids is treated as in Pollack et al. (1996). All solids accreted by the planet are assumed to sink to the core, in a condensed form, and increment the core mass. As originally derived by Safronov (1969), the accretion rate of solids can be written as

$$\dot{M}_c = \mathcal{S}_{\rm eff}\, \sigma_Z(a) \Omega(a) F_g, \tag{6}$$

where $\mathcal{S}_{\rm eff}$ is the effective cross section for planetesimal capture of the planet, $\sigma_Z(a)$ is the solids' surface density at the planet's orbital radius, a, $\Omega(a)$ is the planet's orbital frequency, and F_g is the ratio of the gravitational to the geometric cross section (Greenzweig & Lissauer 1990, 1992), known as the gravitational enhancement factor. Further details can be found in Pollack et al. (1996, and references therein). The accretion rate in Equation (6) neglects the contribution of the dust entrained in the accreted gas ($\lesssim 1\%$ by mass). The planetesimal radius is assumed to be 100 km, although smaller planetesimals were also tested.

A planetary embryo accreting planetesimals at a fixed orbital radius will deplete an annular region around its orbit of full width about equal to $8\,R_{\rm H}$, at which point the condensed core becomes detached from the planetesimals' disk. In these calculations, the secular evolution of planetesimals is neglected and therefore, once detached, the core reaches its final mass

$$M_c^f \approx \sqrt{\frac{(16\pi a^2 \sigma_Z)^3}{3M_\star}}, \tag{7}$$

which neglects the contribution of the envelope mass to $R_{\rm H}$ and is hence appropriate when $M_p \approx M_c$. The situation is more complex for a migrating planet, since the depletion rate of solids in the disk tends to be initially slower than the migration rate through the disk. Hence, the planet cuts a swathe through the solids' disk, which deepens as $|da/dt|$ reduces, eventually detaching itself. The final mass of the core in this case is more difficult to predict, as it depends on both the accretion and migration history. During the long isolation stage, a planet may be subjected to stochastic impacts, which may alter the core and envelope mass and the planet's orbit if the impactors are sufficiently massive. This possibility is not considered here.

As mentioned above, solids sink to the top of the core. This process releases energy in the envelope, affecting the local energy budget, but not the local chemical composition of the envelope. These calculations consider accretion of hydrated, partly hydrated, and anhydrous planetesimals, depending on the local disk temperature. Rocky planetesimals may reach the core nearly intact if they are large enough (they may be held together by their own gravity) or if the ram pressure does not exceed their compressive strength (D'Angelo & Podolak 2015, and references therein). Ice-rich planetesimals are more easily disrupted or entirely ablated in the envelope because the critical temperature of H_2O is only ≈ 650 K, a value reached in relatively shallow layers of the envelope (their mass is nevertheless assumed to sink to the core).

An important part of the calculation is represented by the capture of planetesimals, which determines self-consistently the cross section $\mathcal{S}_{\rm eff}$ in Equation (6), and by their interaction with the planet's envelope, which determines depth-dependent mass and energy deposition rates. This part is based on the protocols described in Pollack et al. (1996), enhanced with an improved integration algorithm of the planetesimals' trajectories (D'Angelo et al. 2014). In brief, a number of trajectories with a varying impact parameter ($\leq R_p$) are integrated through the envelope. The largest impact parameter for which the body hits the core surface, breaks up, or is entirely ablated provides the radius for planetesimal capture and hence the

cross section $\mathcal{S}_{\rm eff}$. At this point, an additional series of trajectory integrations is performed, with an impact parameter up to the capture radius, to record the ablation history and the fate of the body as a function of the impact parameter. This collective information provides the mean energy and mass deposition rates in each envelope layer.

The methods outlined above apply to both in situ and ex situ calculations. The basic difference is that the boundary conditions at R_p change over time in ex situ models, whereas in situ calculations allow only for a linear decline with time of the gas surface density at R_p. In ex situ models, the surface density σ_Z in Equation (6) also varies as a function of the distance from the star and of the disk temperature. Additionally, ex situ models use stellar properties from stellar structure models of solar-type stars to compute the equilibrium temperature (Equation (5)), the mass-loss rate during isolation (Equation (8)), and the irradiation temperature of the disk (Equation (16)). The calculations apply a stellar model of a solar-mass and protosolar metallicity ([Fe/H]= 0.0, Asplund et al. 2009; Lodders 2010) star from Siess et al. (2000), whose radius, effective temperature, and luminosity are plotted in Figure 2. For comparison, some calculations are repeated by adopting a Yonsei-Yale model (Spada et al. 2013) for a 0.95 $M_\odot$, [Fe/H]= 0.0 star, also represented in Figure 2. In contrast, in situ models are based on fixed, solar-type values for radius, effective temperature, and luminosity of the star.

2.2. *Core Structure Calculation*

In situ formation calculations determine the core radius, R_c, from its current mass, M_c, using tables of results from Rogers et al. (2011). The core is composed of iron and silicates, with Earth-like mass fractions of 30% and 70%, respectively. Applied to an Earth-mass planet, the results predict a radius within 2.9% of the Earth radius, $R_\oplus$. The radius R_c is then used as an inner boundary condition for the H+He envelope.

Ex situ formation calculations allow for accretion of planetesimals whose composition varies as a function of time and distance from the star. At disk temperatures below 150 K, the planetesimals are ice-rich, 50% by mass (45% silicates and 5% iron). They become progressively ice-poor (and rich in silicates and iron) at higher disk temperatures and are anhydrous at temperatures above 250 K (D'Angelo & Podolak 2015), where a terrestrial-type composition is adopted (70% silicates and 30% iron by mass). The mass fractions of iron, silicates, and ice are linearly interpolated in temperature between 150 and 250 K.

Since the composition of the condensed core may vary during the evolution of ex situ models, as the composition of accreted solids changes, detailed calculations of the core structure are performed. The core is assumed to be spherically symmetric about its center and described by the equation of mass conservation and hydrostatic equilibrium (see Appendix A). The core is taken to be fully differentiated into an iron nucleus, a silicate mantle, and an outer shell of condensed H_2O. Two-layer (with any combination of the three materials) or one-layer structures are also possible. Each material is characterized by a "cold" equation of state (EoS) relating density and pressure. We experimented with a combination of Birch-Murnaghan, Vinet, and Generalized Rydberg EoS (for a review, see Stacey & Davis 2008), and extend them to very high pressures by means of the Thomas-Fermi-Dirac theory. Details are given in Appendix A. Temperature effects on the EoS are neglected since thermal pressure is expected to provide only a minor correction to R_c for the core masses considered here (see, e.g., Valencia et al. 2006; Seager et al. 2007; Sotin et al. 2007; Sohl et al. 2014b). However, temperature effects are included to account for phase transitions within the layers (see Appendix A for details). Applying this module to an Earth-mass planet with a composition of 70% silicates and 30% iron by mass, the calculated radius is within 0.1% of $R_\oplus$. For a cold-Earth analog (67.3% silicates and 32.7% iron by mass, Sohl & Schubert 2007, pp. 27-68), the resulting radius is within 0.8% of $R_\oplus$. More detailed structure calculations, including heat transfer and additional material phases, are also presented in Appendix A. They are compared to isothermal core structures in Appendix C.

The integration of the equations proceeds from the center outward, varying the central pressure in an iterative fashion, until the pressure at the core radius, R_c, matches (within 1%) the pressure at the bottom of the envelope, which is provided by the envelope structure module (Section 2.1). The integration of the core structure equations is performed whenever M_c increases by $\geq 1\%$ or if the pressure or temperature at R_c changes by $\geq 10\%$.

2.3. *Radiation-Driven Gas Loss During Isolation*

Removal of envelope gas after the planet becomes isolated, when stellar photons can directly impinge on the planet dayside, is based on the energy-limited hydrodynamics escape driven by stellar X-ray and EUV (XUV) radiation (Watson et al. 1981; Erkaev et al. 2007; Murray-Clay et al. 2009; Lopez et al. 2012). In this limit, the mass-loss rate of the envelope can be approximated as

$$\dot{M}_e^{\rm iso} = \frac{\varepsilon \pi R_{\rm XUV}^2 F_{\rm XUV}}{K(\xi)} \left(\frac{R_p}{G M_p} \right), \qquad (8)$$

where $R_{\rm XUV} \approx 1.1\, R_p$ is the envelope radius at which the atmosphere becomes optically thick to the incoming stellar XUV radiation and most of the flux $F_{\rm XUV}$ is absorbed (Erkaev et al. 2007; Murray-Clay et al. 2009), $K(\xi) = 1 - 3/(2\xi) + 1/(2\xi^3)$ is a reduction factor of the planet's potential energy caused by tidal forces of the star, and $\xi = R_{\rm H}/R_p > 1$ (Erkaev et al. 2007). Escape is assumed to take place at the equipotential surface passing through the collinear Lagrange point L_1. Note that Equation (8) diverges for $\xi \to 1$. During the evolution in isolation, it is assumed that $\dot{M}_e = -\dot{M}_e^{\rm iso}$.

Observations of the histories of EUV and X-ray fluxes of solar-type stars suggest that mass loss is most vigorous at ages of $t < 0.1$ Gyr (Ribas et al. 2005). Here, we set $F_{\rm XUV} = 3 \times 10^{-4} L_\star/(4\pi a^2)$ for $t \lesssim 0.1$ Gyr and $F_{\rm XUV} = 3 \times 10^{-6} (5\,{\rm Gyr}/t)^{1.23} L_\star/(4\pi a^2)$ at later times (Ribas et al. 2005), where $L_\star$ is the stellar bolometric luminosity. The quantity ε is an efficiency factor intended to roughly account for radiative losses from the envelope (Erkaev et al. 2007), so that only a fraction of the incident flux $F_{\rm XUV}$ can effectively drive mass loss. This factor is quite uncertain. These calculations are based on an efficiency of $\varepsilon = 0.1$ (e.g., Murray-Clay et al. 2009; Lopez et al. 2012). However, other values of ε are considered for a sensitivity study.

In situ and ex situ calculations handle radiation-induced mass loss of the envelope in similar ways. The only basic difference is that, in Equation (8) and in the function $K(\xi)$, $R_{\rm XUV}$ replaces R_p in the in situ models. Additionally, the stellar luminosity of ex situ models varies in time, according to the applied stellar evolution model (see Figure 2), whereas in situ simulations use $L_\star = L_\odot$. Since

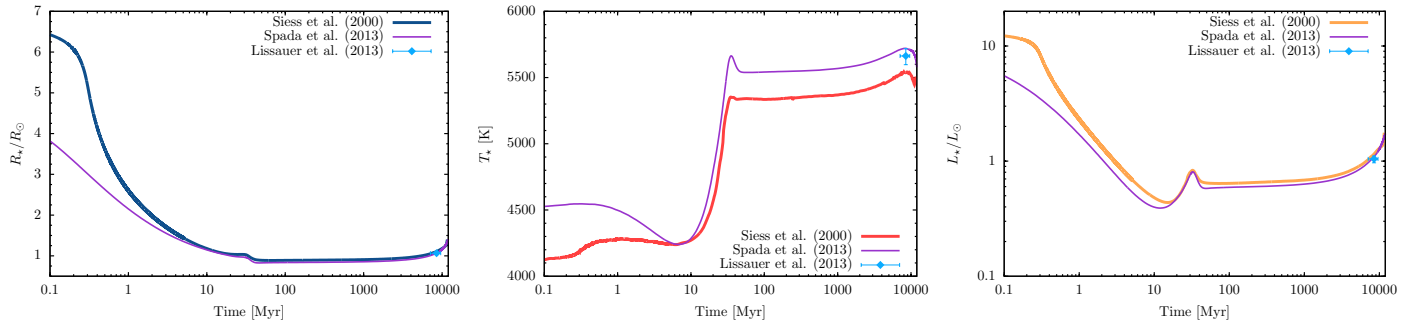

Figure 2. Radius (left), effective temperature (center), and luminosity (right) evolution of the star: thick curves are for a protosolar metallicity ([Fe/H]= 0.0), $1 M_\odot$ stellar model from Siess et al. (2000); thin curves are for a [Fe/H]= 0.0, $0.95 M_\odot$ Yonsei-Yale model from Spada et al. (2013). Estimated age, radius, effective temperature, and luminosity of the host star Kepler 11, from L13, are also shown as points with error bars. Lissauer et al. (2011a) estimated a radius of $R_\star = 1.1 \pm 0.1\, R_\odot$, and effective temperature of $T_\star = 5680 \pm 100$ K, and an age between 6 and 10 Gyr.

the XUV stellar output is assumed to be proportional to $L_\star$, the mass-loss history of the envelope during isolation may differ from that occurring at a constant value of $L_\star$, as used by in situ calculations.

Other mass-loss mechanisms during the beginning of the isolation phase have been considered. Ikoma & Hori (2012) and Ginzburg et al. (2016) studied the effect of loss of pressure support at the planet's outer boundary once the disk's gas disperses; the energy for the mass loss is supplied by the planet's cooling luminosity. Owen & Wu (2016) considered a similar mechanism, initiated by the loss of pressure from the disk, in which a "Parker" wind is driven by a combination of the stellar continuum radiation and the gravitational energy released as the planet contracts. The assumptions made in these works are considerably different from those made here, and it is not clear if these processes would be significant in our models. First, the planet radius in the above papers is implicitly assumed to be close to $R_{\rm B}$, while in the models discussed here, just before disk dispersal, R_p is roughly a factor of ≈ 3 to ≈ 6 smaller than $R_{\rm B}$ (see also Section 3). Second, as the disk disperses, the possible up-lifting of the outer envelope layers due to loss of disk pressure during the nebular stage is implicitly included in the structure calculation through the boundary conditions at R_p. After disk dispersal, the boundary conditions transition to those of an isolated photosphere (Equations (2) and (3)). The transition occurs on the cooling timescale of the outer envelope layers, which is shorter than the disk dispersal timescale. As a result, the photospheric pressure increases and the planet further contracts inside $R_{\rm B}$. The Owen & Wu mechanism, for example, is not significant for $R_p \lesssim 0.1\, R_{\rm B}$. Clearly, whether these wind mechanisms are in fact unimportant in calculations like ours needs to be tested in more detail.

2.4. *Disk Evolution*

These models consider the evolution of an axisymmetric gaseous disk, of surface density Σ, driven by turbulence viscosity ν (of some nature), stellar-induced photoevaporation, tidal torques due to gravitational interactions with an embedded planet, and accretion of gas on the planet. Indicating with $\mathcal{T}_\nu(r)$ the viscous torque acting between two adjacent disk's annuli at a distance r from the star and with $-\mathcal{T}(r)$ the tidal torque exerted by the planet on the disk's gas at radius r, conservation of mass and momentum within the disk leads to the following disk's evolution equation (e.g., Lin & Papaloizou 1986)

$$\pi r \frac{\partial}{\partial t}(\Sigma + \Sigma_{\rm pe} + \Sigma_{\rm ac}) = \frac{\partial}{\partial r}\left\{ \frac{1}{r\,\Omega}\frac{\partial}{\partial r}\left[\mathcal{T}_\nu(r) - \mathcal{T}(r)\right]\right\}, \quad (9)$$

where Ω is the disk's rotation rate, $\dot\Sigma_{\rm pe}$ is gas mass removed by photo-evaporation per unit disk surface and unit time (see Section 2.6), and $\dot\Sigma_{\rm ac}$ is gas mass removed by accretion on the planet per unit disk surface and unit time. Recalling that $\mathcal{T}_\nu = -2\pi r^3 \nu \Sigma\, \partial\Omega/\partial r$ (Lynden-Bell & Pringle 1974) and approximating Ω to the Keplerian rotation rate $\sqrt{GM_\star/r^3}$, the viscous torque becomes $\mathcal{T}_\nu = 3\pi r^2 \nu \Sigma \Omega$ and Equation (9) assumes the more familiar form

$$r\frac{\partial}{\partial t}(\Sigma + \Sigma_{\rm pe} + \Sigma_{\rm ac}) = \frac{\partial}{\partial r}\left[3\sqrt{r}\frac{\partial}{\partial r}\left(\nu\Sigma\sqrt{r}\right) - \frac{2\,\Sigma}{\Omega}\frac{\partial \mathcal{T}}{\partial m}\right]. \quad (10)$$

The quantity $\partial\mathcal{T}/\partial m$ is the torque density distribution, i.e., the gravitational torque per unit disk mass ($dm = 2\pi\Sigma r dr$) arising from tidal interactions with the planet. This function is discussed in Section 2.5. If multiple planets orbit in the disk, $\partial\mathcal{T}/\partial m$ is the sum of all partial torque density distributions. The presence of the tidal torque term in Equation (10) naturally accounts for (planet-induced) gap formation in the density distribution. Notice that, if $\nu\Sigma$ is constant in radius, a viscously evolving planet-less disk is in a steady state.

The mass removed from the disk, via accretion on the planet, per unit surface and unit time, is written as $\dot\Sigma_{\rm ac} = \delta(r-a)\dot M_e/(2\pi a)$ so that $\int 2\pi \dot\Sigma_{\rm ac} r dr = \dot M_e$, the planet's gas accretion rate, which ensures conservation of the mass transferred between the planet and the disk. Contrary to $\dot\Sigma_{\rm pe}$ (which is zero or positive), $\dot\Sigma_{\rm ac}$ can be positive, null, or negative. In the latter case, mass is transferred from the planet to the disk. The planet's envelope can lose mass ($\dot M_e < 0$) if its radius exceeds the accretion radius $R_{\rm A}$ (see Section 2.1). Numerically, to avoid discontinuities, the mass added to (removed from) the planet is removed from (added to) a disk region around the planet's orbit of radial width a few times $R_{\rm H}$.

The presence of an accreting planet can change the mass transfer through the disk and thus alter the disk's surface density (Lubow & D'Angelo 2006). This effect cannot be described by Equation (10). To account for it, the approach of Lubow & D'Angelo (2006) is applied. The accretion rate through the disk is

$dm/dt = 2/(r\Omega)\partial\left(\mathcal{T}_\nu - \mathcal{T}\right)/\partial r$ (adopting the convention that $dm/dt > 0$ for an inward transfer of mass). By indicating with $\langle dm/dt\rangle_{\rm ext}$ and $\langle dm/dt\rangle_{\rm int}$ accretion rates averaged over narrow rings, respectively, exterior and interior to the planet's orbit (and sufficiently apart from it), the condition is imposed that

$$\left\langle \frac{dm}{dt} \right\rangle_{\rm ext} = \left\langle \frac{dm}{dt} \right\rangle_{\rm int} + \dot{M}_e. \tag{11}$$

Equation (11) is used to adjust dm/dt (i.e., Σ) inside and outside of the planet's orbit in a mass-conservative manner. This correction is applied only if $\langle dm/dt\rangle_{\rm ext} - \dot{M}_e > \langle dm/dt\rangle_{\rm int} > 0$. For stability reasons, mass adjustments are spread over several grid zones.

The thermal structure of the disk is determined by imposing a simple energy balance involving viscous heating, radiative cooling from the surface of the disk, and irradiation heating by the star

$$Q_\nu - Q_{\rm cool} + Q_{\rm irr} = 0. \tag{12}$$

In the case of Keplerian rotation, the energy flux produced by viscous dissipation is (Mihalas & Weibel Mihalas 1999)

$$Q_\nu = \frac{9}{4}\nu\Sigma\Omega^2. \tag{13}$$

The energy flux escaping from the disk's surface and the heating flux generated by stellar photons are (Hubeny 1990)

$$Q_{\rm cool} = 2\sigma_{\rm SB}\, T^4 \left(\frac{3}{16}\kappa_{\rm R}\Sigma + \frac{1}{2} + \frac{1}{2\kappa_{\rm P}\Sigma}\right)^{-1} \tag{14}$$

and

$$Q_{\rm irr} = 2\sigma_{\rm SB}\, T_{\rm irr}^4 \left(\frac{3}{16}\kappa_{\rm R}\Sigma + \frac{1}{2} + \frac{1}{2\kappa_{\rm P}\Sigma}\right)^{-1}, \tag{15}$$

respectively. In the equations above, T is the mid-plane temperature of the disk, $T_{\rm irr}$ is the stellar irradiation temperature, and $\kappa_{\rm R}$ and $\kappa_{\rm P}$ are the Rosseland and Planck mean opacities. These opacity coefficients are calculated following the method of D'Angelo & Bodenheimer (2013), for grain size distributions of up to 1 mm in radius, and connected to the gas opacities of Ferguson et al. (2005). The advantage of using the fluxes in Equations (14) and (15) is that, in the approximation of vertically integrated quantities, they also describe optically thin disks. The irradiation temperature is written as (e.g., Menou & Goodman 2004)

$$T_{\rm irr}^4 = \frac{1}{2}\left(T_\star^4 + T_{\rm acc}^4\right)\left(\frac{R_\star}{r}\right)^2\left[\frac{2}{5}\left(\frac{R_\star}{r}\right) + \frac{2}{7}\frac{H}{r}\right]. \tag{16}$$

The disk scale height, assuming vertical hydrostatic equilibrium, is given by $H = \sqrt{\gamma\, k_{\rm B}T/(\mu m_{\rm H})}/\Omega$. The adiabatic index γ is set between 1.4 and 1.6 and the mean molecular weight is $\mu = 2.39$ ($k_{\rm B}$ is the Boltzmann constant and $m_{\rm H}$ the hydrogen mass). Equation (16) includes the contribution from luminosity released by accretion on the star (Pringle 1981)

$$T_{\rm acc}^4 = \frac{1}{8\pi}\left(\frac{GM_\star\dot{M}_\star}{\sigma_{\rm SB}R_\star^3}\right). \tag{17}$$

The stellar accretion rate is computed as $\dot{M}_\star = 2/(r\Omega)\partial\mathcal{T}_\nu/\partial r$, from the solution of Equation (10) at the inner boundary of the disk (where $\mathcal{T} = 0$).

The disk also contains a solid component, assumed to be formed of 100 km-radius planetesimals, whose surface density is σ_Z. In principle, this planetesimal disk would evolve through gravitational encounters, including collisions, and interactions with any embedded planet. Gas drag would also affect the evolution of this solid component, but over rather long timescales, given the size of the bodies considered here. However, for the sake of simplicity and tractability, it is assumed that σ_Z only varies because of depletion by accretion of solids on the planet ($\dot{M}_c$) and because of scattering by the planet's gravity (Ida & Lin 2004)

$$\dot{M}_{\rm scat} = \left(\frac{GM_c}{R_c}\right)^2\left(\frac{a}{2GM_\star}\right)^2\dot{M}_c. \tag{18}$$

The equation above is a very simple approximation, based on energy arguments, and assumes that $M_p \approx M_c$, which is appropriate for the planets modeled here. The surface density σ_Z also changes in response to temperature variations in the disk, allowing for the vaporization of ice (see Section 2.2).

Equation (10) is solved by means of a hybrid implicit/explicit numerical scheme, based on the fourth/fifth-order Dormand-Prince method (embedding backward differentiation) with an adaptive step-size control for the global accuracy of the solution (Hairer et al. 1993). Additional details and tests can be found in D'Angelo & Marzari (2012). Toward the end of the disk's life, when the evolution is entirely driven by photo-evaporation and the disk is quickly dispersed, the algorithm transitions from implicit to explicit, with a time step condition that constrains the maximum amount of mass removed from any disk annulus. Details on the solution method of Equation (12) for the energy balance are also given in D'Angelo & Marzari (2012). The disk extends in radius from the larger of 0.01 au and $R_\star = R_\star(t)$ to 900 au, and is discretized over 6000 grid points by imposing a constant ratio $\Delta r/r$. Beyond 900 au, to ensure that the grid boundary does not interfere with viscous spreading, a buffer zone of 400 additional grid points (at a degraded resolution) brings the outer disk edge to $\approx 3.5\times10^5$ au.

2.5. *Tidal Interactions and Orbital Migration*

In order to describe tidal interactions between the disk and the planet, we apply the formalism of D'Angelo & Lubow (2008, 2010) for local isothermal disks. This is based on the torque density distribution, which is defined by the integral

$$\mathcal{T}(a) \equiv 2\pi\int_0^\infty \frac{\partial\mathcal{T}}{\partial m}\,\Sigma(r)\, r\, dr, \tag{19}$$

where $\mathcal{T}(a)$ is the total torque applied to the planet. In actuality, the integral is performed over the disk's radial extent. In a disk whose properties vary smoothly with radius, the theory of disk resonances (e.g., Meyer-Vernet & Sicardy 1987; Ward 1997) suggests that

$$\frac{\partial\mathcal{T}}{\partial m} = \mathcal{F}(x,\beta,\zeta)\,\Omega^2(a)\,a^2\left(\frac{M_p}{M_\star}\right)^2\left(\frac{a}{\Delta_p}\right)^4, \tag{20}$$

where $\mathcal{F}$ is a dimensionless parametric function of $x = (r-a)/\Delta_p$ with $\Delta_p = \max\left[H(a), R_{\rm H}\right]$, whose extrema are at $x \approx \mp 1$. The parameters $\beta = -d\ln\Sigma/d\ln r$

and $\zeta = -d\ln T/d\ln r$ are calculated as averages between $x = -4$ and 4 (the function $\mathcal{F}$ is practically zero outside of these limits). D'Angelo & Lubow (2010, hereafter DL10) tested the validity of Equation (20) and provided analytic approximations of the function $\mathcal{F}$, for wide ranges of the parameters β and ζ, based on 3D hydrodynamics calculations of disk-planet interactions.

Gravitational interactions transition from a linear to a nonlinear regime when $|\mathcal{T}(a)| \gtrsim |\mathcal{T}_\nu(a)|$, or

$$\left(\frac{M_p}{M_\star}\right)^2 \gtrsim 3\pi \left(\frac{\nu}{a^2\Omega}\right)\left(\frac{\Delta_p}{a}\right)^3. \quad (21)$$

Nonlinear interactions can cause order-of-magnitude variations in the surface density (relative to the unperturbed disk), as the planet mass grows. However, under typical disk conditions, the torque density $\partial\mathcal{T}/\partial m$ varies smoothly across the transition, and the maximum and minimum of the function $\mathcal{F}$ change only by factors of the order of unity. The variation of $\partial\mathcal{T}/\partial m$ across the transition is implemented as explained in DL10.

The rate of change of the planet's orbital radius is found by imposing conservation of orbital angular momentum, which yields $da/dt = 2\mathcal{T}(a)/[M_p\, a\, \Omega(a)]$. Since $\mathcal{T}(a)$ is defined through Equation (19), the migration speed becomes

$$\frac{da}{dt} = 4\pi\,\Omega(a)\left(\frac{a}{M_\star}\right)\left(\frac{M_p}{M_\star}\right)\left(\frac{a}{\Delta_p}\right)^4 \times \int \mathcal{F}(x,\beta,\zeta)\,\Sigma(r)\,r\,dr, \quad (22)$$

where the integration is performed over the entire disk. In the linear regime, one can show that the integral on the right-hand side of Equation (22) is $\propto H^2\Sigma(a)$, hence $da/dt \propto (M_p/M_\star)(\pi a^2\Sigma(a)/M_\star)(a/H)^2$, which is proportional to both the planet mass and the local disk mass ($\pi a^2\Sigma$). A comparison between a direct 3D calculation of planet migration and Equation (22) is shown in Figure 9 of DL10. In the nonlinear regime, the integral depends on the planet mass through functions $\mathcal{F}$ and Σ. As the density gap deepens, the integral has nonzero contributions mostly from regions near the gap edges. D'Angelo et al. (2006) showed that this formalism provides a good agreement with results from hydrodynamics calculations of planet migration also in the nonlinear regime (for non-highly eccentric orbits). It should be noted that there are regimes of fast orbital migration in which $\partial\mathcal{T}/\partial m$ can also depend on da/dt and which may not be fully captured by the formalism applied here (D'Angelo & Lubow 2008). However, the conditions required by these extreme regimes are not met in this study.

The formalism used here for disk-planet tidal interactions relies on the local isothermal approximation of disk's gas. The resulting torques agree well with analytical estimates (Tanaka et al. 2002), when the comparison is possible (DL10; Masset & Casoli 2010). Adiabatic disks can produce torques that may behave differently (see Kley & Nelson 2012; Baruteau et al. 2014, pp. 667-689, for recent reviews). However, while prescriptions are available for the total torque $\mathcal{T}(a)$ acting on a low-mass planet in the adiabatic limit (Masset & Casoli 2010; Paardekooper et al. 2011), there is no formalism for the description of the torque density $\partial\mathcal{T}/\partial m$ in this limit. It is important to stress that the use of the distribution function $\partial\mathcal{T}/\partial m$, but not of $\mathcal{T}(a)$, fulfills the action-reaction principle within the disk-planet system, thus accounting for disk-planet tidal interactions. Additionally, a description based on $\partial\mathcal{T}/\partial m$, but not on $\mathcal{T}(a)$, allows for a *continuous* transition between different regimes of orbital migration, without the need of relying on some gap formation criterion and imposing different migration rates. In fact, as planet mass and disk thermodynamical conditions change, the tidal interactions (and hence da/dt) adapt consistently to the changing conditions. Finally, inside ≈ 5 au, outward migration in adiabatic disks may occur for planet masses somewhat greater than $\approx 7\,M_\oplus$ (Baruteau et al. 2014, pp. 667-689), possibly affecting the largest simulated planet. However, by the time this planet attains that mass, the local disk has become radiatively efficient.

Disk-planet tidal interactions also affect orbital eccentricity. In the linear regime, orbits tend to be circularized on timescales shorter than the migration timescales (e.g., Artymowicz 1993; Tanaka & Ward 2004). In the strong nonlinear regime, the outcome of tidal interactions is more complex (e.g., Lubow & Ida 2011, pp. 347-371), though this regime is not relevant in these calculations.

Orbital migration of a planet during formation may also be driven by interactions with planetesimals (e.g., Minton & Levison 2014, and references therein). However, since the secular evolution of the planetesimals' disk is neglected, so is planetesimal-induced migration.

2.6. *Disk Photo-evaporation*

The disk photo-evaporation follows an approach along the lines of Alexander & Armitage (2007), in which the total amount of gas removed from the disk per unit surface and unit time is

$$\dot\Sigma_{\rm pe} = \dot\Sigma_{\rm dif} + \dot\Sigma_{\rm rim}. \quad (23)$$

By assumption, photo-evaporation is essentially driven by stellar EUV radiation. Gas removal by FUV and X-ray radiation is not considered (but see the discussion in Gorti & Hollenbach 2009; Gorti et al. 2009). The emission rate of EUV ionizing photons by the star is $10^{42}\,{\rm s}^{-1}$ (Alexander & Armitage 2007). The component $\dot\Sigma_{\rm dif}$ represents the removal rate due to the "diffuse" stellar radiation, whereas the additional component $\dot\Sigma_{\rm rim}$ is activated after the disk becomes radially optically thin to stellar photons inside some radius $r_{\rm rim}$ ("rim" photo-evaporation).

Diffuse photo-evaporation depends on the gravitational radius $r_g = GM_\star/c_s^2$ (Hollenbach et al. 1994), where c_s is the sound speed of an ionized hydrogen/helium mixture at $T \approx 10^4$ K, the nearly constant temperature of the upper layers of a disk heated by EUV radiation (e.g., Gorti & Hollenbach 2009). It is assumed that $\dot\Sigma_{\rm pe} \approx 0$ inside of the critical radius $r_{\rm crt} = r_g/10$ (≈ 0.7 au, Liffman 2003; Gorti et al. 2009), where gas lies too deeply in the gravitational field of the star to escape. The maximum of $\dot\Sigma_{\rm dif}$ is around the radius $r \approx r_{\rm crt}$.

For most of the disk evolution, $\dot\Sigma_{\rm rim} = 0$. At later times, when the mass supply rate operated by viscous stresses cannot keep up with the removal rate caused by $\dot\Sigma_{\rm dif}$, the disk's gas becomes locally depleted (typically, somewhat inward of 1 au). Inside of this density gap induced by photo-evaporation, gas viscously drains toward the star on relatively short timescales, of the order of 10^4 years for the kinematic viscosity adopted in this study. Once the disk develops an inner cavity, becoming optically thin interior to $r = r_{\rm rim}$, $\dot\Sigma_{\rm rim}$ provides an additional contribution to photo-evaporation at and around the rim region. As a

result of the enhanced $\dot{\Sigma}_{\rm pe}$, the rim radius $r_{\rm rim}$ increases as the disk disperses from the inside out. The presence of a sufficiently massive planet, with a semi-major axis of $a \approx r_{\rm crt}$, can aid in the formation of the photo-evaporation induced gap through gas depletion by tidal torques. Beyond the critical radius, a planet accreting gas at high rates can reduce the gas density interior to its orbit (see Equation (11)) and hence facilitate gap formation by photo-evaporation.

3. IN SITU FORMATION MODELS

The calculations consider two phases: the formation phase during which accretion of gas and solids takes place, and the evolutionary or isolation phase, during which the core mass remains constant but the envelope is subject to evaporative mass loss. During this latter phase, the planet is assumed to be completely isolated. These phases, up to an age of 8 Gyr, are followed numerically for all six of the Kepler 11 planets. Each planet is assumed to form at its present orbital position; migration is not considered, either of the planet or of the solid material that forms its core. The initial core mass is $\approx 1\,M_\oplus$ at a time of 2×10^5 yr; the corresponding envelope mass is $\approx 10^{-3}\,M_\oplus$, consistently calculated with the core mass and the nebular boundary conditions. The surface density of solids σ_Z at each formation radius is adjusted so that the final model at an age of 8 Gyr matches, as closely as possible, the radius of the planet as measured by Kepler. The corresponding total planetary masses are then compared to those measured via transit timing variations (L13). As pointed out by Bodenheimer & Lissauer (2014), these required surface densities are high (see Table 2), a factor of roughly four to eight times those given by the minimum-mass extrasolar nebula of Chiang & Laughlin (2013) and three to nine times the values estimated by Schlichting (2014). Compared to the densities extrapolated from the minimum-mass solar nebula of Hayashi (1981), these factors would be much larger, between 25 and 60.

The disk temperature during the formation phase, which serves as a boundary condition on the planetary structure, is assumed to be $T = 1000$ K in all cases – the same assumption is made by Chiang & Laughlin (2013). The disk gas density during that phase is derived assuming that the gas-to-solid mass ratio is 200, and that the ratio of the disk scale height to the orbital distance is $H/a = 0.03$. The disk gas density is assumed to decrease linearly with time, with an assumed cutoff time for the presence of the gas of 3.5 Myr, which in these models represents the isolation time, $t_{\rm iso}$. The outer radius of the planet, R_p, during the formation phase is given by the accretion radius $R_{\rm A}$ in Equation (1). As mentioned in Section 2.1, the factor four approximately describes the results of hydrodynamics simulations of a planet embedded in a disk (Lissauer et al. 2009), which show that only the gas within $\approx R_{\rm H}/4$ remains bound to the planet. In these in situ models, the value of $R_{\rm H}/4$ is always smaller than the Bondi radius, $R_{\rm B}$, by a factor of ≈ 2 to ≈ 5. Thus, Equation (1) implies that R_p is only weakly dependent on disk temperature. Furthermore, as the disk cools with time $R_{\rm B}$ gets larger. Stevenson (1982) showed that the planet structure is only marginally dependent on R_p for radiative envelopes (which is the case for the outer part of the envelope). Hence, the assumption that the disk temperature is constant with disk radius is not expected to significantly affect the results.

At the cutoff time, the model makes a transition from disk boundary conditions (i.e., the nebular stage, see Section 2.1) to isolated conditions, basically stellar photospheric boundary conditions with the inclusion of the radiation input from the central star, as given by Equations (2)–(5). The surface temperature of the planet during the evolutionary phase is normally close to the equilibrium temperature, $T_{\rm eq}$ in the stellar radiation field; the approximation is made that this temperature is constant with time. The outer layers rapidly thermally adjust to this new temperature, which is between 500 and 1000 K. In all cases, the mass of the gaseous envelope is considerably less than that of the heavy-element core at the time of this transition. The phase of rapid gas accretion (see Section 2.1) is never reached. When accretion stops, the radius of the planet decreases considerably on a short timescale, then declines slowly as the planet contracts and cools.

During the isolation phase, mass loss from the planet's atmosphere as a result of energy input from stellar X-ray and EUV photons can be important. This process is included, starting immediately after disk dispersal ($t = 3.5$ Myr), according to the energy-limited approximation outlined in Section 2.3. These calculations apply a standard value for the efficiency parameter, $\varepsilon = 0.1$. The mass loss turns out to be quite important for the inner planet Kepler 11b, but not significant for the outer planet Kepler 11g.

The present calculations differ from those published in earlier papers (e.g., Hubickyj et al. 2005; Lissauer et al. 2009) because of the dust and molecular opacities applied during the formation phase. The opacity table includes grain sizes in the range from 0.005 μm to 1 mm, with a power-law size distribution proportional to the grain radius to the power of -3 (see Figure 1, top). This grain size distribution matches the observations of T Tauri disks better than do opacities based on an interstellar size distribution, reduced by a constant factor of about 50, as used in our earlier papers. In contrast to the calculations of Bodenheimer & Lissauer (2014), where grain settling and coagulation were included according to the method of Movshovitz et al. (2010), the present calculations use pre-computed tables of opacity as a function of temperature and density. These simulations require numerous trials based on adjustment of the main parameter, which is the solid surface density, and inclusion of the detailed opacity simulations would have been too time-consuming. During the isolation phase, since there is no input of solid material, the grains are assumed to have settled into the envelope's interior and evaporated; the molecular opacities of Freedman et al. (2008) are used during this phase.

3.1. *In Situ Model Results*

Table 2 gives a summary of the final properties of the six simulated Kepler 11 planets, along with the deduced value of σ_Z. The final core mass, the final envelope mass, the final core radius, the final planet radius, the final planet luminosity, the composition, and the orbital position are presented.

Figures 3 and 4 show, for the various planets, the evolution of the core mass, envelope mass, and outer radius. In general, because of the high solid surface densities required, the core mass increases rapidly, on a timescale $< 10^5$ years. In fact, by using Equation (6), the accretion timescale of the core is

$$\frac{M_c}{\dot{M}_c} = \frac{4}{3}\frac{\rho_c R_c}{\sigma_Z F_g}\sqrt{\frac{a^3}{GM_\star}}, \tag{24}$$

Table 2
Summary of Results for In Situ Formation of Kepler 11 Planets[a]

Planet	$M_c/M_\oplus$	$M_e/M_\oplus$	$R_c/R_\oplus$	$R_p/R_\oplus$	$L_p/L_\odot$	(Fe,Si)%[b]	(Fe,Si,H+He)%[c]	a [au]	σ_Z [g cm^{-2}]
b	1.96	0.00	1.19	1.19		(30, 70)	(30, 70, 0.0)	0.091	10000
c	5.76	0.26	1.60	2.91	3.9×10^{-7}	(30, 70)	(28.7, 67.0, 4.3)	0.107	14500
d	5.01	0.49	1.53	3.24	2.3×10^{-7}	(30, 70)	(27.7, 64.5, 7.8)	0.155	6200
e	6.66	1.45	1.67	4.24	2.1×10^{-7}	(30, 70)	(24.6, 57.5, 17.9)	0.195	4600
f	2.84	0.11	1.33	2.42	4.1×10^{-8}	(30, 70)	(28.9, 67.4, 3.7)	0.250	1680
g	5.01	0.74	1.53	3.34	2.4×10^{-8}	(30, 70)	(26.1, 61.0, 12.9)	0.466	685

[a] Values at time $t = 8$ Gyr. The last column refers to the local density of solids at $t = 0$.
[b] Percentage of the core mass. 'Fe' and 'Si' indicate the core's iron nucleus and the silicate mantle, respectively.
[c] Percentage of the planet mass. 'H+He' represents the envelope gas.

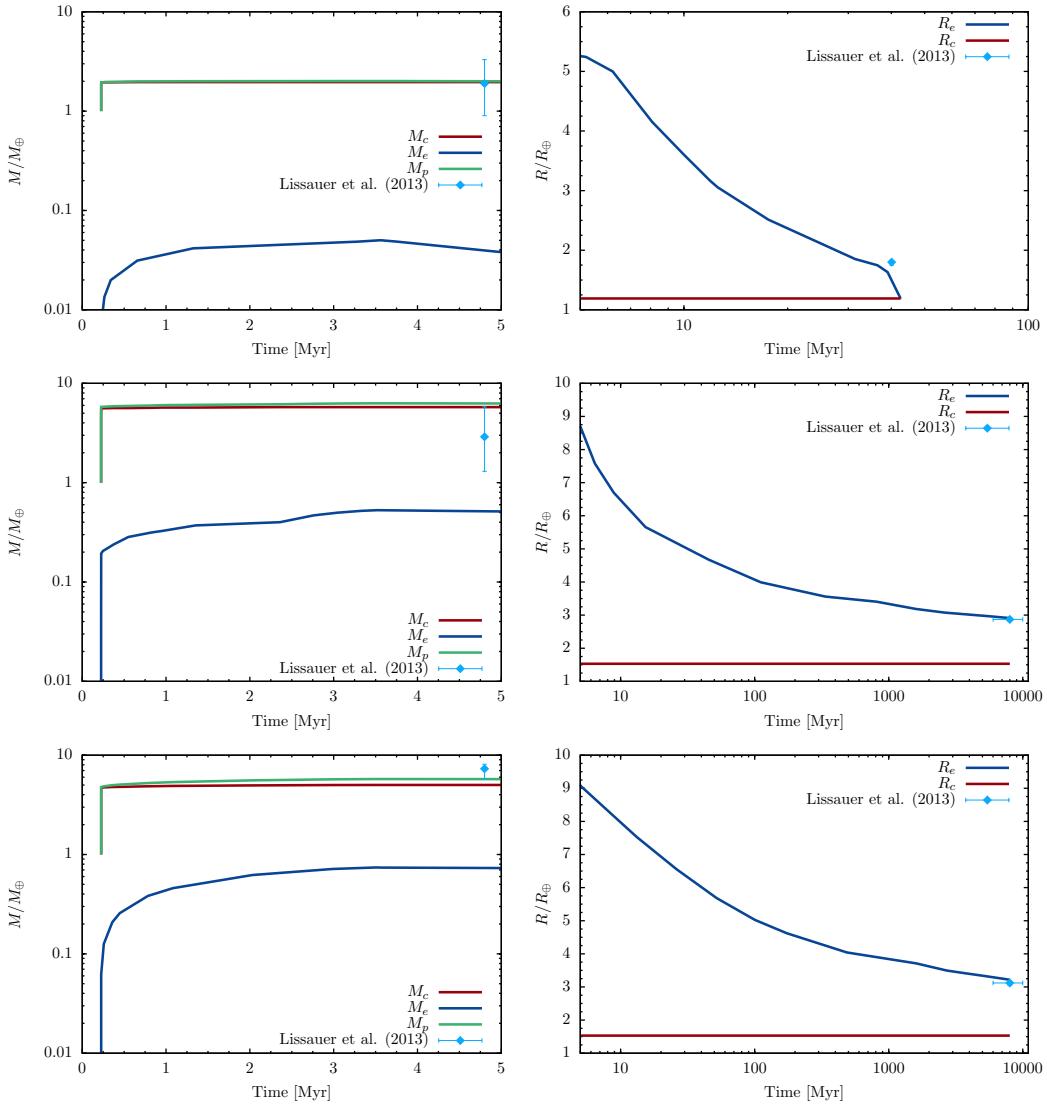

Figure 3. Formation and evolutionary (i.e., isolation) phases of in situ models for planets Kepler 11b (top), Kepler 11c, and Kepler 11d (bottom). Core, envelope, and total mass (left panels, as indicated), and core and envelope radius (right panels as indicated; $R_e = R_p$) are illustrated as functions of time. The disk's gas around the planet's orbit is assumed to disperse in $t_{\rm iso} = 3.5$ Myr. The models start from a $1\,M_\oplus$ planetary core at a time of 2×10^5 yr. The vertical error bars indicate the results from L13. To account for uncertainty, the age of the star is assumed to be 8 ± 2 Gyr (Lissauer et al. 2011a, Nasa Exoplanet Archive, and The Extrasolar Planets Encyclopaedia).

Table 3
Properties of In Situ Formation Models of Kepler 11 Planets at Isolation[a]

Planet	$t_{\rm iso}$[Myr]	$M_c/M_\oplus$	$M_e/M_\oplus$	$R_c/R_\oplus$	$R_p/R_\oplus$	(Fe,Si,H+He)%[b]	$T_{\rm eq}$[c] [K]	$\langle\dot{M}_e\rangle$[d] [$M_\oplus\,{\rm yr}^{-1}$]
b	3.5	1.96	0.05	1.19	5.3	(29.2, 68.3, 2.5)	927	-4.0×10^{-9}
c	3.5	5.76	0.53	1.60	9.5	(27.5, 64.1, 8.4)	880	-1.3×10^{-9}
d	3.5	5.01	0.74	1.53	11.7	(26.1, 61.0, 12.9)	731	-1.2×10^{-9}
e	3.5	6.66	1.65	1.67	14.3	(24.0, 56.1, 19.9)	623	-1.0×10^{-9}
f	3.5	2.84	0.16	1.33	8.4	(28.4, 66.3, 5.3)	550	-2.6×10^{-10}
g	3.5	5.01	0.75	1.53	9.4	(25.7, 59.9, 14.4)	409	-1.0×10^{-10}

[a] The isolation time, $t_{\rm iso}$, is the time at which disk's gas is assumed to disperse.
[b] Percentage of the planet mass at time $t = t_{\rm iso}$.
[c] Constant equilibrium temperature, $T_{\rm eq}$, during the isolation phase.
[d] Rate of change of the envelope mass averaged over the first 100 Myr of evolution in isolation. For Kepler 11b, $\langle\dot{M}_e\rangle$ is an average over 10 Myr.

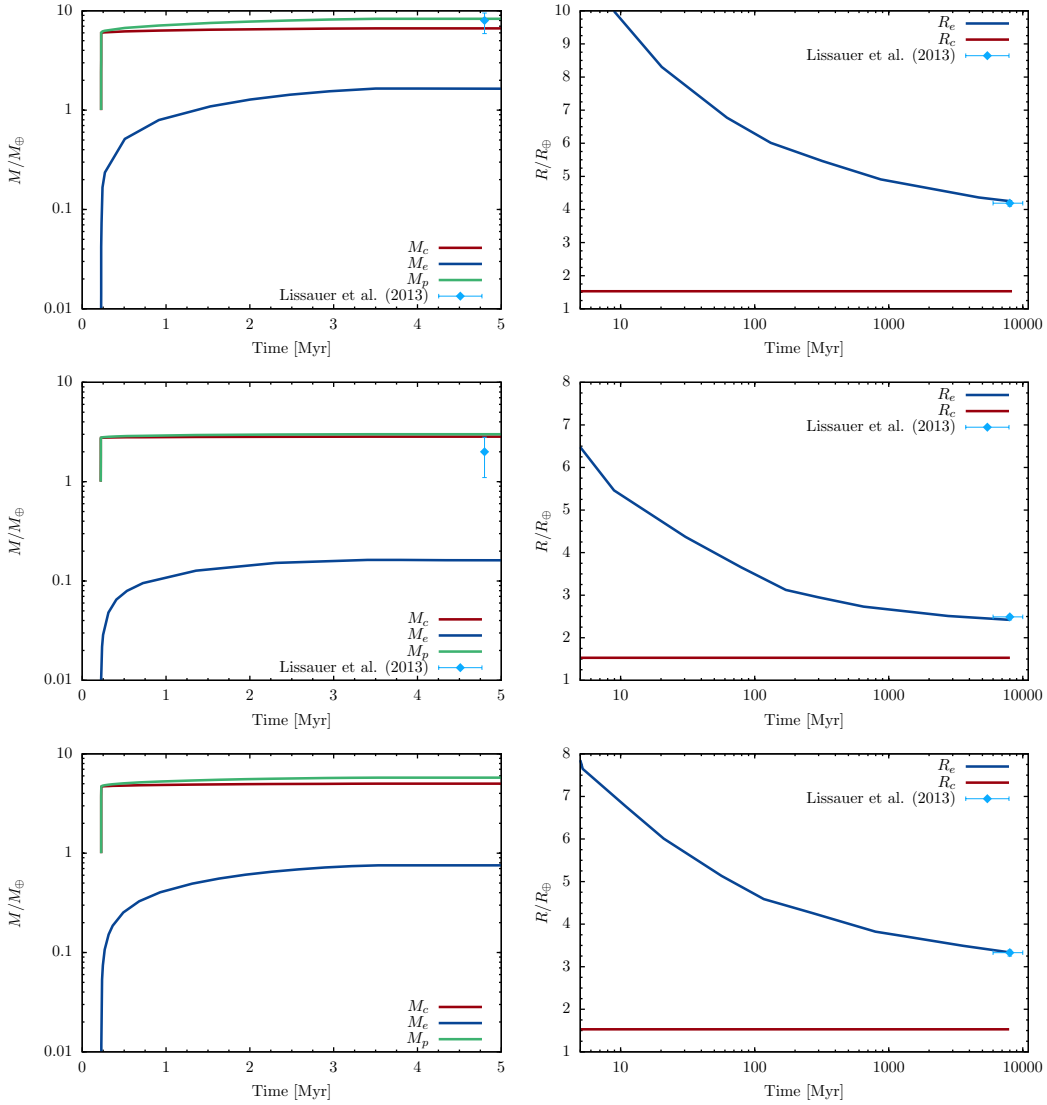

Figure 4. Same as in Figure 3, but for in situ models of Kepler 11e (top), Kepler 11f, and Kepler 11g (bottom).

where the cross section for planetesimals' capture is $\mathcal{S}_{\rm eff} \approx \pi R_c^2$ when the gas bound to the core is very tenuous. If $F_g \approx 1$, Equation (24) gives initial accretion timescales (see a and σ_Z in Table 2) $\lesssim 10^5$ yr. Nonetheless, at an initial envelope mass of $\approx 10^{-3}\,M_\oplus$, even 100 km-size planetesimals are affected by gas drag in the envelope and $\mathcal{S}_{\rm eff}$ becomes $\gg \pi R_c^2$ (D'Angelo et al. 2014). In the calculations, the actual timescales are all of the order of 10^4 yr (see Figures 3 and 4). Thus, any uncertainties in Equation (6) or in the choice of the initial core mass have practically no effect on the final result. The core mass levels off at the isolation mass, as given by Equation (7). The envelope mass increases more slowly, on a timescale of 10^6 yr. The outer radius during the formation phases shows an initial rapid rise corresponding to the rapid core growth, and then a nearly flat section since the outer boundary condition is essentially determined by the nearly constant core mass. Once the transition at $t_{\rm iso} = 3.5$ Myr is reached, the radius decreases rapidly as a result of the transition to isolated boundary conditions. Beyond that time, the radius decreases slowly as a result of contraction and cooling. As a further effect, the envelope mass and outer radius decline as a result of mass loss induced by stellar XUV radiation.

Some properties of the Kepler 11 planets at the time of disk dispersal ($t = t_{\rm iso}$), according to our in situ models, are reported in Table 3. Planet Kepler 11b would lose its entire H+He envelope in 4×10^7 years. For planets Kepler 11f through c, proceeding inwards, mass-loss rates are 1 to $5 \times 10^{-9}\,M_\oplus\,{\rm yr}^{-1}$ at 10 Myr, decreasing to 1 to $5 \times 10^{-10}\,M_\oplus\,{\rm yr}^{-1}$ at 100 Myr. At the final age of 8 Gyr, these rates are down to 2.3×10^{-13} to $1.3 \times 10^{-12}\,M_\oplus\,{\rm yr}^{-1}$.

Specifically, the main results from our in situ models can be summarized as follows.

Kepler 11b. a low-mass H+He envelope forms around the core mass of $1.96\,M_\oplus$, but during the isolation phase this envelope is entirely lost. The final mass is consistent with the measured mass $1.9^{+1.4}_{-1.0}\,M_\oplus$ (L13), but the final radius, the core radius of $1.19\,R_\oplus$, is far below the measured value of $1.80^{+0.03}_{-0.05}\,R_\oplus$, as shown in the top-right panel of Figure 3. Even by taking the upper limit of the measured mass, a 100% silicate core would still have too small a radius, only $1.5\,R_\oplus$. A steam envelope (not modeled here) is probably required to achieve consistency (Lopez et al. 2012). This possibility, however, is inconsistent with in situ formation inside 0.1 au of a solar-type star because of the lack of ice in the core. Another possibility is the release of gas sequestered by the core during formation. The result that the entire envelope mass is lost remains valid even if the assumed core mass is increased to $3\,M_\oplus$.

Kepler 11c. about half of the accreted envelope mass is lost during the isolation phase, but the final radius agrees with the measured radius of $2.87^{+0.05}_{-0.06}\,R_\oplus$ (see Figure 3, center-right). The final total mass of $6.02\,M_\oplus$ falls just above the one-standard-deviation upper limit for the measured mass of $2.9^{+2.9}_{-1.6}\,M_\oplus$, but is certainly within the uncertainties in the theoretical models.

Kepler 11d. about one-third of the accreted envelope mass is lost during the isolation phase. The final computed radius of $3.24\,R_\oplus$ is within 4% of the measured value of $3.12^{+0.06}_{-0.07}\,R_\oplus$ (see Figure 3, bottom-right). The final computed total mass of $5.5\,M_\oplus$ is just below the one-standard-deviation lower limit for the measured mass of $7.3^{+0.8}_{-1.5}\,M_\oplus$. These small discrepancies are well within the uncertainties of the models. To reduce the radius to agree with the measured value would require reducing the mass, increasing the discrepancy with the measured value.

Kepler 11e. at a separation from the star of about 0.2 au, the accreted H+He envelope of this object loses only about 12% of its mass during the isolation phase. The final computed radius of $4.24\,R_\oplus$ agrees to within 1.5% with the measured value of $4.19^{+0.07}_{-0.09}\,R_\oplus$, as indicated the in top-right panel of Figure 4. The final computed total mass of $8.11\,M_\oplus$ agrees with the measured mass of $8.0^{+1.5}_{-2.1}\,M_\oplus$. A slight reduction in the assumed mass ($\approx 5\%$) would bring the radius into agreement with the observed value and the planet mass would still agree with the observed mass, well within one-standard-deviation uncertainties.

Kepler 11f. even though the planet lies farther from the star (0.25 au) than Kepler 11e, its lower core mass (2.8 vs $6.7\,M_\oplus$) results in 31% of the H+He envelope being lost during the isolation phase. The final computed radius of $2.42\,R_\oplus$ agrees with the measured value of $2.49^{+0.04}_{-0.07}\,R_\oplus$ to within 2.5% (see Figure 4, center-right). The final total mass of $2.95\,M_\oplus$ is slightly above the one-standard-deviation upper limit for the measured value of $2.0^{+0.8}_{-0.9}\,M_\oplus$. To improve the agreement with the observed radius, the assumed mass would have to increase by about $0.1\,M_\oplus$, increasing the (small) discrepancy with the observed value. In any case, the agreement is within the uncertainties of the theoretical model.

Kepler 11g. at a distance of 0.466 au, the planet loses only about 2% of its H+He envelope mass during the isolation phase. The computed final radius of $3.34\,R_\oplus$ agrees with the measured value of $3.33^{+0.06}_{-0.08}\,R_\oplus$. The corresponding computed total mass is $5.75\,M_\oplus$. The observed mass in this case is not well constrained; it is less than $25\,M_\oplus$.

4. EX SITU FORMATION MODELS

4.1. *General Results*

The two phases of planet evolution identified in Section 3 can also be defined in ex situ models. The time $t = 0$ coincides with the time at which the disk evolution starts from the imposed initial conditions. The gaseous disk evolution depends on several quantities (see Section 2.4–2.6). The gas surface density at $t = 0$ is $\Sigma = 1110\sqrt{1\,{\rm au}/r}\,{\rm g\,cm^{-2}}$ with an exponential cut-off beyond some radius, so that a total disk mass of $0.03\,M_\odot$ is initially confined within ≈ 60 au of the star (see, e.g., Williams & Cieza 2011). This surface density distribution, $\Sigma(t = 0)$, was determined after a number of attempts aimed at reproducing the observed physical properties of planet Kepler 11b and at tentatively matching those of Kepler 11f (the planet farthest from the star for which both R_p and M_p are constrained by transit observations). Only later it was realized that, fortuitously, $\Sigma(t = 0)$ inside ≈ 10 au matches quite closely the minimum-mass solar nebula density of Davis (2005). Although no other slope $d\ln\Sigma/d\ln r$ was tested for the initial Σ, it is unlikely that the adopted initial surface density provides a unique solution to the problem. In any case, the choice of the initial density values is likely to influence the outcomes of the models more than does the choice of the initial slope $d\ln\Sigma/d\ln r$.

These calculations apply a time-constant kinematic viscosity $\nu = \nu_1\sqrt{r/1\,{\rm au}}$, where $\nu_1 \approx 4 \times 10^{14}\,{\rm cm^2\,s^{-1}}$. In terms of the viscosity prescription of Shakura & Sunyaev (1973), the α-parameter quantifying turbulence varies with time and distance from the star. The value around the starting orbital radius of the simulated planets is between

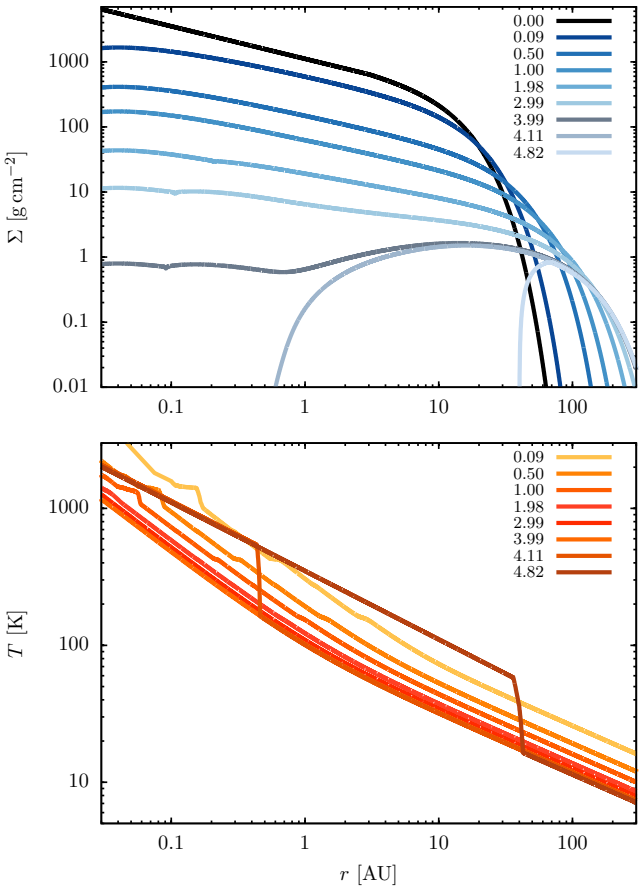

Figure 5. Surface density (top) and temperature distribution (bottom) of the disk's gas, from the model of Kepler 11b, as a function of time (as indicated in the legends in units of megayears). A cavity forms in the inner disk at $t \approx 4.1$ Myr. Photo-evaporation of gas caused by stellar irradiation first induces the formation of a density gap, which turns into a cavity because gas interior to the gap is rapidly removed by viscous diffusion toward the star. The disk rim, i.e., the external edge of the gap, now exposed to direct stellar irradiation, quickly recedes away (see Section 2.6 for details). The temperature transitions in the profiles at 4.1 and 4.8 Myr represent transitions between the local irradiation temperature (in Equation (16)) and the gas temperature (from Equation (12)).

$\approx 10^{-3}$ and $\approx 10^{-2}$. The disk provides an initial accretion rate toward the star of order $10^{-7}\,M_\odot\,\mathrm{yr}^{-1}$.

The lifetime of the gaseous disk is determined by $\Sigma(t = 0)$, ν, the initial disk mass, and the photo-evaporation rate. All of these quantities are the same for all planet models. As mentioned in Section 2.6, the presence of a planet may affect disk dispersal, to a smaller or larger extent depending on the planet mass, its gas accretion rate, and orbital radius. In fact, although the planets end up inside the critical radius $r_{\rm crt}$, they do spend most of their disk-embedded evolution at larger radii and, therefore, they can potentially influence $\dot{\Sigma}_{\rm pe}$. However, in the models presented here, this effect appears to be marginal and the gas inside 1 au is dispersed in ≈ 4 Myr, with a time-spread among models of about 2%.

The evolution of Σ and T is illustrated in Figure 5 (see the figure's caption for details). Dust opacity transitions are visible in the temperature profiles, the most prominent of which are represented by the evaporation of the silicate species above 1000 K. The fainter opacity transitions associated with the evaporation of icy grains are also visible (located around 3 au at $t \approx 10^5$ yr and 1 au at $t \approx 10^6$ yr). In the forming region of Kepler 11 planets ($r > 0.09$ au), the gas temperature is $\lesssim 1600$ K at $t \approx 10^5$ yr and becomes $\lesssim 1000$ K at times $t \gtrsim 5 \times 10^5$ yr. By the time the simulated planets have settled on their final orbits, the local gas temperature varies between ≈ 160 and ≈ 500 K.

Gas photo-evaporation by stellar irradiation produces a density gap somewhat inward of 1 au, around the radius $r_{\rm crt} \approx 0.7$ au, where the ratio between the photo-evaporation timescale and the accretion timescale through the disk is smallest. Viscous diffusion quickly removes gas inward of $r_{\rm crt}$ on a timescale of $\sim r_{\rm crt}^2/\nu$ (see Section 2.6), generating a cavity at $t \approx 4.1$ Myr. Afterwards, rim photo-evaporation dissipates gas inside-out, pushing the cavity edge outward to $r \approx 40$ au by $t \approx 4.8$ Myr (see Figure 5). Inside the disk cavity, which is virtually devoid of gas, the temperature T is set equal to the irradiation temperature, so that $T^4 = L_\star/(4\pi\sigma_{\rm SB} r^2)$. Beyond the cavity edge, the temperature is set by the gas thermal balance, Equation (12) (hence the large temperature transitions in the bottom panel of Figure 5 for $t > 4$ Myr). The evolution of Σ and T in Figure 5 is the same for all models, except for variations induced by disk-planet tidal interactions and gas accretion on the planet.

The energy output of the central star can impact both the evolution of the disk and that of the planet. The two stellar models considered here (see Section 2.1) show similar luminosities for $t \gtrsim 10$ Myr (see Figure 2), implying similar evolution of the planets in isolation. However, there are differences at earlier times, specifically in the effective temperature $T_\star$ and radius $R_\star$, which enter the irradiation temperature in Equation (16). Therefore, the disk thermal budget may be affected and hence the planet migration history may differ somewhat (see Section 2.5). The temperature at the planet surface may also change. These differences are assessed for the cases of Kepler 11b and c (see Section 4.2).

Among the main simplifications of this study are the neglect of planet-planet interactions and the fact that only a single planet evolves in the disk, though the models account for the depletion of the planetesimal disk generated by planets that have already initiated the formation process. It is assumed that by the time $t = t_i$, a solid core of mass $M_c = 0.1\,M_\oplus$ (corresponding to $M_e \approx 10^{-7}\,M_\oplus$, calculated consistently with M_c and the disk boundary conditions) has formed at a current orbital radius of $r = a_i$. There is no speculation about its previous accretion/migration history and a_i is considered to be the initial orbital radius of the simulated planet. (However, the small initial planet mass implies that orbital migration via disk-planet tidal interactions may be negligible at times $t < t_i$). Both t_i and a_i are free parameters, constrained by the requirement, among others, that no two orbital paths intersect each other. Strictly speaking, this is not a physical requirement (e.g., Hands et al. 2014) but rather a necessity dictated by the absence of gravitational interactions among planets. The time t_i ranges from $\approx 6 \times 10^4$ yr (Kepler 11b) to $\approx 10^6$ yr (Kepler 11f). Clearly, the time t_i is also determined by the choice of using the same initial core mass for all planets. The orbital radius a_i ranges from ≈ 2.1 au for Kepler 11f to 5.35 au for Kepler 11e.

Table 4 summarizes the final properties (and a_i) of the six simulated Kepler 11 planets, assumed to have formed ex situ. These are referred to as reference models. The initial orbital radius of each planet, a_i, and the epoch t_i are found by trial and error so that the final model provides

Table 4
Summary of Results for Ex Situ Formation of Kepler 11 Planets[a]

Planet	$M_c/M_\oplus$	$M_e/M_\oplus$	$R_c/R_\oplus$	$R_p/R_\oplus$	$L_p/L_\odot$	(Fe,Si,H_2O)%[b]	(Fe,Si,H_2O,H+He)%[c]	a_i [au]	a_f [au]
b	2.10	0.00	1.47	1.47		(10.6, 50.6, 38.8)	(10.6, 50.6, 38.8, 0.0)	2.14	0.091
c	4.56	0.10	1.84	2.84	2.1×10^{-7}	(6.6, 46.5, 46.9)	(6.5, 45.5, 45.9, 2.1)	3.94	0.109
d	5.58	0.31	1.93	3.14	1.4×10^{-7}	(6.0, 46.0, 48.0)	(5.7, 43.6, 45.5, 5.2)	4.68	0.156
e	6.90	1.29	2.00	4.14	1.6×10^{-7}	(5.7, 45.7, 48.6)	(4.8, 38.5, 41.0, 15.7)	5.35	0.194
f	2.74	0.07	1.62	2.49	3.4×10^{-8}	(6.1, 46.1, 47.8)	(6.0, 44.9, 46.6, 2.5)	2.10	0.248
g	5.57	0.69	1.92	3.40	1.9×10^{-8}	(5.0, 45.0, 50.0)	(4.5, 40.1, 44.4, 11.0)	4.41	0.469

[a] Values at time $t = 8$ Gyr.
[b] Percentage of the core mass. 'Fe', 'Si', and 'H_2O' indicate, respectively, the iron nucleus, the silicate mantle, and the H_2O outer shell of the core (see Appendix A for details).
[c] Percentage of the planet mass.

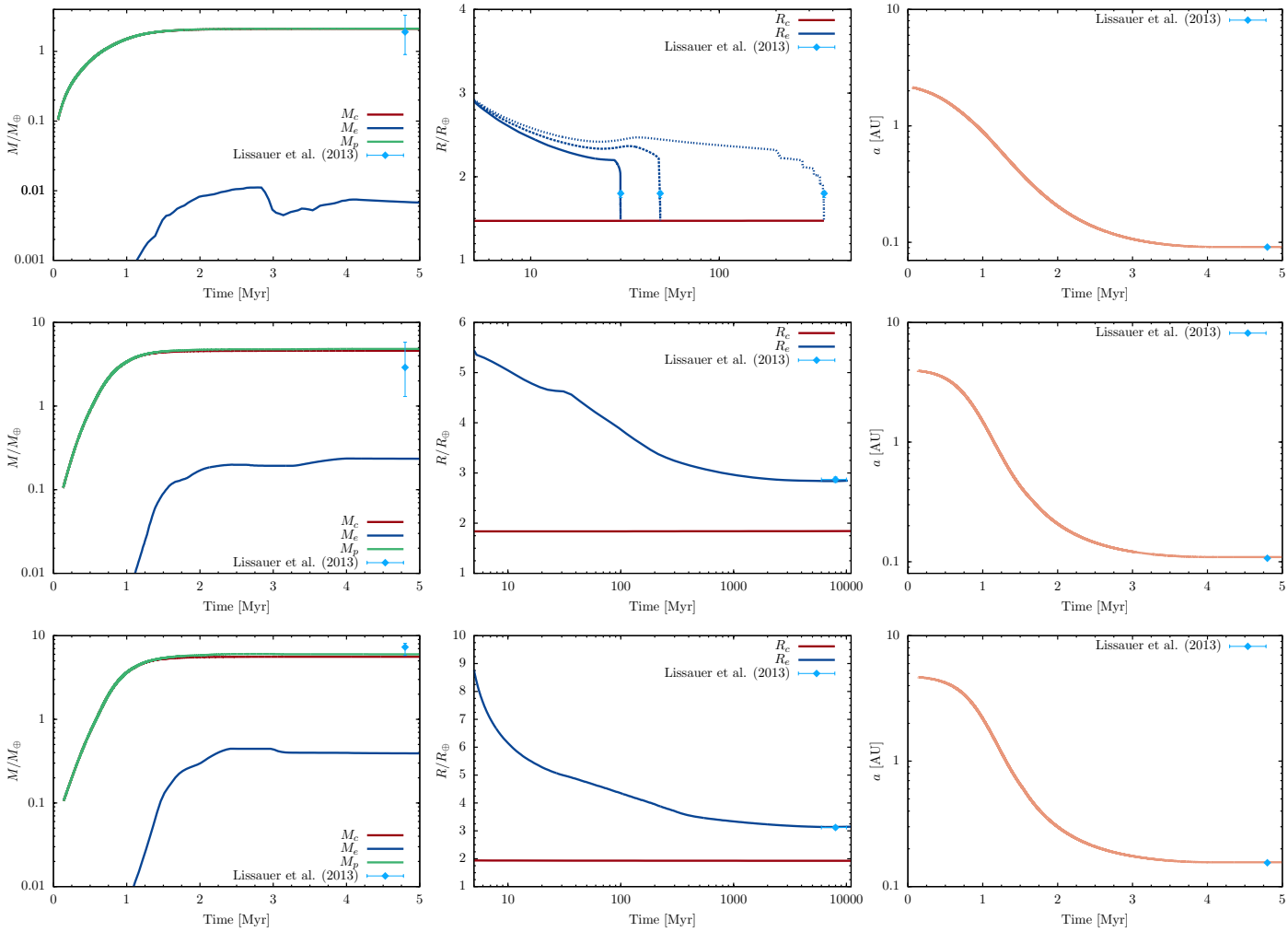

Figure 6. Results from ex situ models of Kepler 11b (top), Kepler 11c, and Kepler 11d (bottom). Plots show, as a function of time, core, envelope, and total mass (left), core and envelope radius (center; $R_e = R_p$), and orbital radius (right). Disk's gas inside ≈ 1 au dissipates within a little over 4 Myr (see Table 5). For Kepler 11b, the plot of the radius evolution includes the reference case with an efficiency for mass loss due to photo-evaporation of $\varepsilon = 0.1$ (solid line), and the cases with $\varepsilon = 0.05$ (dashed line) and 0.01 (dotted line). All models start from a $0.1\,M_\oplus$ planetary embryo, at time t_i. The vertical error bars indicate the results from L13. To account for uncertainty, the age of the star is assumed to be 8 ± 2 Gyr (Lissauer et al. 2011a, Nasa Exoplanet Archive, and The Extrasolar Planets Encyclopaedia).

Table 5
Properties of Ex Situ Formation Models of Kepler 11 Planets at Isolation[a]

Planet	$t_{\rm iso}$[Myr]	$M_c/M_\oplus$	$M_e/M_\oplus$	$R_c/R_\oplus$	$R_p/R_\oplus$	(Fe,Si,H_2O,H+He)%[b]	$T_{\rm eq}$[c] [K]	$\langle\dot{M}_e\rangle$[d] [$M_\oplus\,{\rm yr}^{-1}$]
b	4.11	2.10	0.007	1.47	3.2	(10.6, 50.4, 38.6, 0.4)	819	-3.8×10^{-10}
c	4.08	4.56	0.235	1.84	8.0	(6.2, 44.3, 44.6, 4.9)	749	-5.8×10^{-10}
d	4.06	5.58	0.395	1.94	12.7	(5.6, 42.9, 44.9, 6.6)	627	-4.0×10^{-10}
e	4.04	6.90	1.399	2.02	14.9	(4.8, 38.0, 40.4, 16.8)	563	-4.7×10^{-10}
f	4.09	2.74	0.098	1.62	6.8	(5.9, 44.5, 46.1, 3.5)	492	-1.1×10^{-10}
g	4.04	5.57	0.701	1.94	9.8	(4.5, 40.0, 44.3, 11.2)	361	-1.0×10^{-10}

[a] The isolation time, $t_{\rm iso}$, is the time at which the disk's gas at $r \lesssim a$ disperses.
[b] Percentage of the planet mass at time $t = t_{\rm iso}$.
[c] Equilibrium temperature of the planet, Equation (5), at $t = t_{\rm iso}$.
[d] Rate of change of the planet's envelope mass averaged over the first 100 Myr of evolution in isolation. For Kepler 11b, $\langle\dot{M}_e\rangle$ is an average over 10 Myr.

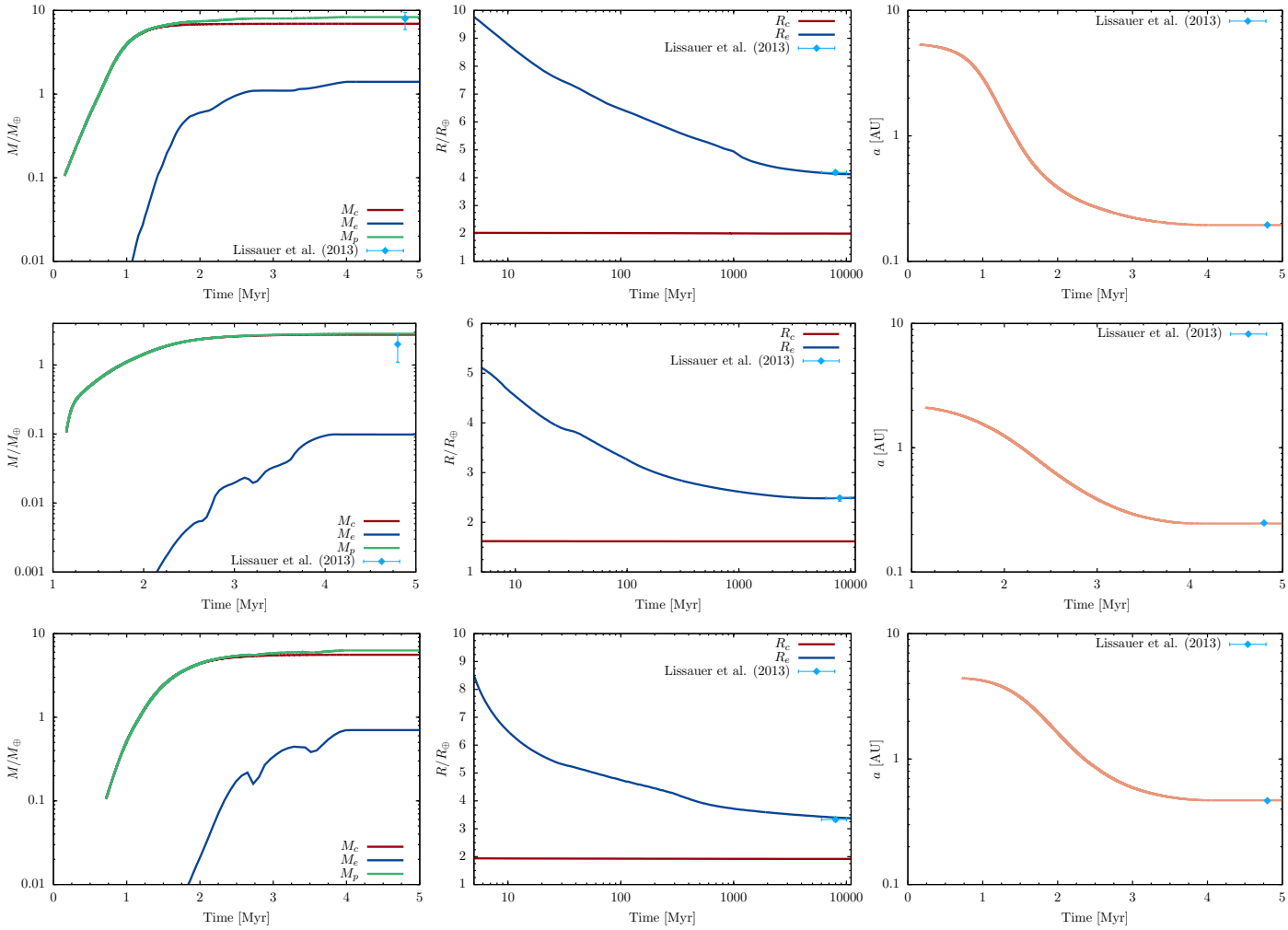

Figure 7. Same as in Figure 6, but for ex situ models of Kepler 11e (top), Kepler 11f, and Kepler 11g (bottom). The simulated evolution of Kepler 11f begins slightly inside Kepler 11b's initial orbit, but at a much later time. Kepler 11g starts in between the initial orbits of Kepler 11c and d, but is delayed until these planets are inside 3.5 au.

reasonable matches to a, R_p, and M_p at an age of 8 Gyr, as reported by L13. Additionally, as mentioned above, orbital paths must not intersect. Plots of various quantities versus time from the resulting models are illustrated in Figures 6 and 7. Since all planets start well beyond 1 au, contrary to in situ models, the local density of solids at a_i and t_i is moderate to low: $\sigma_Z \approx 9\,\mathrm{g\,cm^{-2}}$ for Kepler 11b, $\approx 6\,\mathrm{g\,cm^{-2}}$ for Kepler 11f, and between ≈ 3 and $\approx 4\,\mathrm{g\,cm^{-2}}$ for the other planets (in ascending order of a_i).

Models for each planet were constructed in ascending order of final orbital radius, a_f. At time $t = 0$, the gas-to-solid mass ratio is set to about 70 beyond the ice condensation line at around 3 au ($T < 150$ K). Planetesimals are anhydrous interior to ≈ 1 au ($T > 250$ K), where the gas-to-solid mass ratio becomes approximately 140 (see Section 2.2 for details). As the disk evolves, the ice sublimation line moves inward to $r \approx 1$ au by $t \approx 1$ Myr (see Figure 5). The model for Kepler 11b is constructed from this initial surface density of solids, $\sigma_Z(t = 0)$. The distribution σ_Z is depleted by the passage of Kepler 11b. Indicating with a_i^c the initial and a_f^c the final (i.e., observed) orbital radii of Kepler 11c, the distribution σ_Z for modeling this planet is determined by taking the depleted mass in solids between a_f^c and $\approx 1.25\,a_i^c$, and redistributing the mass over the region according to a $1/\sqrt{r}$ power law. The same procedure is used to determine σ_Z for the construction of models for Kepler 11d and e (each based on the depleted reservoir of solids left by the preceding planet). For the models of Kepler 11f and g, which start inside the orbits of preceding planets at significantly later times, the depleted mass in solids is redistributed interior to $\approx 1.3\,a_i^e$ (down to their observed orbital radii).

Typically, models make a transition from disk to photospheric boundary conditions (see Section 2.1) at the isolation time, $t_{\rm iso}$. Although in some models gas accretion can be disk-limited during late stages of formation, as for in situ models a proper phase of rapid gas accretion (i.e., R_p significantly smaller than $R_{\rm A}$) is never reached during the formation phase. Accretion of solids could in principle (and does on occasion) continue beyond the isolation time, until the feeding zone is emptied (which requires $da/dt \approx 0$). However, since orbital migration becomes very slow much earlier than $t_{\rm iso}$ (see Figures 6 and 7), M_c plateaus well before isolation is achieved, as can be seen in the left panels of Figures 6 and 7. For all practical purposes, a planet is isolated from both the disk's gas and solids at $t > t_{\rm iso}$. Some properties of the reference models of Kepler 11 planets at $t = t_{\rm iso}$ are listed in Table 5. The small scatter in isolation times is likely caused by the removal of gas via accretion on the planet (when $a > r_{\rm crt}$), which tends to lower the accretion rate through the disk for $r \lesssim a$ (Lubow & D'Angelo 2006, see also Equation (11)) and thus operates in concert with disk photo-evaporation to augment gas depletion inside $r \approx a$. In fact, the time $t_{\rm iso}$ is shorter for planets with larger envelope masses, i.e., with larger $\langle \dot{M}_e \rangle$. However, the contribution of $\dot{M}_e$ to $\dot{\Sigma}_{\rm pe}$ is quite marginal in these calculations. In the more realistic situation in which all planets migrated in the disk, the time $t_{\rm iso}$ would be set by the largest planet, Kepler 11e. However, since the formation phases of all planets are basically complete by that time, no significant consequences would be anticipated.

The relative gas content is largest for Kepler 11e, accounting for $\approx 17\%$ of the total mass at $t_{\rm iso} \approx 4$ Myr, and somewhat less at 8 Gyr (see Table 4). The light elements (H+He) in the other planets make $\lesssim 10\%$ of the total mass

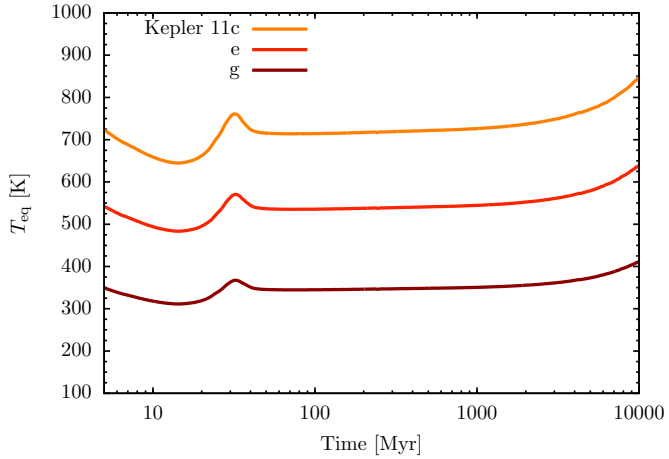

Figure 8. Equilibrium temperature in the radiation field of the star, Equation (5), from the stellar model of Siess et al. (2000) in Figure 2. The temperature is plotted at the final orbital radius of planets Kepler 11c, e, and g (see Table 4), as indicated.

at the isolation time and, in most cases, only a few to several percent at 8 Gyr. At this age, however, the gaseous envelope always accounts for $\approx 35\%$ to $\approx 50\%$ of the planet radius. For all planets, the condensible mass fraction of H_2O is $\gtrsim 39\%$, indicating that their cores mostly form behind the ice condensation line. Although the composition of the initial core is dictated by the local disk composition of the solids at $t = t_i$, its mass ($0.1\,M_\oplus$) is small enough to not affect the final core composition much. Kepler 11b contains the smallest mass fraction of H_2O and the largest mass fractions of silicates and iron, due to its small initial orbital radius (≈ 2 au) and early start time, $t_i \approx 6 \times 10^4$ yr. Nonetheless, also in this case the substantial fraction of H_2O ($\approx 39\%$ by mass) implies that the planet accumulates its condensible inventory mostly behind the ice condensation front. Despite an equally small starting orbit, the core composition of Kepler 11f is instead more similar to that of neighboring planets because of its late start time ($t_i \approx 1.1$ Myr) and growth in a colder disk environment.

Except for the varying stellar properties (see Figure 2), the isolation evolution of ex situ models behaves as that of in situ models. The surface temperature of the planet closely follows the equilibrium temperature, $T_{\rm eq}$, which is shown in Figure 8 for the isolation evolution of Kepler 11c, e, and g.

As for in situ models, the planet radius R_p decreases on a short timescale once the planet becomes isolated. Afterwards, R_p steadily declines as the planet cools. The radius of planets Kepler 11c and d reaches a minimum at an age between 7 and 7.5 Gyr, after which the envelope begins to slowly expand, following the rise of $T_{\rm eq}$ (see Figure 8). However, the expansion is very modest and by an age of 12 Gyr, R_p increases over its minimum value by $< 1\%$. Kepler 11f follows a similar trend, achieving a minimum radius around the age of 7.5 Gyr and then inflating slightly (R_p changing by $< 1\%$). Possibly due to their more massive envelopes and hence larger internal energy, the simulated planets Kepler 11e and g still contract at an age of ≈ 11 Gyr.

The evaporative loss of envelope gas, caused by the absorption of stellar X-ray and EUV photons and given by Equation (8), starts at $t = t_{\rm iso} \approx 4$ Myr, i.e., as soon as the gaseous disk interior to the planets' orbit is cleared and the isolation phase begins. As for in situ models, a stan-

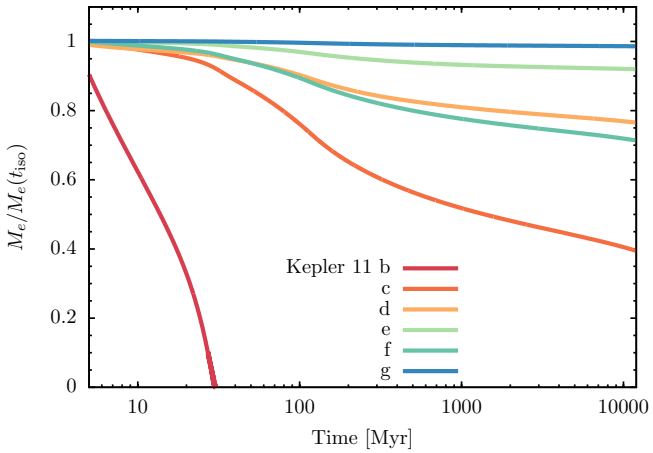

Figure 9. Normalized envelope mass, M_e, as a function of time during the phase of evaporative mass loss, after the planets become isolated from the disk. The envelope (H+He) mass is normalized to M_e at $t = t_{\rm iso}$ (see Table 5). By $t = 5$ Myr, the simulated Kepler 11b planet has already lost about 10% of its H+He mass at $t = t_{\rm iso}$.

dard value for the efficiency parameter, $\varepsilon = 0.1$, is applied (but see also Section 4.2). The resulting envelope masses versus time are illustrated in Figure 9. The rate $|\dot{M}_e|$ is especially large at early ages, $t \lesssim 100$ Myr, because both R_p and the flux $F_{\rm XUV}$ (see Section 2.3) are large. Values of the gas loss rates, averaged over the first 100 Myr (10 Myr for Kepler 11b) of evolution, are listed in Table 5 and range from 10^{-10} to around $6 \times 10^{-10}\, M_\oplus\, {\rm yr}^{-1}$, i.e., between $\approx 10^{10}$ and $\approx 10^{11}\, {\rm g\, s}^{-1}$. Mass loss is significant for the inner planets Kepler 11b, c, and d. By 8 Gyr these planets lose, respectively, 100%, ≈ 57%, and ≈ 22% of their M_e at $t = t_{\rm iso}$. Envelope loss is also substantial for Kepler 11f, which loses nearly 29% of its gaseous mass during the isolation phase. In relative terms, Kepler 11e and g are more immune to evaporative mass loss, as M_e reduces by about 8% and 2%, respectively, from ≈ 4 Myr to 8 Gyr. Of the H+He mass removed during isolation, at least 38–40% evaporates within ≈ 100 Myr. As planets contract, $R_p/R_{\rm H} \ll 1$ hence $K(\xi) \approx 1$ in Equation (8), and H+He gas is stripped from the envelope at a rate $\dot{M}_e^{\rm iso} \propto R_p^3/(M_p a^2)$. After 8 Gyr, mass-loss rates become quite small for all planets, ranging from around 10^{-13} (for Kepler 11f and g) to $\approx 10^{-12}\, M_\oplus\, {\rm yr}^{-1}$ (for Kepler 11c and d).

Comparing the evolution of R_p in Figures 3 and 6 after isolation, one can see that planets formed in situ remain somewhat more inflated than do planets formed ex situ. The difference is especially large for the case of Kepler 11b, probably due to the fact that the planet formed in situ acquires a more massive H+He envelope (because of the rapid core growth). Differences tend to vanish at later times. This behavior accounts for the differences in the average rates $\langle \dot{M}_e \rangle$ in Tables 3 and 5. Although there is a factor of 10 difference in the gas loss rates between in situ and ex situ models of Kepler 11b, in this case, the difference is immaterial since both simulated planets lose their entire envelopes within 30–40 Myr.

4.2. *Results for Individual Planets*

The main results from our ex situ reference models can be summarized as follows.

Kepler 11b. at an initial orbital distance of 2.14 au ($t_i \approx 6.3 \times 10^4$ yr) and a surface density of solids $\sigma_Z \approx 9\, {\rm g\, cm}^{-2}$, according to Equation (7) a non-migrating core would achieve a final mass of $\approx 0.7\, M_\oplus$, and smaller if depletion via scattering (Equation (18)) was taken into account. About 90% of the core mass is accreted from solids orbiting beyond 0.5 au from the star, hence the presence of large amounts of H_2O in the planet. The envelope mass is maximum around 2.8 Myr, before part of it becomes unbound and is released back to the disk. After the planet becomes isolated, the remaining H+He gas is removed by stellar X-ray and EUV radiation within ≈ 30 Myr. Reducing the efficiency of the evaporative mass-loss rate, ε in Equation (8), allows the planet to retain an atmosphere for somewhat longer. However, even a value as low as $\varepsilon = 0.01$ predicts a complete removal of the primordial H+He gas within a few times 100 Myr (see Figure 6). Despite the presence of abundant H_2O in the core (≈ 40% by mass), R_c is still significantly smaller than the observed radius. Although not included, this model naturally accounts for the formation of a steam atmosphere that was proposed to reconcile simulated and observed radii (Lopez et al. 2012). Both final orbital radius and planet mass agree with measured values (see Figure 10).

Kepler 11c. the planet starts at roughly 4 au ($t_i \approx 1.3 \times 10^5$ yr) and grows about 90% of its condensible final mass at $r \gtrsim 0.8$ au. Nearly 46% of the planet's final mass is in H_2O, the second largest (after Kepler 11f) relative fraction of all simulated planets (although Kepler 11d, e, and g contain more H_2O in absolute measure). When the local disk disperses and the planet becomes isolated, the envelope includes about 5% of M_p. Roughly 90% of this H+He mass is accreted from the disk's gas at $170 \lesssim T \lesssim 460$ K. Over the course of the isolation phase, stellar radiation removes more than half of the envelope mass, leaving only ≈ 2% of M_p in primordial H+He gas at 8 Gyr, the smallest relative fraction in all simulated planets that retain an envelope. The evolution of R_p in Figure 6 shows a period, between $t \approx 20$ and ≈ 40 Myr, in which the planet contraction slows down. This feature is likely associated with the rise in $T_{\rm eq}$ at that age (see Figure 8), following the brightening of the star (Figure 2). A similar feature appears in the radius evolution of Kepler 11b and f planets, which can more promptly respond to changes in the external incident flux having (with Kepler 11c) the least massive envelopes. The final planet mass and radius agree with measurements, whereas the final orbital distance is just above the one-standard-deviation upper limit of the measured value (0.108 au).

Kepler 11d. the starting orbital radius is less than 1 au larger than that of Kepler 11c and the start time is comparable ($t_i \approx 1.4 \times 10^5$ yr). Therefore, similarly to its inner neighbor, the planet accumulates ≈ 90% of M_c outside of ≈ 0.9 au. The maximum value of M_e is attained shortly prior to 2.5 Myr, but afterwards some envelope gas becomes unbound and returns to the disk. For ≈ 1 Myr prior to isolation, R_p remains very close to the accretion radius $R_{\rm A}$, preventing further accretion of gas. During its evolution in isolation, the envelope loses somewhat less than $0.1\, M_\oplus$, about a fifth of M_e at $t = t_{\rm iso}$. Comparing the core radii in Tables 4 and 5, a small difference can be noticed. The core masses at $t = t_{\rm iso}$ and at 8 Gyr are virtually identical, yet the pressure applied at the top of the core at the later epoch is nearly twice as large (≈ 9 GPa vs. ≈ 4.8 GPa) because of the cooler temperature, which in this case accounts for the 85 km reduction in R_c. The values of the planet's mass and radius and the orbital distance at 8 Gyr

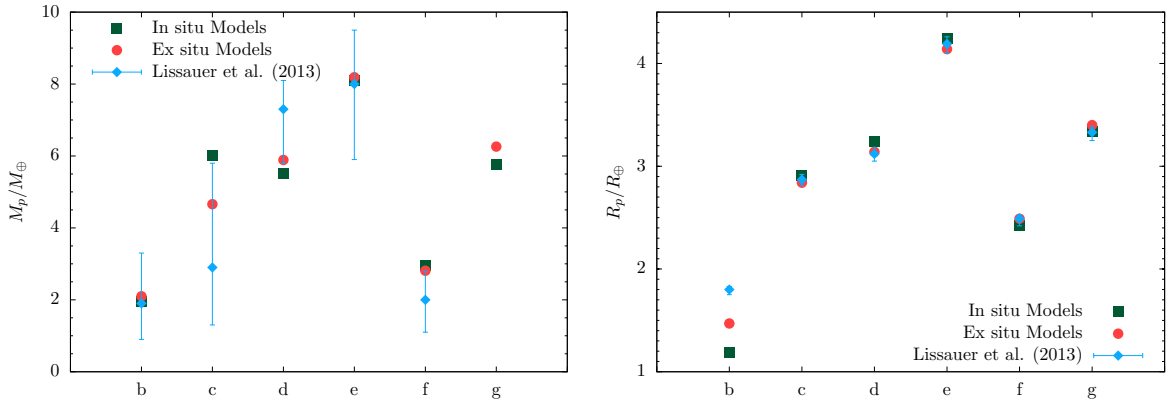

Figure 10. Comparison between results from simulated planets and data from L13: planet mass (left) and planet radius (right). The mass of Kepler 11g is only loosely constrained by transit observations ($M_p < 25\,M_\oplus$). The final orbital distances from ex situ models are in very close agreement with measurements (compare entries in Tables 2 and 4) and are not plotted.

are all within measurement errors.

Kepler 11e. the most massive of the six, in terms of both core and envelope mass, this planet also has the farthest initial orbit at 5.35 au ($t_i \approx 1.5\times10^5$ yr) from the star. The initial local density of solids is $\approx 3\,\mathrm{g\,cm^{-2}}$. Neglecting scattering, a non-migrating planet at that distance would achieve a final core mass of around $2\,M_\oplus$ before emptying its feeding zone. The planet grows 90% of its core mass beyond ≈ 1 au, but most of its H+He inventory is accreted inside this radius. Essentially, the planet's core fully forms behind the ice condensation line ($\approx$ 49% of M_c is H_2O). The average mass-loss rate at the beginning of the isolation phase ($-\langle\dot{M}_e\rangle$, see Table 5) is higher than that of Kepler 11d despite the larger mass and orbital radius of Kepler 11e. The reason is the strong dependence of $\dot{M}_e^{\rm iso}$ in Equation (8) on planet radius. In the case of Kepler 11d, R_p drops below $6\,R_\oplus$ by ≈ 10 Myr, whereas the radius of Kepler 11e remains $> 6\,R_\oplus$ well after 100 Myr (see Figure 7). In absolute terms, the planet loses the second largest amount of primordial H+He during the isolation phase ($0.11\,M_\oplus$). The difference in R_c between $t = t_{\rm iso}$ and $t = 8$ Gyr is again caused by the pressure difference at the bottom of the envelope. The final values of a, M_p, and R_p all agree with measurements.

Kepler 11f. the observed mass of the planet is significantly smaller than those of its neighbors, possibly suggesting a formation at a smaller orbital distance. To achieve a correspondingly smaller core mass with our σ_Z, the planet's initial orbit is interior to the initial orbits of the other planets. Consequently, the planet requires a late start, $t_i \approx 1.1$ Myr, to avoid crossing other orbital paths[4]. The assembly of the core takes place for the most part beyond ≈ 0.6 au and at disk temperatures of $T \lesssim 160$ K. As a result, the core composition is very similar to that of fully hydrated planetesimals (50% H_2O and 45% silicates by mass). Though rich in H_2O in relative terms, 47% of M_p (the richest, in fact), because of its small mass the planet contains an amount of H_2O ($1.3\,M_\oplus$) greater only than the H_2O mass of Kepler 11b. During the evolution in isolation, stellar radiation strips off about 29% of the H+He gas accreted during the formation phase. At 8 Gyr, the planet is left with a gas content of 2.5% by mass. The final planet radius and orbital distance agree with observations, whereas the final total mass, $2.81\,M_\oplus$, is close to the one-standard-deviation upper limit of the measured value ($2.8\,M_\oplus$).

Kepler 11g. similarly to its inner neighbor, the planet starts its simulated evolution at an advanced stage of the disk's life ($t_i \approx 7\times10^5$ yr) in between the initial orbits of Kepler 11c and d. Roughly 90% of its condensible inventory is collected beyond ≈ 1 au, and all of the core is accumulated behind the ice condensation front. In fact, its formation occurs at disk temperatures below ≈ 170 K and its core has virtually the same composition as that of fully hydrated planetesimals. Partially hydrated planetesimals account for only 0.03% of the core mass. Mass loss during isolation is negligible, and the planet basically contracts at a constant mass. Again, the core shrinks somewhat as the envelope cools down and the applied pressure at R_c increases. The planet radius at 8 Gyr is just above the one-standard-deviation upper limit of the measured value ($3.39\,R_\oplus$), whereas a_f agrees with measurements. The planet mass is not really constrained by transit observations, but the value provided by this ex situ model is consistent with that from the in situ calculations in Table 2. Both simulations point at a planet somewhat less massive than Kepler 11e and of comparable mass to that of Kepler 11d.

4.3. *Effects of Changes in Model Assumptions*

The reference models use a standard value of $\varepsilon = 0.1$ in the expression of $\dot{M}_e^{\rm iso}$, to account for re-radiation of the EUV and X-ray stellar flux by the envelope (see Section 2.3). Since this parameter is uncertain, the evolution in isolation was repeated by applying values of $\varepsilon = 0.05$ and 0.15. Results for the evolution of R_p are plotted in Figure 11. The case of Kepler 11b is omitted for obvious reasons. The solid curves of each pair (upper curve for the smaller efficiency) bracket the excursion of R_p (colored regions). Within the considered range of ε, the impact on the radius at 8 Gyr is typically small. For Kepler 11g and e, the relative excursion of M_e amounts to about 1% and 9%, respectively, and the percentile variations of R_p are 0.4% and 2%. The excursion of M_e is larger for Kepler 11d (26%) and larger still for Kepler 11f ($\approx$ 40%), owing to its small mass. The relative change in R_p, though, is $\lesssim 5\%$ for either. In all these cases, the simulated planets would still provide reasonable matches to the observed planets, with M_p and R_p lying within or proximate to measurement

[4] This solution is unlikely unique, and an earlier start may be possible together with a wider initial orbit and a lower σ_Z. In this case, however, the slower growth of M_c would entail larger gas densities to account for the required amount of orbital migration.

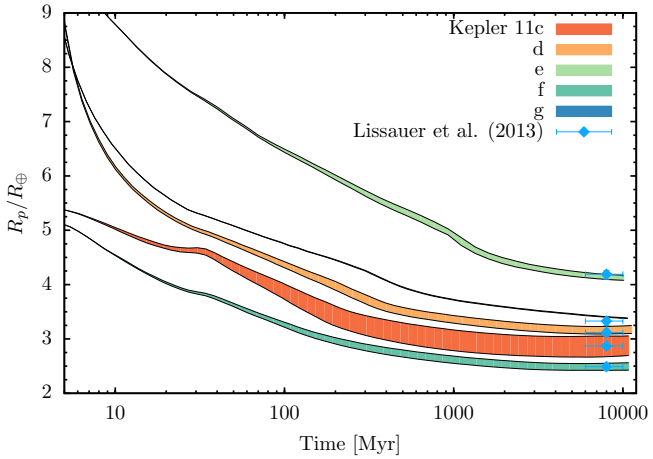

Figure 11. Evolution of the radius of the simulated Kepler 11 planets during the isolation phase for a range of evaporative mass-loss rates, $\dot{M}_e^{\rm iso}$. The efficiency parameter for the absorption of energetic stellar photons in Equation (8) is, respectively, $\varepsilon = 0.15$ (lower solid curves of pairs) and 0.05 (upper solid curves of pairs).

ranges. Due to its vulnerability to mass loss, Kepler 11c represents the most extreme case, with M_e changing by a factor of three and R_p by $\approx 14\%$, which would place the planet radius well outside of the measurement range.

The reference models are based on time-dependent stellar properties for a $1\,M_\odot$ ([Fe/H]$= 0.0$) star computed by Siess et al. (2000). In order to determine the impact of the stellar evolution model, which enters the calculations through Equations (5), (8), and (16), a simulation of Kepler 11b was performed with the Yonsei-Yale stellar model (Spada et al. 2013) in Figure 2 (see the figure's caption and Section 2.1 for further details), starting from the same disk's initial conditions as in the reference model. The three equations depend on $L_\star$ ($T_\star^4 R_\star^2 \propto L_\star$, although Equation (16) separately depends on $R_\star$ as well). The largest differences in stellar luminosity between the two stellar models occur for $t \lesssim 20\,$Myr, i.e., during the disk-embedded phase and the early isolation phase of the planet. The Yonsei-Yale stellar model predicts lower luminosities, which tend to produce a somewhat cooler disk in regions where stellar irradiation is important in the energy budget of the gas (Equation (12)). The cooler temperature in turn reduces the disk thickness and hence affects the migration rate, since $|da/dt| \propto (a/H)^2$ (see Equation (22)). The cooler temperatures during the nebular stage of the planet's evolution also change the Bondi radius $R_{\rm B}$, and hence the planet accretion radius $R_{\rm A}$ in Equation (1). By using the same initial orbital radius, a_i, as in the reference model (see Table 4), the somewhat larger (in magnitude) migration speed requires a later start time, $t_i \approx 1.4 \times 10^5\,$yr (the difference in luminosity is especially large for $t \lesssim 3 \times 10^5\,$yr, see Figure 2). The resulting model provides an isolation time of $t_{\rm iso} = 4.1\,$Myr and values at $t = t_{\rm iso}$ in very good agreement with those in Table 5. During the isolation phase, the surface temperature of the planet differs by $\lesssim 20\,$K relative to that of the reference model. The H+He envelope is entirely removed by $t \approx 30\,$Myr, as in Figure 6. Because of the cooler gas temperatures and later start, the core contains a slightly larger H_2O fraction ($\approx 43\%$ vs. $\approx 39\%$ by mass).

Since the isolation phase of Kepler 11b does not last long, a calculation with the Yonsei-Yale stellar model was also performed for the isolation phase of Kepler 11c. The properties of the model at $t_{\rm iso}$ are those of the reference model listed in Table 5. For most of the isolation phase ($t \gtrsim 50\,$Myr), the stellar luminosity of the Yonsei-Yale stellar model is around 9% lower, compared to $L_\star$ of the Siess et al. model, and thus $T_{\rm eq}$ is only marginally different. The calculation results in an envelope mass at 8 Gyr of $0.11\,M_\oplus$ and a planet radius of $2.88\,R_\oplus$. Both numbers are a little larger than the values in Table 4, but within the errors of the measured mass and radius of Kepler 11c. Clearly, the stellar evolution model does not affect the simulated planets significantly.

Dust grains, either entrained in the accreted gas and/or produced by ablation of accreted solids, can pollute planetary envelopes at temperature $T \lesssim 1500\,$K (assuming silicate grains). In such cases, dust opacity regulates the envelope cooling rate and hence the planet's contraction timescale (e.g., Pollack et al. 1996; Hubickyj et al. 2005). The calculations presented here are based on the opacity plotted in the top panel of Figure 1, which assumes a maximum grain radius of 1 mm. To evaluate the effect of grain opacity in the envelope of the reference models, calculations were also performed by using the table plotted in the bottom panel of Figure 1, which assumes a maximum grain radius of 10 mm. The ratio of the grain-dominated, Rosseland mean opacities in the two tables is about eight. The lower opacity provided by the size distribution with larger dust grains is expected to facilitate cooling and allow for higher gas accretion rates. The planet Kepler 11b, which accumulates the least massive H+He envelope, was simulated with the lower grain opacity. By using the same initial conditions for both disk and planet as for the reference model, the calculation provides values of $\dot{M}_e$ that are initially a few times as large as those of the reference model. The envelope mass achieves a maximum value of $M_e \approx 0.035\,M_\oplus$ at a time $t \approx 2.6\,$Myr, after which the envelope loses mass to the disk as R_p tends to exceed the accretion radius $R_{\rm A}$. The planet attains isolation at a time $t_{\rm iso} = 4.1\,$Myr. Despite the larger envelope mass during the planet's early accretion history, the core mass at $t_{\rm iso}$ is again $M_c = 2.1\,M_\oplus$ and $M_e = 0.013\,M_\oplus$ (about twice as large as that of the reference model), which is entirely removed by stellar radiation by an age of $\approx 33\,$Myr.

Although the opacity test indicates little impact on the simulated Kepler 11b planet, larger effects are to be expected for planets that accumulate higher H+He mass fractions. Indeed, the same test repeated for the most massive planet, Kepler 11e, results in an entirely different outcome. The planet reaches a crossover mass ($M_e = M_c$) of $\approx 7.2\,M_\oplus$ at $t \approx 2\,$Myr and enters the transition stage (see Section 2.1) of fast – and disk-limited – gas accretion by $t \approx 2.2\,$Myr. On its track to becoming a Hot Jupiter, the planet reaches a mass of $\approx 0.7\,M_{\rm J}$ by $t \approx 2.5\,$Myr. The tendency to evolve into a giant planet, with the lower dust opacity of Figure 1 (bottom panel), is also obtained from in situ calculations. Ex situ models matching the observed radius of Kepler 11e with the lower opacity require a smaller core mass and, hence, a tighter initial orbit ($a_i \approx 4.8\,$au). A calculation resulting in $R_p = 4.18\,R_\oplus$ at 8 Gyr provides a mass $M_p = 5.55\,M_\oplus$, below the one-standard-deviation lower limit of the measured value of $5.9\,M_\oplus$. A calculation resulting in $M_p = 5.96\,M_\oplus$ produces a radius $R_p \approx 4.5\,R_\oplus$, well over the one-standard-deviation upper limit of the measured value of $4.26\,R_\oplus$. Similarly, in situ formation models indicate that R_p can be matched with a mass M_p somewhat smaller than the

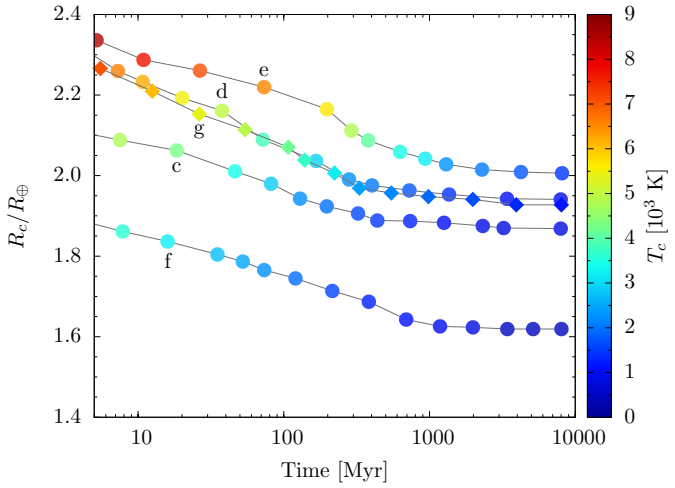

Figure 12. Core radii of Kepler 11 planets, as indicated, calculated from the thermal structures described in Appendix A. The calculations apply pressure (P_c) and temperature (T_c) at the core surface derived from ex situ models. Data are color-coded by the temperature T_c. The core radius of Kepler 11g is represented by diamonds instead of circles. Nearly all the difference ΔR_c along each curve is caused by the contraction of the core's H_2O shell. By $t \approx 0.5$ Gyr, R_c is within $\lesssim 3\%$ of its value at 8 Gyr.

measured one-standard-deviation lower limit.

Both in situ and ex situ models assume formation in a disk of 100 km-radius planetesimals. A reduction in planetesimal size from ≈ 100 to ~ 1 km was studied by the authors in other contexts. First, the orbital eccentricities and inclinations of these bodies decrease, and second, the cross section for planetesimal capture in the planetary envelope ($\mathcal{S}_{\rm eff}$ in Equation (6)) increases (see D'Angelo et al. 2014, Figure 6). Both effects enhance the accretion rate of solids, $\dot{M}_c$. Whether the planetesimal size has an effect on the accreted gas mass depends on the ratio of the timescale for the buildup of the core to the disk lifetime. The core buildup timescale of the in situ models is already very short, thus the effect is negligible. In the ex situ models, the core accretion time would decrease (considerably in the case of small planetesimals). The faster core growth would increase the migration rate. The planet would be driven more quickly toward the inner disk regions, where solids' densities are higher but the solids' mass available for accretion is lower. Therefore, the outcome is difficult to predict. We performed tests for Kepler 11d with planetesimals of 10 and 1 km in radius. Compared to the reference case discussed above, the final core mass increased by only about 10% and 15%, respectively.

The data listed in Tables 4 and 5 indicate that there can be marginal changes in core radii during the isolation phase. As mentioned in Section 4.2, these changes arise from differences in boundary pressures caused by contraction, resulting in core compression. Such small changes, however, may be offset by temperature effects through the core. In the calculations discussed above, core thermodynamics is ignored and ex situ models include it only for phase transitions within the silicate mantle (see Section 2.2 and Appendix A). The assumption of neglecting the core thermal stratification is based on previous studies, which argued that thermal pressure should not significantly affect the core radius at these core masses (e.g., Valencia et al. 2006; Seager et al. 2007; Sotin et al. 2007; Sohl et al. 2014b). Nonetheless, for completeness, improved structure models are presented and discussed in Appendix C. These include temperature stratification, energy transfer, and temperature-dependent EoS in a self-consistent fashion; they also include additional material phases. Thermal effects (in H_2O-rich cores) may be relatively important for the determination of R_c during the early stages of the isolation phase ($t \lesssim 0.5$ Gyr, see Figure 12). However, at an age of ≈ 8 Gyr, the differences in R_c between thermal and isothermal cores of the simulated Kepler 11 planets are small, typically $\lesssim 0.5\%$ in most cases and somewhat less than 2% for Kepler 11c. Assessing the impact of thermodynamics for the case of Kepler 11b is more difficult, because the expected steam envelope is not modeled. If the gas pressure and temperature at the bottom of the envelope were, respectively ≈ 1 GPa and ≈ 1000 K, then R_c would be 5% larger than the value listed in Table 4 (see the discussion in Appendix C).

During isolation, planets gradually cool down. The pressure P_c at the bottom of the envelope varies by factors of the order of unity, whereas temperature variations are larger. To make a simple assessment of the impact on R_c of the varying conditions at the core-envelope boundary as planets cool, thermal structure calculations of the cores (see details in Appendix A) were performed by applying pressure and temperature at the core surface during the isolation phase. Figure 12 indicates that there can be significant variations in R_c, up to $\approx 0.34\,R_\oplus$. The symbols in the figure are color-coded according to the core surface temperature, T_c, as obtained from ex situ calculations. However, in the figure, 92–94% of the total difference ΔR_c along each curve is due to the contraction of the cores' H_2O shell. Additional details are given in Appendix C. Assuming $\Delta R_p \approx \Delta R_c$, the inflated cores may result in planet radii larger by $\approx 3\%$ at around the isolation time, which may in turn enhance the evaporative mass-loss rate by $\approx 10\%$ during early isolation times. Results in Figure 11 suggest that the impact on R_p at 8 Gyr may be relatively small.

4.4. *Effects of Changes in Initial Conditions*

Figure 13 illustrates how some properties of the models for Kepler 11d and e at 8 Gyr depend on the surface density of solids, σ_Z, and the initial orbital radius, a_i (see the figure's caption for further details). Where relevant, in situ models are included as well. In the figure, $\sigma_Z^{\rm ref}$ and $a_i^{\rm ref}$ are the reference values of the models discussed in Sections 3 and 4. In the calculations of the top panel, the initial gas density Σ is rescaled so to keep the ratio Σ/σ_Z fixed. The planet mass increases monotonically as σ_Z and a_i increase. In either case, this is a consequence of the larger core mass that facilitates gas accretion, especially at early times. The final envelope mass of in situ models increases monotonically, as it generally (but not always) does also in ex situ models. In the latter calculations, because of the different accretion history (and initial condition a_i), the final orbital radius a_f varies, affecting the evolution of M_e during isolation. The radius R_p tends to grow with the ratio M_e/M_c, which is not always a monotonic function of σ_Z or a_i in ex situ models (see the left panels of Figure 13). Because of the small uncertainties on the observed radius, only initial conditions in the neighborhood of those adopted for the reference models can match observations. The final orbital distance varies by a factor of up to ≈ 1.8 in the ex situ calculations of the top panels and ≈ 1.3 in those of the bottom panels (relative to the reference values, $a_f = 0.156$ and 0.194 au).

The in situ reference models of Section 3 and those rep-

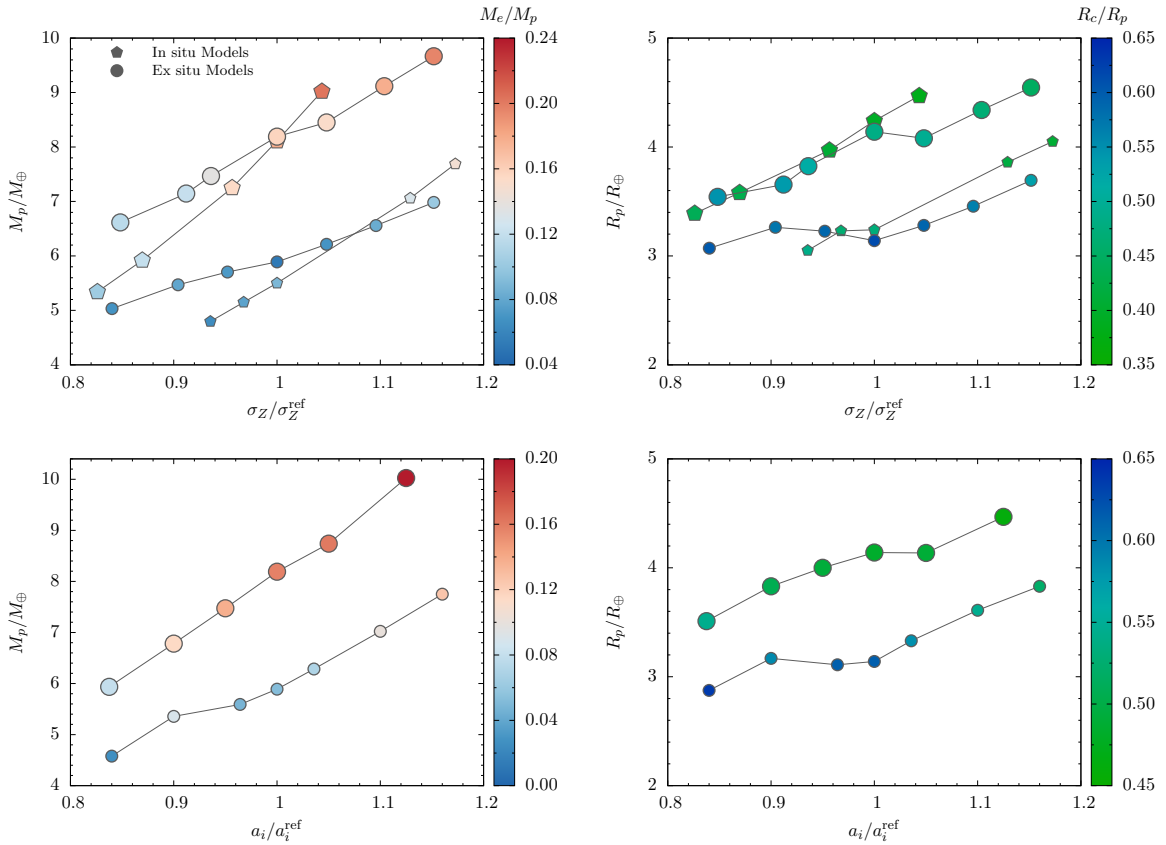

Figure 13. Planet mass and radius at 8 Gyr versus the solids' surface density, σ_Z (top), and the orbit's initial radius, a_i (bottom), for Kepler 11d and e (larger symbols). Data are color-coded by the envelope-to-planet mass ratio (left) and the core-to-planet radius ratio (right). The values of σ_Z and a_i are scaled by those of the reference models listed in Tables 2 and 4. In ex situ models, $\sigma_Z^{\rm ref}$ is similar for the two planets, between 3 and 3.5 g cm^{-2}.

resented in Figure 13 assume an initial disk's gas-to-solid mass ratio of 200. Experiments conducted on Kepler 11e, by using $\sigma_Z = 4600\,{\rm g\,cm^{-2}}$ (as in the reference case) and varying the mass ratio from 50 to 400, resulted in mass and radius changes (at 8 Gyr) of $\lesssim 10\%$. For a gas-to-solid mass ratio of 50, $M_p = 7.7\,M_\oplus$ and $R_p = 3.98\,R_\oplus$ whereas these values increase to $8.46\,M_\oplus$ and $4.44\,R_\oplus$, respectively, for a mass ratio of 400. The planet mass is still within measurement errors, while the planet radius lies outside the observed range by at most a few percent.

5. DISCUSSION

5.1. *Implications of In Situ and Ex Situ Formation*

Both in situ and ex situ simulated planets result in radii, masses, and orbital distances in agreement with measured values at the estimated age of the system. Therefore, it is not possible to distinguish between the two modes of formation from these final properties. The two formation scenarios do, however, provide entirely different perspectives of the environment in which the planets grew, of their compositions, and interior structures.

Figure 14 shows the initial surface density of the gas applied to the in situ (circles) and ex situ models (blue line). The figure also illustrates other reference surface densities (Weidenschilling 1977; Hayashi 1981; Davis 2005; Chiang & Laughlin 2013; Schlichting 2014). As noted above, Σ at $t = 0$ of the ex situ simulations fortuitously matches the surface density constructed by Davis (2005). It should be pointed out that, among these reference density distributions, only those of Chiang & Laughlin (2013) and

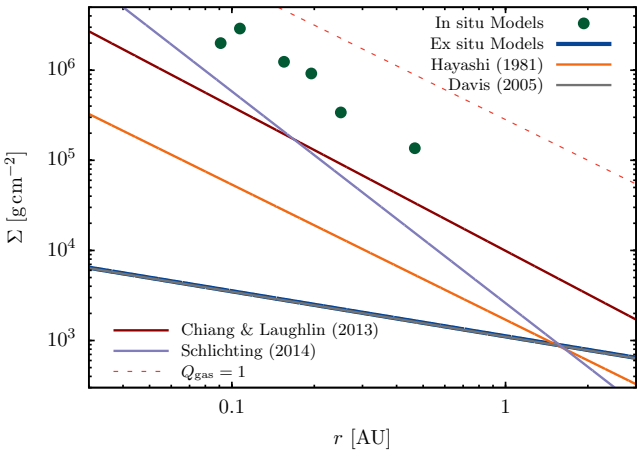

Figure 14. Comparison of the gas surface density required for in situ formation (dots) and ex situ formation (thick blue line, see also Figure 5) of Kepler 11 planets. Also shown in the plot are the minimum-mass solar nebula density of Hayashi (1981) (see also Weidenschilling 1977), and Davis (2005), and the minimum-mass extrasolar nebula density of Chiang & Laughlin (2013) and Schlichting (2014). Fortuitously, the initial Σ for ex situ models closely matches Davis' density distribution. The dashed line represents the density threshold for gravitational instability of the initial gaseous disk, assuming $T = 1000$ K. $Q_{\rm gas}$ is the Toomre stability parameter (e.g., Durisen et al. 2007, pp. 607-622).

Schlichting (2014) were explicitly derived for close-in extrasolar planets. The other two are meant to apply to the solar system and are thus simple extrapolations at the short distances from the star of Kepler 11 planets. The

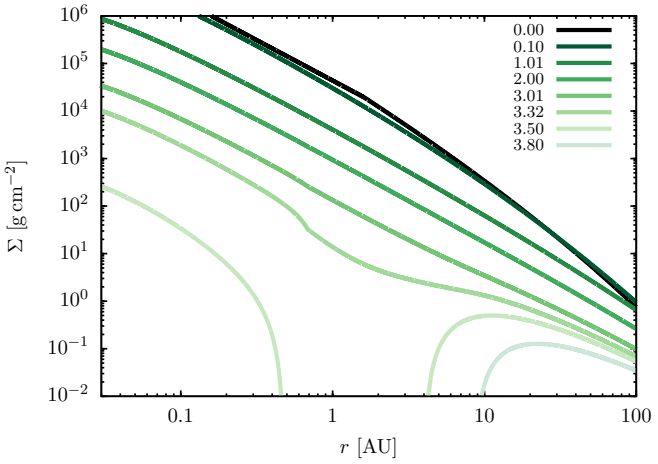

Figure 15. Simulated evolution of the gas surface density applied to in situ models discussed in Section 3. The initial Σ was derived from the required σ_Z, augmented by the gas-to-solid mass ratio. See Section 5 for further details. Times in the legend are in megayears.

dashed line in the figure indicates the gas density above which the disk would be gravitationally unstable to axisymmetric perturbations according to the Toomre stability criterion (Durisen et al. 2007, pp. 607-622), using a constant gas temperature of 1000 K. Even by applying $T = 1000(0.1\,\mathrm{au}/r)\,\mathrm{K}$, appropriate for H/r nearly constant, the initial Σ inferred from in situ models would still be stable (although only marginally stable to non-axisymmetric perturbations).

In situ formation requires a very large σ_Z within ≈ 0.5 au of the star, as illustrated in Figure 14 (see also Bodenheimer & Lissauer 2014). The models discussed here suggest densities of solids between 700 and $1.45 \times 10^4\,\mathrm{g\,cm^{-2}}$ (see Table 2). If most of these solids had to form locally, the initial gaseous mass of the region had to be accordingly large. Given the short accretion timescales involved in the growth process, $\sim 10^4$ yr (see Figures 3 and 4), most of the solids necessary for core assembly had to be available prior to the beginning of this process. Therefore, a gradual replenishment of the solids' reservoir from larger radii might not be a viable alternative to a large σ_Z. Moreover, this possibility would likely lead to a hierarchical system of planets with inwardly decreasing masses, which is inconsistent with the masses of Kepler 11f and e (and probably of Kepler 11g as well).

A disk model aimed at mimicking the evolution of the initial in situ Σ shown in Figure 14 is presented in Figure 15. The disk has an initial mass of $\approx 0.18\,M_\odot$ within ≈ 70 au. Both the kinematic viscosity of the gas and the emission rate of stellar EUV ionizing photons were chosen to induce photo-evaporation of the inner disk at around the age of 3.5 Myr (see Section 3). The region $r \lesssim 1$ au in the disk in Figure 15 is dispersed between $t \approx 3.5$ and ≈ 3.7 Myr. Gas temperatures are initially high, as can also be realized from simple arguments based on energy balance. At high densities, the disk is optically thick in the vertical direction and the main source of energy is viscous heating. Hence Equation (12) reduces to $Q_\nu = Q_{\rm cool}$, which becomes

$$\sigma_{\rm SB}\,T^4 = \frac{27}{128}\left(\Sigma\kappa_{\rm R} + \frac{8}{3}\right)\nu\Sigma\Omega^2, \qquad (25)$$

where $\Sigma\kappa_{\rm R}/2$ is the optical depth of the disk's mid-plane. Since the initial accretion rate through the disk in this case is $3\pi\nu\Sigma \sim 10^{-7}\,M_\odot\,\mathrm{yr}^{-1}$, Equation (25) and Figure 15 imply that, at $r \approx 0.5$ au, temperatures are initially in excess of 2500 K and drop below 1000 K at $t \gtrsim 1$ Myr. At $r \approx 0.1$ au, temperatures become $\lesssim 1000$ K at $t \gtrsim 2.5$ Myr. These high gas temperatures would only allow for the presence in the disk of metals and highly refractory solid species, which would be reflected by the compositions of the cores. The high temperatures also prevent the massive inner disk from becoming gravitationally unstable (Durisen et al. 2007, pp. 607-622). Lowering the kinematic viscosity of the gas would somewhat reduce the gas temperatures ($T \propto \nu^{1/4}$) but would also extend the disk lifetime (by halving ν it would take over 5 Myr to photo-evaporate the inner disk). The effects of the initially high disk temperature and of the disk evolution on the in situ formation process require further calculations.

Ex situ formation can occur in low-mass disks, in which the initial σ_Z increases from $\approx 5\,\mathrm{g\,cm^{-2}}$ at around 7 au to $\approx 10\,\mathrm{g\,cm^{-2}}$ at 0.5 au, the disk region that provides the vast majority of the solids to assemble all the planetary cores. Initial gas densities at these radial distances are in the range from a few times $100\,\mathrm{g\,cm^{-2}}$ to $\approx 1.5\times10^3\,\mathrm{g\,cm^{-2}}$ (see Figure 5). Cores are assembled over timescales of the order of 1 Myr (see Figures 6 and 7). Planets experience relatively low temperatures during their formation phase and spend a long enough time behind the ice condensation line to become enriched in H_2O and other volatile substances (if available).

The percentile composition of the six planets is represented in the histograms of Figure 16, for in situ as well as ex situ models (see the figure's caption for details). Recall that in situ simulations assume a fixed core composition of iron and silicates of 30% and 70% by mass, respectively. In ex situ models, H_2O is assumed to be all condensed in the core, although part of it should be in gaseous form mixed with H+He gas, released by ablating solids passing through the envelope. Both in situ and ex situ calculations predict that the percentile H+He mass of Kepler 11c is comparable to that of the smaller Kepler 11f, because most of the envelope is lost after formation. Kepler 11b simulated in situ acquires a much larger envelope than does the ex situ simulated planet, because the core mass approaches its final value at very early times (compare the growth of M_e in Figures 3 and 6).

In order to reconcile observed and simulated radii of Kepler 11b, the in situ formation scenario requires that gas is sequestered in the core during formation and released afterwards. Outgassing of at least $\approx 10^{-3}\,M_\oplus$ of hydrogen would be sufficient to account for the observed radius. However, outgassing would still need to compete against evaporative gas loss, which would operate at rates between $\approx 10^{-12}$ and $\approx 10^{-11}\,M_\oplus\,\mathrm{yr}^{-1}$. If outgassing began right after the removal of the primordial H+He envelope (at $t \approx 40$ Myr) and continued for the age of the planet, the (average) outgassing rate would only need to be marginally higher than the (average) evaporative gas loss rate. This possibility, however, implies that the amount of gas sequestered in the core during formation ought to be significant in relative terms, between ≈ 0.01 and $\approx 0.1\,M_\oplus$. The details regarding the processes of sequestration and outgassing remain to be investigated, but the result could have important implications concerning the in situ versus ex situ formation of Kepler 11b.

The ex situ formation scenario predicts the presence of a steam atmosphere (not modeled here). Based on previ-

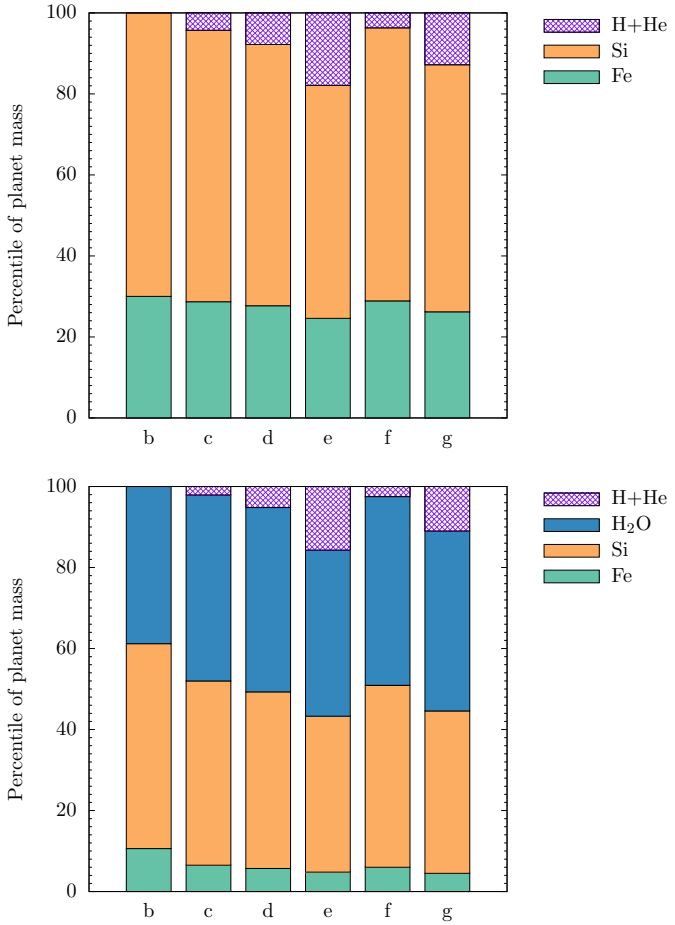

Figure 16. Histogram of the fractional composition of simulated Kepler 11 planets. 'Fe' indicates the iron nucleus of the core, 'Si' the silicate mantle surrounding the nucleus, H_2O the outer ice/water core shell, and 'H+He' the planet's envelope gas. In case of Kepler 11b, the H_2O mass fraction does not account for the possible removal of atmospheric steam. The top/bottom panel displays results from in situ/ex situ models. In situ calculations assume fixed core mass fractions of Fe (30% by mass) and silicates (70% by mass).

ous assessments of the planet mass and radius (Lissauer et al. 2011a), Lopez et al. (2012) estimated that the planet radius can be matched by a water-world whose composition is about 40% H_2O by mass, comparable to the H_2O content of the simulated ex situ planet (see Table 4). Assuming a hydrostatic and adiabatic atmosphere with an ideal EOS for H_2O, the mass M_e necessary to match the observed radius is $\approx 7\times10^{-3}\,M_\oplus$, though non-ideal effects in the EOS may reduce this estimate. Because of the larger mean molecular weight, evaporative mass loss of H_2O by stellar radiation should be less significant than is loss of lighter elements. Additionally, steam can be replenished by the condensed core. Since hydrogen can mix with H_2O at the pressures and temperatures of planetary interiors (Soubiran & Militzer 2015), hydrogen may be present in the atmosphere of Kepler 11b as well.

5.2. *On the Mass of Kepler 11g*

Transit observations only place an upper limit of $\approx 25\,M_\oplus$ on the mass of Kepler 11g (L13). Assuming negligible amounts of gas in the envelope, an ex situ type composition of 5% iron, 45% silicates, and 50% H_2O by mass, would result in a radius of $2.8\,R_\oplus$, short of the observed value $R_p = 3.33\,R_\oplus$. An in situ type composition

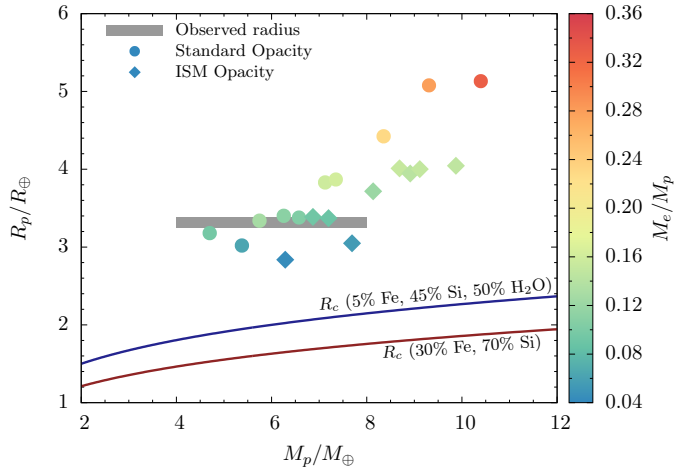

Figure 17. Planet radius versus planet mass for various simulations of Kepler 11g. Circles refer to models adopting the standard opacity table (with dust grains up to 1 mm in radius, see Figure 1). Diamonds refer to models adopting an interstellar medium-type distribution of grains (up to 1 μm in radius), described in D'Angelo & Bodenheimer (2013). The planet gas content is rendered by the color scale. Also plotted are the core radii for the interior compositions of Kepler 11g from in situ (lower solid curve) and ex situ simulations (upper solid curve).

would result in an even smaller radius ($2.3\,R_\oplus$). Hence, the planet must bear a gaseous envelope.

Both in situ and ex situ models indicate that Kepler 11g is somewhat less massive than Kepler 11e and of comparable mass to Kepler 11d. It is reasonable to imagine a scenario in which a lower core mass may attract a sufficiently large envelope to account for the observed radius. In fact, another simulation of Kepler 11g (with different start conditions) results in a radius only marginally smaller than that observed and $M_p \approx 4.7\,M_\oplus$. Even smaller masses might be attained, e.g., by lowering the dust opacity in the planet's envelope. However, the opposite scenario of a much more massive planet and a smaller M_e/M_p ratio may be more difficult to realize.

Figure 17 shows outcomes from additional ex situ simulations of Kepler 11g. In these models, the start conditions of the reference model (t_i, a_i, and initial σ_Z) were changed with the aim of obtaining different planet masses and gas-to-condensible mass ratios. The final orbital radii are within roughly 10% of the observed orbital distance. Circles represent simulations that apply the grain opacity of the top panel of Figure 1, as in reference models. Data points are color-coded by their relative gas content, M_e/M_p. The solid lines indicate the core radius corresponding to the interior composition of in situ (30% iron and 70% silicates) and ex situ models (see Table 4), assuming a pressure at R_c of 1 GPa and $T = T_{\rm eq}$. The observed radius of the planet, within measurement errors, is indicated by the gray-shaded area. The data points include the in situ simulation of Table 2 as well. This model has a comparatively large gas content for its radius, owing to the smaller value of R_c (i.e., the difference $R_p - R_c$ is in fact comparably large).

From the data plotted in Figure 17, it appears difficult to reconcile observed and simulated radii for planets more massive than about $7\,M_\oplus$. In fact, when $M_p \gtrsim 7\,M_\oplus$, the H+He mass fraction M_e/M_p tends to exceed $\approx 16\%$, resulting in too large a radius. In the calculations reported herein, the value of M_e at the end of the formation phase is set by dispersal of the gaseous disk. The model with largest

mass in Figure 17 has $M_e \gtrsim 2.5\,M_\oplus$ ($M_e/M_p \gtrsim 0.28$) and R_p far larger than observed. If under different circumstances the accretion of gas was starved by disk dispersal at an earlier age and R_p at 8 Gyr was similar to the observed value, the planet mass would not exceed $\approx 8\,M_\oplus$ (an envelope mass somewhat smaller than $1\,M_\oplus$ appears necessary to account for the observed radius).

According to L13, an $M_p \approx 15\,M_\oplus$ planet with a 6.6% gas content by mass can match the radius of Kepler 11g. It may be possible to build a large core mass without attracting an excessively large envelope by augmenting the opacity in the envelope, which operates to slow contraction and inhibits gas accretion. This possibility was tested by using dust opacities calculated from an interstellar medium-type grain distribution, with dust grains of up to $1\,\mu$m in radius (for details, see D'Angelo & Bodenheimer 2013). Results from this second set of models are represented by diamonds in Figure 17. As expected, for a given M_p, the ratio M_e/M_p is smaller than in the other set of simulations, yielding smaller planetary radii. Nonetheless, as M_p grows beyond $\approx 8\,M_\oplus$, $M_e/M_p \gtrsim 0.2$ and R_p becomes too large to match observations. Clearly, other scenarios can be envisaged (e.g., most of M_c is accumulated toward the end of the disk lifetime, delaying envelope growth), although they must be compatible with the formation of the inner planets. Within the assumptions adopted herein, both in situ and ex situ models argue in favor of a mass smaller than or comparable to Kepler 11e's mass.

6. CONCLUSIONS

We constructed models of formation and long-term evolution of the six Kepler 11 planets. Both in situ and ex situ scenarios were considered. The simulations presented here take into account many physical aspects of the formation and evolution processes in detail (see Section 2). Approximations were nonetheless necessary in order to render the problem tractable. A major limitation of this study is the neglect of planet-planet interactions. Although it is not possible to speculate about the impact of this deficiency on the results, especially in regard to orbital stability of planets and capture into mean-motion resonances, N-body simulations did show that compact planetary systems, and the Kepler 11 system in particular, may indeed originate in the presence of disk-driven orbital migration (Hands et al. 2014).

Both in situ and ex situ models appear equally capable of generating planets whose radii, masses, and orbital distances (when relevant) at the estimated age of ≈ 8 Gyr agree with those measured via transit observations (see Sections 3 and 4). Based exclusively on these final outcomes of the simulations, it seems difficult – and certainly not obvious – to argue in favor of one scenario over the other. The implications of the two formation scenarios are, however, significantly and profoundly different (see Section 5).

In situ formation may only work if a large amount of solids is available for accretion within $r \lesssim 0.5$ au of the star. The models built here predict a surface density of solids $7 \times 10^2 \leq \sigma_Z \leq 1.45 \times 10^4\,\mathrm{g\,cm^{-2}}$ (see Table 2) and a mass in solids of $\approx 50\,M_\oplus$ inside ≈ 0.5 au. Initial gas densities in the disk are expected to be accordingly high ($\gtrsim 10^5\,\mathrm{g\,cm^{-2}}$, see Figure 15). Planets form at disk temperatures of over 1000 K, hence their cores may only contain metals and refractory materials. The large values of σ_Z also result in extremely short assembly times of the cores (of the order of 10^4 yr, see Figures 3 and 4). Kepler 11b, which is completely stripped of its primordial H+He envelope during the isolation phase (a fate that appears unavoidable!), must have a tenuous atmosphere continuously replenished over time, or generated at a late age, by the release of gas sequestered in the core. More detailed modeling is required, taking into account the release of hydrogen as well as the evaporation of the atmosphere, to determine if this picture is reasonable.

Ex situ formation may work in low-mass disks. The models built here are based on a disk whose distribution of solids at $t = 0$ is $5 \lesssim \sigma_Z \lesssim 10\,\mathrm{g\,cm^{-2}}$, proceeding inward from ≈ 7 to ≈ 0.5 au. The initial gas density in this region ranges from ≈ 100 to $\approx 10^3\,\mathrm{g\,cm^{-2}}$ (see Figure 5). The disk's gas interior to ≈ 1 au is dispersed in about 4 Myr. Cores grow gradually, over timescales of the order of 10^6 yr (see Figures 6 and 7). In all cases, most of the core assembly may be completed beyond the ice condensation line ($T \lesssim 150$ K). Consequently, ex situ formation predicts planetary cores to be rich in H_2O, and possibly in other volatile materials, if hydrated planetesimals bear substantial amounts of ice (as assumed here). Most of the H_2O is at high pressures and temperatures (see Appendix C). Kepler 11b, which loses its entire envelope during isolation, is predicted to have a steam envelope originating from the release of H_2O from the core's outer shell. The gaseous envelopes of the other planets may contain H_2O mixed with hydrogen and helium as well. In fact, since the critical temperature of ice is reached at shallow depths ($T \approx 650$ K), passing solids should shed part of their mass in the outer envelope layers.

Simulations indicate that, from a formation standpoint, it may be difficult for Kepler 11g to become more massive than $\approx 8\,M_\oplus$, collecting only a relatively light envelope (see Section 5). Both in situ and ex situ models point at a planet mass not much greater than $M_p \approx 7\,M_\oplus$ and a percentile gas content between ≈ 10 and $\approx 15\%$.

We thank Uma Gorti for numerous helpful discussions and for her precious guidance during the implementation of the disk photo-evaporation module. We are grateful to an anonymous referee, whose insightful comments helped improve several parts of this paper. G.D. thanks the Los Alamos National Laboratory for its hospitality. G.D. acknowledges support from NASA Outer Planets Research Program grant 202844.02.02.01.75 and from NASA Origins of Solar Systems Program grant NNX14AG92G. Resources supporting this work were provided by the NASA High-End Computing (HEC) Program through the NASA Advanced Supercomputing (NAS) Division at Ames Research Center.

APPENDIX

A. CORE STRUCTURE CALCULATIONS

Here we describe our basic calculations of core structures, i.e., those of the condensible part of a planet, along with improvements intended to check the validity of some of the assumptions and approximations applied in the models discussed above. An important cautionary note: the labels used in this appendix are unrelated to those used elsewhere in the paper.

As anticipated in Section 2.2, the condensed interior of a planet consists of an iron nucleus (hereafter referred to as "core" for conformity with geophysics terminology), surrounded by a silicate mantle, overlaid with an H_2O shell.

Table 6
Equations of state and related thermodynamics quantities

Material	EoS type[a]	EoS	γ	θ_D	α
ϵ-Fe	GR	W11	W11	W11	Eq. (A8)
γ-Fe	BM	K10	W11	W11	Eq. (A8)
α-Fe	BM	K10	W11	W11	Eq. (A8)
Liquid Fe	BM	K10	I14		Eq. (A8)
$MgSiO_3$ppv	GR	W11	S11	S11	K09b
$MgSiO_3$pv	GR	W11	S11	S11	K09b
Mg_2SiO_4	BM	W11	W11	W11	K09a
Ice X	VN	L99	F93	F93	F04
Ice VII	BM	F04	F93	F93	F04
Ice VI	BM	S02	F93	F93	S05
Ice V	BM	S02	F93	F93	F05
Ice III	BM	S02	F93	F93	F05
Ice Ih	BM	S02	F93	F93	T98
Water	BM	S90	S05		S90
Water	IAPWS	W02	W02		Eq. (A8)

References. — Fei et al. (1993, F93); Fortes et al. (2005, F05); Frank et al. (2004, F04); Ichikawa et al. (2014, I14); Katsura et al. (2009a, K09a); Katsura et al. (2009b, K09b); Komabayashi & Fei (2010, K10); Loubeyre et al. (1999, L99); Sohl et al. (2002, S02); Stewart & Ahrens (2005, S05); Stamenković et al. (2011, S11); Stixrude & Bukowinski (1990, S90); Tanaka (1998, T98); Wagner & Pruß (2002, W02); Wagner et al. (2011, W11).

[a] Generalized Rydberg (GR); 3rd-order Birch-Murnaghan (BM); Vinet (VN); see Stacey & Davis (2008) for a review. The last entry is for IAPWS ordinary water.

The core material can transition among the iron allotropes α-Fe, γ-Fe , ϵ-Fe[5], and liquid iron, according to the P-T phase diagrams of Kerley (1993) and Anzellini et al. (2013). The silicate mantle can differentiate, with increasing pressure, into olivine (Mg_2SiO_4), perovskite ($MgSiO_3$pv), and post-perovskite ($MgSiO_3$ppv) layers. Here, the transition among these species is regulated by the phase diagrams of Fei et al. (2004) and Tateno et al. (2009). Post-post-perovskite phases (e.g., see the discussion in Stamenković et al. 2011; Wagner et al. 2012) are neglected. The H_2O shell is composed of several types of ice (Ih, III, V, VI, VII, and X) and water, according to the phase curves of Loubeyre et al. (1999), Lin et al. (2004), Lin et al. (2005), and Choukroun & Grasset (2007). The transition to the vapor phase is ignored.

Two fundamental and customary assumptions made in planetary structure calculations are those of spherical symmetry and hydrostatic equilibrium. Indicating with m the mass of the condensed matter interior to radius R, and with P, Q, and T, respectively, the pressure, the heat flux, and temperature at $R = R(m)$, the structure equations read

$$\frac{\partial R}{\partial m} = \frac{1}{4\pi\rho R^2}, \tag{A1}$$

$$\frac{\partial P}{\partial m} = -\frac{Gm}{4\pi R^4}, \tag{A2}$$

$$\frac{\partial Q}{\partial m} = \left(\varepsilon\rho - \frac{2Q}{R}\right)\frac{\partial R}{\partial m}, \tag{A3}$$

$$\frac{\partial T}{\partial m} = -\frac{Q}{N_u k_c}\frac{\partial R}{\partial m}. \tag{A4}$$

[5] The crystal structure of these allotropes is, respectively, body-centered cubic (bcc), face-centered cubic (fcc), and hexagonal close packed (hcp).

$$\frac{\partial T}{\partial m} = \left(\frac{\partial T}{\partial m}\right)_S. \tag{A5}$$

In Equation (A3), ε is the specific energy production rate (due to radiogenic heating produced by radioactive decay, to tidal heating, to accretion heating, to heating/cooling during phase changes, etc.). Heat production in the H_2O shell is set to zero, whereas it accounts for radiogenic heating in the silicate mantle, where a constant value of $\varepsilon = 7.38 \times 10^{-12}\,\mathrm{W\,kg^{-1}}$ (appropriate for the Earth, Turcotte & Schubert 2014) is applied. In the iron core, ε is chosen so that the heat flux across the boundary with the silicate mantle (CMB) is $Q_{\rm CMB} = -k_c(\partial T/\partial R)_{\rm CMB}$ (Valencia et al. 2006; Wagner et al. 2011). For the Earth test considered below, the power through this boundary is $\approx 7\,\mathrm{TW}$, comparable to the lower limit estimated for the Earth (Tateno et al. 2009). Under the assumption of spherical symmetry, the gravitational acceleration $g = Gm/R^2$ is known from the solution $R = R(m)$. In Equation (A4), N_u is the Nusselt number, which gives the ratio of the total (conductive plus convective) to the conductive heat flux through the spherical surface of radius R, and k_c is the thermal conductivity ($N_u = 1$ when the convective heat flux is zero). Equation (A4) is applied to semi-convective layers whereas Equation (A5), which represents the adiabatic temperature gradient (Anderson 1989)

$$\left(\frac{\partial T}{\partial m}\right)_S = \frac{\gamma T}{K_S}\frac{\partial P}{\partial m}, \tag{A6}$$

is applied to vigorously convective layers. In the equation above, γ is the Grüneisen parameter and K_S is the adiabatic bulk modulus (e.g., Anderson 1989). Here the iron core is assumed to be fully convective (i.e., adiabatic) whereas the silicate mantle and the ice layers are semi-convective. "Fluid" H_2O layers are adiabatic (Fu et al. 2010).

The adiabatic bulk modulus in Equation (A6) can be written as

$$K_S = (1 + \alpha\gamma T)\,K_T, \tag{A7}$$

where $K_T = \rho\,(\partial P/\partial\rho)_T$ is the isothermal bulk modulus and

$$\alpha = \left(\frac{1}{K_T}\right)\left(\frac{\partial P}{\partial T}\right)_\rho \tag{A8}$$

is the thermal expansivity (Anderson 1989). The expansivity is often approximated to a parameterized function $\alpha = \alpha(\rho, T)$ (e.g., Reynard & Price 1990; Frank et al. 2004). These thermodynamical quantities relate to the specific heat at constant pressure and volume, C_P and C_V, according to $\gamma\rho C_P = \alpha K_S$ and $C_P K_T = C_V K_S$.

If the heat flux carried via convection is written as $Q_{\rm conv} = -4\pi\rho R^2 k_v\,[\partial T/\partial m - (\partial T/\partial m)_S]$ (e.g., Sasaki & Nakazawa 1986; Abe 1997), then in Equation (A4)

$$N_u k_c = \frac{(k_c + k_v)Q}{Q - 4\pi\rho R^2 k_v\,(\partial T/\partial m)_S}. \tag{A9}$$

The thermal conductivity is, in general, a function of both pressure and temperature. In the metallic core, k_c is only used to determine $Q_{\rm CMB}$ (the heat flux at the core-mantle boundary) and is assumed to be dominated by the electronic contribution, according to the resistivity estimates of de Koker et al. (2012) and Seagle et al. (2013). It is also assumed that electron-phonon scattering and electron-electron scattering equally contribute to the resistivity of

iron (Zhang et al. 2015). In the mantle, k_c combines contributions from lattice vibration (phonons), radiation, and electrons (Hofmeister 1999; van den Berg et al. 2010). In the ice shell, k_c only includes lattice vibration, according to the formulation of Hofmeister (1999).

The coefficient k_v is zero if $|\partial T/\partial m| \leq |(\partial T/\partial m)_S|$. Otherwise, it is taken from the prescription for the eddy thermal diffusivity of Abe (1995, pp. 215-230) and Abe (1997)

$$k_v = \frac{4\pi}{18}\left(\frac{\rho g K_S R^2 \alpha^2 l_{\rm mix}^4}{\gamma\nu}\right)\left[\left(\frac{\partial T}{\partial m}\right)_S - \frac{\partial T}{\partial m}\right], \quad \text{(A10)}$$

which is based on a modified mixing length theory of thermal convection (Sasaki & Nakazawa 1986). In Equation (A10), $l_{\rm mix}$ plays the role of a mixing length (Tachinami et al. 2011). Although not indicated above, the coefficient k_v also includes a prescription for the limit of a vanishing viscosity (Abe 1997), when $(\partial T/\partial m)_S - \partial T/\partial m > 81\nu^2/(16\pi\rho g\alpha R^2 l_{\rm mix}^4)$, in which k_v becomes independent of ν (Abe 1995, pp. 215-230). Estimates of $\nu = \nu(P,T)$, when available, are affected by large uncertainties. Stamenković et al. (2011) presented a parametrization for the viscosity of perovskite in the diffusion creep regime, and argued that it also provides a reasonable approximation to the viscosity of the ppv phase. That parametrization is applied in the calculations to the entire silicate mantle. For the Earth test discussed here, the dynamical viscosity ($\nu\rho$) of the mantle ranges from $\sim 10^{20}$ to $\sim 10^{23}$ Pa s, in accord with the inferred values in the Earth's mantle (Stamenković et al. 2011; Wagner et al. 2012). The complex rheology of ice, especially of the low-pressure phases, (e.g., Barr & Showman 2009, and references therein), is not meant to be fully accounted for in these calculations. For the purpose of the semi-convection scheme, ice viscosity is assumed to be dominated either by diffusion or by dislocation creep, according to the parametrization of Durham & Stern (2001).

The system of Equations (A1)-(A5) is closed by equations of state (EoS) of the type $P = P(\rho, T)$, written as

$$P(\rho,T) = P(\rho, 300\,{\rm K}) + \Delta P_{\rm th}(\rho,T). \quad \text{(A11)}$$

The first term on the right-hand side is a room-temperature EoS, listed in Table 6, whereas the second term accounts for thermal corrections. The last entry in Table 6 represents the revised release of the 1995 EoS for ordinary water from the International Association for the Properties of Water and Steam (IAPWS, Wagner & Pruß 2002), which already includes temperature dependence and therefore does not apply the second term on the right-hand side of Equation (A11). The EoS in Table 6 are valid up to pressures of at most a few to several times 100 GPa (e.g., Seager et al. 2007; Wagner et al. 2011), which are easily exceeded in the deep interiors of super-Earths. (The inferred pressure at the center of the Earth is ≈ 360 GPa, e.g., Dziewonski & Anderson 1981.) Therefore, following Seager et al. (2007), each EoS is extended by extrapolation to larger pressures until they intersect the zero-temperature EoS of Zapolsky & Salpeter (1969), which is based on the augmented formulation of the Thomas-Fermi-Dirac (TFD) theory of Salpeter & Zapolsky (1967). In the high-pressure regime, where the TDF EoS is employed, finite-temperature corrections are not expected to be important at the densities and temperatures encountered in these calculations (e.g., Cowan & Ashkin 1957; de Carvalho et al. 2014; Boshkayev et al. 2016). It should be pointed out that the Generalized Rydberg EoS applied here to the high-pressure phases of iron and silicate is especially well suited to extrapolation at large pressures (see, e.g., Stacey & Davis 2008; Wagner et al. 2011). All of the relevant EoS functions in Table 6 intersect the corresponding TDF EoS.

In general, $\Delta P_{\rm th}$ in Equation (A11) is a correction based on quasi-harmonic lattice vibration, according to the Mie-Grüneisen-Debye theory (e.g., Anderson 1989; Jackson & Rigden 1996; Stacey & Davis 2008)

$$\Delta P_{\rm th} = \gamma\rho\left[E_{\rm th}(\rho,T) - E_{\rm th}(\rho, 300\,{\rm K})\right], \quad \text{(A12)}$$

where the specific internal energy is

$$E_{\rm th}(\rho,T) = 9n\left(\frac{k_{\rm B}T}{\mu m_{\rm H}}\right)\left(\frac{T}{\theta_{\rm D}}\right)^3 \int_0^{\theta_{\rm D}/T} \frac{\xi^3 d\xi}{e^\xi - 1}, \quad \text{(A13)}$$

in which the Debye temperature $\theta_{\rm D}$ is related to the Grüneisen parameter by

$$\gamma = \left(\frac{\partial \ln\theta_{\rm D}}{\partial \ln\rho}\right)_T. \quad \text{(A14)}$$

In the high-temperature limit, i.e., for liquids, $\theta_{\rm D}/T \ll 1$ (Stixrude & Bukowinski 1990) and Equation (A13) becomes $E_{\rm th}(T) \approx 3nk_{\rm B}T/(\mu m_{\rm H})$. Typically $\theta_{\rm D}$ is derived via integration of Equation (A14) once a suitable expression for γ is known (e.g., Al'tshuler et al. 1987). Here γ, and hence $\theta_{\rm D}$, is typically a function of ρ only and its dependence on T is neglected (see Anderson 1995). However, for the IAPWS EoS, a fit to the specific heat at constant volume, $C_V = C_V(\rho,T)$, is also made available. In this case, the Grüneisen parameter is calculated as $\gamma = \alpha K_T/(\rho C_V)$, and hence depends on both ρ and T (α and K_T are directly calculated from the EoS). Note that, in Equation (A13), the mean molecular weight of the substance, μ, is expressed in units of the hydrogen mass, $m_{\rm H}$, and that $\mu m_{\rm H}/n$ times the Avogadro's number is the mean atomic molar mass. In the metallic core, $\Delta P_{\rm th}$ also accounts for anharmonic vibration and electronic corrections (Dewaele et al. 2006; Ichikawa et al. 2014).

Table 6 provides the sources for most of the the data needed in the structure calculations. At pressures of $P \gg 100$ GPa, the values of most thermodynamics functions are unknown. Uncertainty also affects their behavior at lower pressures but at temperatures of $T \gg 1000$ K. Given the lack of information, the functions are simply extrapolated both in P and T, as needed.

Since ex situ models of Kepler 11 planets contain large amounts of H_2O, whose high-pressure behavior has been studied via both experiments and quantum molecular dynamics computations, the H_2O EoS was compared to some available data. (The IAPWS EoS, applied at $P \lesssim 1$ GPa, is a many-parameter fit to an extensive body of data, Wagner & Pruß 2002.) In the pressure range between ≈ 50 and $\approx 4\times10^3$ GPa, where the transition to the TFD EoS occurs, the cold EoS of the high-pressure H_2O phases differs by only a few percent or less from the density-functional theory data reported by Seager et al. (2007). Equation (A11) also reproduces within a few percent margin the liquid water, temperature-dependent EoS of Abramson & Brown (2004). In more extreme regimes, French et al. (2009) reported on computations of H_2O EoS that account for temperature dependence at high pressures. The finite-temperature correction scheme applied here produces densities that typically agree within $\approx 5\%$ of French et al.'s

Table 7
Comparison of Measured and Computed Radii of Solar System Planets and Satellites

Planet/moon	$M/M_\oplus$[a]	$R/R_\oplus$[a]	MoI[b]	(Fe,Si,H_2O)%	$\Delta R/R$[c]	$\Delta R/R$[d]	ΔMoI/MoI[d]
Mercury	0.05527	0.3829	0.3359[i]	$(66.7, 33.3, 0)$[i]	-2×10^{-2}	-6×10^{-3}	-2×10^{-2}
Venus	0.81500	0.9499	0.33	$(23, 77, 0)$[iii]	9×10^{-3}	1×10^{-2}	2×10^{-2}
Earth	1.00000	1.0000	0.3308[ii]	$(32.7, 67.3, 0)$[i]	-8×10^{-3}	-3×10^{-3}	-2×10^{-2}
Moon	0.01230	0.2727	0.3931[i]	$(2, 98, 0)$[iv]	4×10^{-3}	6×10^{-3}	3×10^{-3}
Mars	0.10745	0.5320	0.3635[i]	$(22, 78, 0)$[i]	-3×10^{-3}	2×10^{-3}	-3×10^{-2}
Io	0.01496	0.2859	0.3768[v]	$(15, 85, 0)$[v]	-7×10^{-3}	-5×10^{-3}	-2×10^{-2}
Europa	0.00804	0.2450	0.346 [v]	$(10, 80, 10)$[v]	3×10^{-2}	3×10^{-2}	-5×10^{-2}
Ganymede	0.02481	0.4130	0.3105[v]	$(10, 40, 50)$[v]	5×10^{-3}	6×10^{-3}	-1×10^{-2}
Callisto	0.01802	0.3783	0.3549[v]	$(0, 50, 50)$[v]	7×10^{-3}	3×10^{-2}	-1×10^{-1}
Titan	0.02253	0.4041	0.3414[vi]	$(0, 64, 36)$[vii]	-3×10^{-2}	-6×10^{-3}	-8×10^{-2}
Triton	0.00358	0.2124	0.33	$(0, 72, 28)$[viii]	-5×10^{-2}	2×10^{-2}	-5×10^{-2}

References. — Sohl & Schubert (2007, i); Lunar & Planetary Science (ii); Phillips & Malin (1983, iii); Righter et al. (2006, iv); Sohl et al. (2002, v); Sohl et al. (2014a, vi); Tobie et al. (2005, vii); Sotin & Tobie (2004, viii).

[a] From JPL Solar System Dynamics.
[b] Moment of inertia factor.
[c] Results from simplified structure models.
[d] Results from improved structure models.

tabled data for all pressures (up to 10^4 GPa) and temperatures (up to 2.4×10^4 K).

At high pressures ($P \gtrsim 50$ GPa) and temperatures ($T \gtrsim 1500$ K) H_2O should transition to a superionic phase, in which oxygen atoms remain on fixed sites in a lattice while hydrogen atoms can diffuse through the lattice, behaving fluid-like (Redmer et al. 2011). Superionic phases separate fully liquid and fully solid H_2O in the P-T diagram (e.g., Wilson et al. 2013). The phase space of superionic H_2O was identified according to the diagrams of Wilson et al. (2013) and Sun et al. (2015). In superionic phases, it is simply assumed that the EoS of liquid H_2O applies (which, as mentioned above, does reproduce available data at high pressure/temperature).

The structure Equations (A1)-(A5), along with Equation (A11) for each layer, are integrated from $m = 0$ to $m = M_c$ with boundary conditions $R(0) = 0$, $P(0) = P_0$, $Q(0) = 0$, $T(0) = T_0$, $P(M_c) = P_c$, and $T(M_c) = T_c$. The quantities P_0 and T_0 are the central pressure and temperature of the planet, whereas P_c and T_c are the pressure and temperature at the surface $R = R_c$ of the condensed part, i.e., at the bottom of the gaseous envelope, both provided by the envelope structure calculations. The set of equations is numerically solved by means of a suite of implicit/explicit algorithms. In the case of a stiff problem, an algorithm based on backward differentiation formulas (i.e., the Gear method, Gear 1971) is employed. If the problem is non-stiff, the Adams-Moulton method (Hairer et al. 1993) is used instead. If implicit methods encounter difficulties, a variable high-order extrapolation algorithm of variable step-size, based on the Gragg-Bulirsch-Stoer method (Hairer et al. 1993), is used. The marching step (Δm) is self-adaptive and is constrained to be smaller than the smallest of $|\partial \ln Y/\partial m|^{-1}$, computed locally for $Y = (R, Q, P, T)$. The integration is repeated, applying a search algorithm in order to adjust P_0 and T_0, until $P(M_c)$ and $T(M_c)$ are within a few percent ($\lesssim 10\%$ for thermal calculations) of the boundary conditions P_c and T_c.

The core structure calculations used for the ex situ models, discussed in Section 2.2, are simplified in that they use only mass continuity, Equation (A1), and hydrostatic equilibrium, Equation (A2), to compute R_c, imposing the conditions $\partial T/\partial m = \partial Q/\partial m = 0$ ($\Delta P_{\rm th} = 0$). Moreover, they assume that the iron core is entirely made of ϵ-Fe and the H_2O shell of ice VII-X. Here we intend to check how the improved structures (i.e., with thermodynamics and additional material phases) compare to those adopted to construct ex situ models.

Table 7 reports test results from the structures of planets and satellites of the solar system, both in the simplified and improved version. Comparisons are carried out for the radius and the moment of inertia factor (MoI). The simplified models reproduce quite accurately the radii of these bodies. In the tests, as expected, the thermal structure of the improved models provides only minor (and sometimes minute) adjustments to the radius. Nonetheless, the results indicate that the thermal models produce reasonable interior structures. Clearly, the adopted compositional partition into two/three layers represents the single major factor determining the radius and the MoI of these bodies. Of the simulated bodies, it should be noted that the iron mass fraction of the Moon is quite uncertain, yet both models provide a iron core radius of ≈ 350 km, in agreement with detection from seismic analysis (Weber et al. 2011). The MoI of Venus and Triton are undetermined, and the value of 0.33 in Table 7 is assumed as representative of fully differentiated bodies (e.g., Chen et al. 2014). The largest discrepancies are obtained for the MoI of Callisto and Titan, which is likely due to the adopted compositions and complete differentiation assumption. Callisto, for example, may have an intermediate silicate/ice mixed layer atop the silicate core (Sohl et al. 2002). None of the models in Table 7 predicts the presence of the low-pressure α-Fe phase, whereas γ-Fe is predicted in Mercury, Mars, and the satellites. Therefore, only the high-pressure and liquid phases of iron are expected in the condensed part of the Kepler 11 planets discussed above.

B. AN EARTH'S MODEL

Figure 18 displays a more detailed comparison of the improved structure model of the Earth (solid line), compared to the Preliminary Reference Earth Model (PREM,

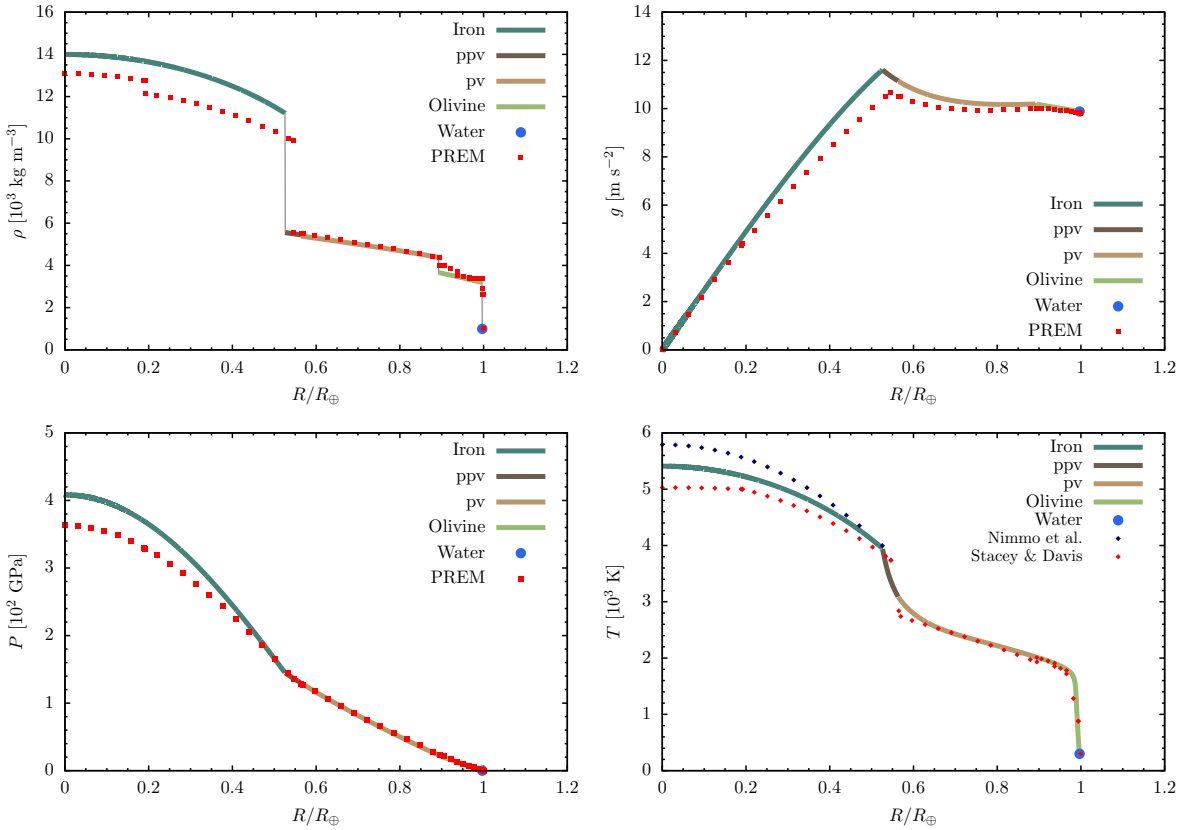

Figure 18. Thermal structure calculation of the Earth's interior compared to the density (top-left), gravitational acceleration (top-right), and pressure (bottom-left) of the Preliminary Reference Earth Model (PREM, Dziewonski & Anderson 1981). The temperature stratification (bottom-right) is compared to the geotherm of Stacey & Davis (2008) and to the core adiabat of Nimmo et al. (2004). See the text for additional details.

Table 8
Structure Properties of the Condensed Part of Kepler 11 Planets

Planet	$M_c/M_\oplus$	(Fe,Si,H_2O)%	$R_c/R_\oplus$ [a]	MoI[a]	$R_c/R_\oplus$ [b]	MoI[b]	$Q_c/Q_\oplus$ [b]
b	2.10	(10.6, 50.6, 38.8)	1.47	0.300	1.55	0.281	0.50
c	4.56	(6.6, 46.5, 46.9)	1.84	0.306	1.87	0.301	0.69
d	5.58	(6.0, 46.0, 48.0)	1.93	0.310	1.94	0.308	0.77
e	6.90	(5.7, 45.7, 48.6)	2.00	0.316	2.01	0.316	0.90
f	2.74	(6.1, 46.1, 47.8)	1.62	0.310	1.62	0.310	0.53
g	5.57	(5.0, 45.0, 50.0)	1.92	0.315	1.93	0.314	0.75

[a] Simplified structure models.
[b] Improved structure models.

Dziewonski & Anderson 1981) and to the geotherm of Stacey & Davis (2008), represented as red squares and diamonds respectively (see the legend). The structure calculation in the figure also includes an "ocean" layer (see the top-left panel), 0.0234% water by mass (Stacey & Davis 2008). The agreement is generally good, with the largest differences confined to the metallic core.

Mantle semi-convection successfully reproduces the temperature gradient in the Earth's outer layers (see also Turcotte & Schubert 2014) and in the mantle in general. The temperature at the CMB is ≈ 3900 K, in accord with current estimates (Alfè et al. 2007; Kamada et al. 2012). The discrepancies in pressure and density in the core are expected (see also Valencia et al. 2006; Wagner et al. 2011) since only pure iron is considered and the presence of lighter elements, such as H, O, Si, and S (e.g., Alfè et al. 2007; Vočadlo 2015, pp. 117-147), is neglected[6]. These impurities are believed to reduce the core density by roughly 7% relative to that of pure iron, at the same conditions of pressure and temperature (Alfè et al. 2007). The inner part of the metallic core is believed to be less polluted than is the outer (liquid) part. The calculated core radius is 3.7% smaller than predicted by the PREM, $R = 3480$ km. The absence of iron alloyed with lighter elements also prevents the formation of an outer molten core. In fact, the melting temperature of Fe at the CMB pressure of ≈ 135 GPa is around 4200 K (Anzellini et al. 2013), whereas the melting temperature at that pressure of, e.g., iron sulfide (FeS) is around 3200 K (Anderson & Ahrens 1996). A calculation conducted with the Vinet EoS for ϵ-Fe of Anderson et al. (2001) yields core pressures, temperature, and densities

[6] It is also estimated that the Earth's core may contain up to about 10% Ni by mass (Vočadlo 2015, pp. 117-147).

that differ by $\lesssim 1\%$ from those in Figure 18.

Core temperatures are quite uncertain, with suggested maximum values ranging up to ≈ 6000 K, and maybe above (Sola & Alfè 2009; Anzellini et al. 2013). As a reference, the bottom-right panel also shows the core adiabat of Nimmo et al. (2004), anchored at the CMB temperature. Again, the general agreement indicates that the thermal model performs reasonably well.

C. THERMAL STRUCTURES OF THE SOLID INTERIORS OF KEPLER 11 PLANETS

As mentioned above, at least $\approx 80\%$ of Kepler 11 planets' total mass consists of condensed material, hence the importance of the condensed structure of the planets in determining their radii. In this appendix, the radii and moment of inertia factors derived from isothermal models of the condensed interiors, applied in the main text, are compared to those derived from the improved structure models described in Appendix A. It should be pointed out that not all condensed layers of the simulated planets are in a solid phase, as liquid iron and liquid/superionic H_2O may exist as well. Results from this comparison are listed in Tables 8.

In order to asses the impact of interior thermodynamics, the structure of the cores of the simulated planets was recalculated applying core-envelope boundary pressures and temperatures (P_c and T_c) obtained from the ex situ calculations discussed in Section 4, at the age of 8 Gyr (see Figure 19). The pressure P_c ranges from ≈ 3 to ≈ 30 GPa, whereas the temperature T_c is between a little over 500 and ≈ 1500 K. Clearly, the values are unconstrained in the case of Kepler 11b, since no light-element envelope is present at 8 Gyr. However, assuming the presence of a relatively thick steam atmosphere, the values $P_c = 1$ GPa and $T_c = 1100$ K are applied. The differences between thermal and isothermal core radii are small, less than 0.5% in most cases and somewhat less than 2% for Kepler 11c. The addition of thermal pressure, the second term on the right-hand side of Equation (A11), tends to reduce density and increase R_c. However, there are additional effects to consider when comparing the two types of models. For example, H_2O in isothermal cores is all in condensed form, whereas the liquid and superionic phases are, in fact, predominant in thermal models.

The case of Kepler 11b is more difficult to evaluate. The choice of P_c and T_c (stated above) leads to a 5% larger R_c, compared to its isothermal counterpart. Upward and downward variations of a factor of two in boundary pressure produce a total change in core radius $\Delta R_c \approx 0.05\, R_\oplus$. If a thinner steam atmosphere could account for the observed radius, assuming a near-isothermal structure at the equilibrium temperature, $T_c \approx T_{\rm eq} \approx 820$ K, a boundary pressure $P_c \approx 0.1$ GPa would still provide a core radius only about 5% larger than that in Table 8 (and $\approx 10\%$, $\approx 0.15\, R_\oplus$, larger than the isothermal radius). Significantly more inflated cores, and H_2O shells in particular, would require much thinner atmospheres (e.g., $R_c \approx 1.76\, R_\oplus$ for $P_c \approx 25$ MPa, see also Thomas & Madhusudhan 2016), although it is not clear whether this possibility is relevant to Kepler 11b.

The results of Table 8 also indicate that the moment of inertia at 8 Gyr is well approximated by isothermal models. The last column lists the energy flux at the core surface, Q_c, normalized to the average surface flux of the Earth, $Q_\oplus = 8.7 \times 10^{-2}\,{\rm W\,m^{-2}}$ (Turcotte & Schubert 2014). As explained above, these values are based on radiogenic heating rates in the planets' silicate mantles estimated for the Earth (at its present age). The total energy output of the cores, $4\pi R_c^2 Q_c$, is negligible compared to the luminosities reported in Table 4. Experiments conducted on Kepler 11b and e with heating rates reduced by a factor of two ($\varepsilon = 3.7 \times 10^{-12}\,{\rm W\,kg^{-1}}$) resulted in very similar interiors (R_c and the MoI factor differing by $\lesssim 0.3\%$, P and ρ at $R = 0$ differing by $\lesssim 1\%$, and T at $R = 0$ differing by 1–2%). The surface heat flux, Q_c, was instead reduced by a factor of ≈ 1.8.

Figure 19 shows some structural properties of Kepler 11 condensed interiors at 8 Gyr. The density, gravitational acceleration, pressure, and temperature are plotted along with the PREM and the reference geotherm of Stacey & Davis (2008), as indicated in the legends of the top panels. As mentioned above, the core temperatures of the Earth may actually be higher. The temperature at the inner core boundary of the Earth ($P \approx 330$ GPa, $R = 1221$ km, Dziewonski & Anderson 1981) was estimated to be 6230 ± 500 K (Anzellini et al. 2013), based on an experimental determination of the melting curve of Fe (though uncertainties persist, e.g., Alfè 2009; Aquilanti et al. 2015; Vočadlo 2015, pp. 117-147).

The iron nucleus of all simulated planets is in the solid phase. The interior models of Figure 12, however, have totally or partially molten nuclei at early isolation times, $t \lesssim 50$–100 Myr. Moreover, if iron in the nucleus was alloyed with lighter elements (such as sulfur or oxygen), a significant volume fraction would likely be in the liquid phase, due to lower melting temperatures (e.g., Anderson & Ahrens 1996; Sotin et al. 2007; Morard et al. 2014). It is also likely that the presence of iron alloys would cause a (partially) molten nucleus in (at least some of) the planets at 8 Gyr. For example, the CMB pressures of Kepler 11b and f are ≈ 300 and ≈ 370 GPa, respectively. The melting temperature of FeS at these pressures is between ≈ 4000 and ≈ 4300 K (Anderson & Ahrens 1996), lower than the calculated CMB temperatures of those planets. It should be stressed, though, that sulfur and oxygen are among the impurities that produce the largest depression of the melting curve compared to that of pure iron (Terasaki & Fischer 2016).

The silicate mantles contain only the high-pressure phases perovskite (pv) and post-perovskite (ppv). In fact, the transition between olivine and perovskite happens at pressures around 23 GPa (for $T \approx 2000$ K, Fei et al. 2004), whereas pressures at the bottom of the H_2O shell are in excess of 60 GPa. For the largest planets Kepler 11c, d, e, and g, the pressure at the base of the H_2O shell is $\gtrsim 160$ GPa, so that ppv is the only phase present in their silicate mantles. Post-post-perovskite phases are predicted for $P \gtrsim 900$ GPa (Wagner et al. 2012), a value reached only at the bottom of the mantle of Kepler 11e (although the stability field of post-ppv phases is also determined by temperature, Stamenković et al. 2011). The H_2O shell is mostly in fluid/superionic phase, except for the presence of ice VII layers in the outer parts of Kepler 11c, d and f.

The interior structures in Figure 19 can be qualitatively compared to those presented by Wagner et al. (2012, , see their Figure 1), since the structural and thermal model applied here share a number of similarities to theirs. However, a detailed comparison is not possible. They considered super-Earths with an Earth-like composition and Earth-like conditions at the surface. Masses are also dif-

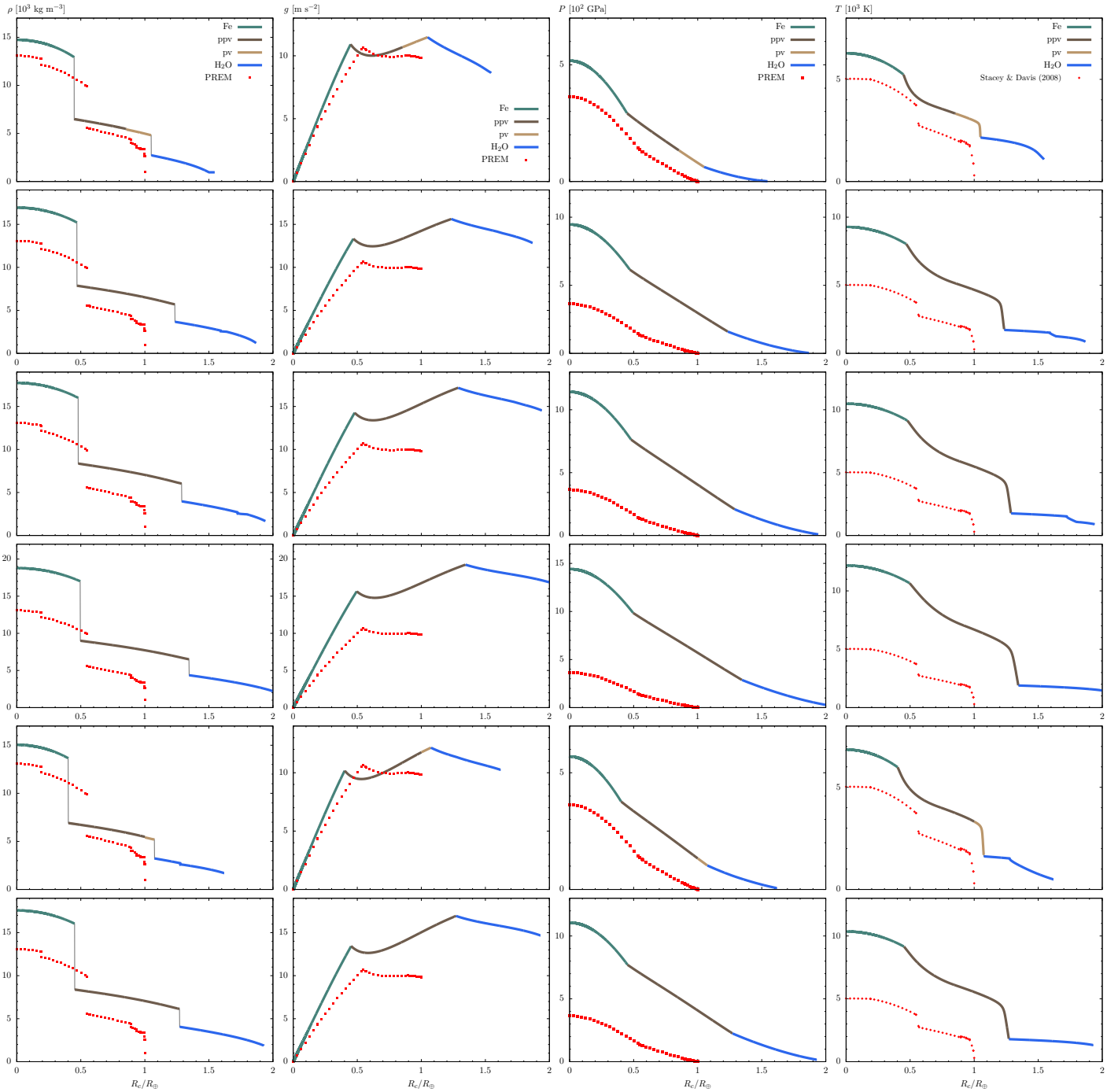

Figure 19. Thermal structure calculations of the condensed cores of Kepler 11 planets at an age of 8 Gyr. See the text for further details. Each row of panels illustrates the stratification of density (left), gravitational acceleration (center-left), pressure (center-right), and temperature (right). From top to bottom, the panels refer to the interiors of Kepler 11b through g.

ferent from those of Kepler 11 planets. Because of the assumed composition, their planets have radii smaller than those obtained here, for similar core masses. Consequently, their central pressures are higher, $\propto M_c^2/R_c^4$. Mantle temperatures are different, which could depend on the boundary conditions at the surface, on the presence of the H_2O shell, and on the behavior of semi-convection in the outer layers of the silicate mantles. In fact, these layers behave as a stagnant lid, in which heat is mainly transported via conduction. The temperature gain across the lid typically accounts for 20–30% of the temperature gain across the entire mantle. The details of the temperature gradient in the lid depend on the thermal conductivity k_c, which is still poorly constrained in the high-pressure and temperature ranges of pv and ppv phases (e.g., see the discussion in van den Berg et al. 2010; Stamenković et al. 2011; Hunt et al. 2012; Wagner et al. 2012). Heat transport becomes more efficient as convection grows more and more vigorous with depth, underneath the stagnant lid. However, details of mantle convection depend on the assumed viscosity parametrization, which is different between the two studies.

The temperatures deep down in the mantles may exceed the melting temperatures of silicates so that, instead

of Equation (A4), the adiabatic temperature gradient in Equation (A5) would apply to those layers. The P–T curves of the mantles in Figure 19 were compared to the high-pressure melting curve of silica (SiO_2) recently determined by Millot et al. (2015) via shock-compression experiments. It was found that in none of the planets' mantles the temperature rises above the melting point. The situation may be different at earlier epochs, though, before the planets cool down. In the case of Kepler 11e, it was found that over most of the evolution in isolation, $t \gtrsim 0.2$ Gyr, mantle temperatures lie below the melting curve. At earlier times, however, the mantle is entirely molten (according to the experiments of Millot et al. 2015) and, hence, it may be approximated as adiabatic. For the less massive planets, Kepler 11c and f, mantle temperatures drop below the melting curve at earlier times, $t \approx 20$–30 Myr.

Figure 12 shows that the condensed cores of Kepler 11 planets formed ex situ (i.e., with significant H_2O content) can undergo substantial contraction during the early stages of evolution in isolation. By $t \approx 0.5$ Gyr, however, the cores are within a few percent of their current radii in Table 8. As mentioned in Section 4.3, almost all of the contraction takes place in the outer H_2O shells, and only 6–8% of the total difference ΔR_c shown in Figure 12 is caused by the contraction of nucleus and mantle. In fact, assuming that the condensed core of Kepler 11g (which undergoes a contraction corresponding to $\Delta R_c \approx 0.34\, R_\oplus$) was 30% Fe and 70% Si by mass, the difference in radii between $t \approx 5$ Myr and ≈ 8 Gyr would be only $\Delta R_c = 0.03\, R_\oplus$! The average gravitational energy per unit time released by the contraction of the cores in Figure 12, during the first 1 Gyr of evolution, is $\approx 10^{-11}\, L_\odot$, becoming much smaller during the following 7 Gyr.

REFERENCES

Abe, Y. 1995, in The Earth's Central Part: Its Structure and Dynamic, ed. T. Yukutake (Tokyo: Terra Scientific Publishing Company), 215–230 26
Abe, Y. 1997, Physics of the Earth and Planetary Interiors, 100, 27 25, 26
Abramson, H. E., & Brown, M. J. 2004, Geochimica et Cosmochimica Acta, 68, 1827 26
Alexander, R. D., & Armitage, P. J. 2007, MNRAS, 375, 500 8
Alfè, D. 2009, Phys. Rev. B, 79, 060101 29
Alfè, D., J., G. M., & Price, G. D. 2007, Contemporary Physics, 48, 63 28
Al'tshuler, L., Brusnikin, S., & Kuz'menkov, E. 1987, Journal of Applied Mechanics and Technical Physics, 28, 129 26
Anderson, D. L. 1989, Theory of the Earth (Oxford, UK: Blackwell Scientific Publications) 25, 26
Anderson, O. L. 1995, Equations of State of Solids for Geophysics and Ceramic Science (New York: Oxford University Press) 26
Anderson, O. L., Dubrovinsky, L., Saxena, S. K., & LeBihan, T. 2001, Geophysical Research Letters, 28, 399 28
Anderson, W. W., & Ahrens, T. J. 1996, Journal of Geophysical Research: Solid Earth, 101, 5627 28, 29
Anzellini, S., Dewaele, A., Mezouar, M., Loubeyre, P., & Morard, G. 2013, Science, 340, 464 25, 28, 29
Aquilanti, G., Trapananti, A., Karandikar, A., Kantor, I., Marini, C., Mathon, O., Pascarelli, S., & Boehler, R. 2015, Proceedings of the National Academy of Sciences of the United States of America, 112, 12042 29
Artymowicz, P. 1993, ApJ, 419, 166 8
Asplund, M., Grevesse, N., Sauval, A. J., & Scott, P. 2009, ARA&A, 47, 481 5
Barr, A. C., & Showman, A. P. 2009, in Europa, ed. R. T. Pappalardo, W. B. McKinnon, & K. K. Khurana (Tucson, AZ: University of Arizona Press), 405 26
Baruteau, C., Crida, A., Paardekooper, S.-J., Masset, F., Guilet, J., Bitsch, B., Nelson, R., Kley, W., & Papaloizou, J. 2014, in Protostars and Planets VI, ed. H. Beuther, R. S. Klessen, C. P. Dullemond, & T. Henning (Tucson, AZ: University of Arizona Press), 667–689 1, 8
Baruteau, C., & Papaloizou, J. C. B. 2013, ApJ, 778, 7 2
Batygin, K. 2015, MNRAS, 451, 2589 2
Batygin, K., & Morbidelli, A. 2013, AJ, 145, 1 2
Bodenheimer, P., D'Angelo, G., Lissauer, J. J., Fortney, J. J., & Saumon, D. 2013, Astrophys. J., 770, 120 3, 4
Bodenheimer, P., Hubickyj, O., & Lissauer, J. J. 2000, Icarus, 143, 2 1, 3, 4
Bodenheimer, P., Laughlin, G., Rózyczka, M., & Yorke, H. 2006, Numerical Methods in Astrophysics: An Introduction (Boca Raton, FL: CRC Press, Taylor and Francis Group) 3
Bodenheimer, P., & Lissauer, J. J. 2014, ApJ, 791, 103 1, 3, 4, 9, 22
Bodenheimer, P., & Pollack, J. B. 1986, Icarus, 67, 391 3
Borsato, L., Marzari, F., Nascimbeni, V., Piotto, G., Granata, V., Bedin, L. R., & Malavolta, L. 2014, A&A, 571, A38 1
Boshkayev, K. A., Rueda, J. A., Zhami, B. A., Kalymova, Z. A., & Balgymbekov, G. S. 2016, International Journal of Modern Physics: Conference Series, 41, 1660129 26
Chatterjee, S., & Ford, E. B. 2015, ApJ, 803, 33 1, 2
Chen, E. M. A., Nimmo, F., & Glatzmaier, G. A. 2014, Icarus, 229, 11 27
Chiang, E., & Laughlin, G. 2013, MNRAS, 431, 3444 1, 2, 9, 21
Chiang, E. I., & Goldreich, P. 1999, ApJ, 519, 279 2
Choukroun, M., & Grasset, O. 2007, The Journal of Chemical Physics, 127, 124506 25
Cowan, R. D., & Ashkin, J. 1957, Phys. Rev., 105, 144 26
Cox, J. P. 1968, Principles of Stellar Structure - Vol.1: Physical principles; Vol.2: Applications to Stars (New York: Gordon and Breach) 4
D'Angelo, G., & Bodenheimer, P. 2013, ApJ, 778, 77 3, 4, 7, 23, 24
D'Angelo, G., & Lubow, S. H. 2008, ApJ, 685, 560 3, 4, 7, 8
—. 2010, ApJ, 724, 730 7, 8
D'Angelo, G., Lubow, S. H., & Bate, M. R. 2006, ApJ, 652, 1698 8
D'Angelo, G., & Marzari, F. 2012, ApJ, 757, 50 7
D'Angelo, G., & Podolak, M. 2015, ApJ, 806, 203 4, 5
D'Angelo, G., Weidenschilling, S. J., Lissauer, J. J., & Bodenheimer, P. 2014, Icarus, 241, 298 4, 12, 20
Davis, S. S. 2005, ApJL, 627, L153 12, 21
de Carvalho, S. M., Rotondo, M., Rueda, J. A., & Ruffini, R. 2014, Phys. Rev. C, 89, 015801 26
de Koker, N., Steinle-Neumann, G., & Vlček, V. 2012, Proceedings of the National Academy of Sciences, 109, 4070 25
Deck, K. M., & Batygin, K. 2015, ApJ, 810, 119 2
Delisle, J.-B., Laskar, J., Correia, A. C. M., & Boué, G. 2012, A&A, 546, A71 2
Dewaele, A., Loubeyre, P., Occelli, F., Mezouar, M., Dorogokupets, P. I., & Torrent, M. 2006, Phys. Rev. Lett., 97, 215504 26
Dodson-Robinson, S. E., Willacy, K., Bodenheimer, P., Turner, N. J., & Beichman, C. A. 2009, Icarus, 200, 672 2
Durham, W. B., & Stern, L. A. 2001, Annual Review of Earth and Planetary Sciences, 29, 295 26
Durisen, R. H., Boss, A. P., Mayer, L., Nelson, A. F., Quinn, T., & Rice, W. K. M. 2007, in Protostars and Planets V, ed. B. Reipurth, D. Jewitt, & K. Keil (Tucson, AZ: University of Arizona Press), 607–622 21, 22
Dziewonski, A. M., & Anderson, D. L. 1981, Physics of the Earth and Planetary Interiors, 25, 297 26, 28, 29
Erkaev, N. V., Kulikov, Y. N., Lammer, H., Selsis, F., Langmayr, D., Jaritz, G. F., & Biernat, H. K. 2007, A&A, 472, 329 5
Fabrycky, D. C., Lissauer, J. J., Ragozzine, D., Rowe, J. F., Steffen, J. H., Agol, E., Barclay, T., Batalha, N., Borucki, W., Ciardi, D. R., Ford, E. B., Gautier, T. N., Geary, J. C., Holman, M. J., Jenkins, J. M., Li, J., Morehead, R. C., Morris, R. L., Shporer, A., Smith, J. C., Still, M., & Van Cleve, J. 2014, ApJ, 790, 146 2
Fei, Y., Mao, H., & Hemley, R. J. 1993, The Journal of Chemical Physics, 99, 5369 25
Fei, Y., Van Orman, J., Li, J., van Westrenen, W., Sanloup, C., Minarik, W., Hirose, K., Komabayashi, T., Walter, M., & Funakoshi, K. 2004, Journal of Geophysical Research: Solid Earth, 109, B02305 25, 29
Ferguson, J. W., Alexander, D. R., Allard, F., Barman, T., Bodnarik, J. G., Hauschildt, P. H., Heffner-Wong, A., & Tamanai, A. 2005, ApJ, 623, 585 3, 7
Figueira, P., Marmier, M., Boué, G., Lovis, C., Santos, N. C., Montalto, M., Udry, S., Pepe, F., & Mayor, M. 2012, A&A, 541, A139 1
Fortes, A. D., Wood, I. G., Alfredsson, M., Vočadlo, L., & Knight, K. S. 2005, Journal of Applied Crystallography, 38, 612 25
Frank, M. R., Fei, Y., & Hu, J. 2004, Geochimica et Cosmochimica Acta, 68, 2781 25
Freedman, R. S., Marley, M. S., & Lodders, K. 2008, ApJS, 174, 504 3, 9
French, M., Mattsson, T. R., Nettelmann, N., & Redmer, R. 2009, Phys. Rev. B, 79, 054107 26
Fu, R., O'Connell, R. J., & Sasselov, D. D. 2010, ApJ, 708, 1326 25
Gear, G. W. 1971, Numerical Initial Value Problems in Ordinary Differential Equations (Englewood Cliffs, NJ: Prentice-Hall) 27
Ginzburg, S., Schlichting, H. E., & Sari, R. 2016, ApJ, 825, 29 1, 6
Goldreich, P., & Schlichting, H. E. 2014, AJ, 147, 32 1, 2
Gorti, U., Dullemond, C. P., & Hollenbach, D. 2009, ApJ, 705, 1237 8
Gorti, U., & Hollenbach, D. 2009, ApJ, 690, 1539 8
Greenzweig, Y., & Lissauer, J. J. 1990, Icarus, 87, 40 4

—. 1992, Icarus, 100, 440 4
Guillot, T. 2010, A&A, 520, A27 4
Hadden, S., & Lithwick, Y. 2014, ApJ, 787, 80 1
Hairer, E., Nørsett, S. P., & Wanner, G. 1993, Solving Ordinary Differential Equations I: Nonstiff Problems (Berlin: Springer) 7, 27
Hands, T. O., Alexander, R. D., & Dehnen, W. 2014, MNRAS, 445, 749 1, 13, 24
Hansen, B. M. S., & Murray, N. 2012, ApJ, 751, 158 1, 2
—. 2013, ApJ, 775, 53 1
Hayashi, C. 1981, Progress of Theoretical Physics Supplement, 70, 35 9, 21
Hofmeister, A. M. 1999, Science, 283, 1699 26
Hollenbach, D., Johnstone, D., Lizano, S., & Shu, F. 1994, ApJ, 428, 654 8
Howard, A. W., Marcy, G. W., Johnson, J. A., Fischer, D. A., Wright, J. T., Isaacson, H., Valenti, J. A., Anderson, J., Lin, D. N. C., & Ida, S. 2010, Science, 330, 653 2
Hubeny, I. 1990, ApJ, 351, 632 7
Hubickyj, O., Bodenheimer, P., & Lissauer, J. J. 2005, Icarus, 179, 415 3, 9, 19
Hunt, S. A., Davies, D. R., Walker, A. M., McCormack, R. J., Wills, A. S., Dobson, D. P., & Li, L. 2012, Earth and Planetary Science Letters, 319320, 96 30
Ichikawa, H., Tsuchiya, T., & Tange, Y. 2014, Journal of Geophysical Research: Solid Earth, 119, 240 25, 26
Ida, S., & Lin, D. N. C. 2004, ApJ, 604, 388 7
Iglesias, C. A., & Rogers, F. J. 1996, ApJ, 464, 943 3
Ikoma, M., & Hori, Y. 2012, ApJ, 753, 66 1, 6
Jackson, I., & Rigden, S. M. 1996, Physics of the Earth and Planetary Interiors, 96, 85 26
Kamada, S., Ohtani, E., Terasaki, H., Sakai, T. a. M., Ohishi, Y., & Hirao, N. 2012, Earth and Planetary Science Letters, 359, 26 28
Katsura, T., Shatskiy, A., Manthilake, G., Zhai, S., Fukui, H., Yamazaki, D., Matsuzaki, T., Yoneda, A., Ito, E., Kuwata, A., Ueda, A., Nozawa, A., & Funakoshi, K. 2009a, Physics of the Earth and Planetary Interiors, 174, 86 25
Katsura, T., Yokoshi, S., Kawabe, K., Shatskiy, A., Manthilake, G., Zhai, S., Fukui, H., Hegoda, C., Yoshino, T., Yamazaki, D., Matsuzaki, T., Yoneda, A., Ito, E., Sugita, M., Tomioka, N., Hagiya, K., Nozawa, A., & Funakoshi, K. 2009b, Geophysical Research Letters, 36, L01305 25
Kerley, I. G. 1993, Multiphase Equation of State for Iron, Tech. Rep. SAND93-0027 (Albuquerque, NM, and Livermore, CA: Sandia National Laboratories) 25
Kippenhahn, R., Weigert, A., & Weiss, A. 2013, Stellar Structure and Evolution (Berlin: Springer) 3
Kley, W., & Nelson, R. P. 2012, ARA&A, 50, 211 1, 2, 8
Komabayashi, T., & Fei, Y. 2010, Journal of Geophysical Research: Solid Earth, 115, 1–12 25
Lee, E. J., & Chiang, E. 2015, ApJ, 811, 41 1
Liffman, K. 2003, Publications of the Astronomical Society of Australia, 20, 337 8
Lin, D. N. C., & Papaloizou, J. 1986, ApJ, 309, 846 6
Lin, J.-F., Gregoryanz, E., Struzhkin, V. V., Somayazulu, M., Mao, H.-k., & Hemley, R. J. 2005, Geophysical Research Letters, 32, L11306 25
Lin, J.-F., Militzer, B., Struzhkin, V. V., Gregoryanz, E., Hemley, R. J., & Mao, H.-k. 2004, The Journal of Chemical Physics, 121, 8423 25
Lissauer, J. J., Fabrycky, D. C., Ford, E. B., Borucki, W. J., Fressin, F., Marcy, G. W., Orosz, J. A., Rowe, J. F., Torres, G., Welsh, W. F., Batalha, N. M., Bryson, S. T., Buchhave, L. A., Caldwell, D. A., Carter, J. A., Charbonneau, D., Christiansen, J. L., Cochran, W. D., Desert, J.-M., Dunham, E. W., Fanelli, M. N., Fortney, J. J., Gautier, III, T. N., Geary, J. C., Gilliland, R. L., Haas, M. R., Hall, J. R., Holman, M. J., Koch, D. G., Latham, D. W., Lopez, E., McCauliff, S., Miller, N., Morehead, R. C., Quintana, E. V., Ragozzine, D., Sasselov, D., Short, D. R., & Steffen, J. H. 2011a, Nature, 470, 53 1, 6, 10, 14, 23
Lissauer, J. J., Hubickyj, O., D'Angelo, G., & Bodenheimer, P. 2009, Icarus, 199, 338 3, 9
Lissauer, J. J., Jontof-Hutter, D., Rowe, J. F., Fabrycky, D. C., Lopez, E. D., Agol, E., Marcy, G. W., Deck, K. M., Fischer, D. A., Fortney, J. J., Howell, S. B., Isaacson, H., Jenkins, J. M., Kolbl, R., Sasselov, D., Short, D. R., & Welsh, W. F. 2013, ApJ, 770, 131 1, 6, 9, 10, 12, 14, 16, 18, 23, 24
Lissauer, J. J., Ragozzine, D., Fabrycky, D. C., Steffen, J. H., Ford, E. B., Jenkins, J. M., Shporer, A., Holman, M. J., Rowe, J. F., Quintana, E. V., Batalha, N. M., Borucki, W. J., Bryson, S. T., Caldwell, D. A., Carter, J. A., Ciardi, D., Dunham, E. W., Fortney, J. J., Gautier, III, T. N., Howell, S. B., Koch, D. G., Latham, D. W., Marcy, G. W., Morehead, R. C., & Sasselov, D. 2011b, ApJS, 197, 8 2
Lithwick, Y., & Wu, Y. 2012, ApJL, 756, L11 2
Lodders, K. 2010, in Principles and Perspectives in Cosmochemistry, ed. A. Goswami & B. E. Reddy (Berlin: Springer), 379 5
Lopez, E. D., Fortney, J. J., & Miller, N. 2012, ApJ, 761, 59 1, 5, 12, 17, 23
Loubeyre, P., LeToullec, R., Wolanin, E., Hanfland, M., & Hausermann, D. 1999, Nature, 397, 503 25
Lubow, S. H., & D'Angelo, G. 2006, ApJ, 641, 526 6, 16
Lubow, S. H., & Ida, S. 2011, in Exoplanets, ed. S. Seager (Tucson, AZ: University of Arizona Press), 347–371 8
Lynden-Bell, D., & Pringle, J. E. 1974, MNRAS, 168, 603 6
Masset, F. S., & Casoli, J. 2010, ApJ, 723, 1393 8
McNeil, D. S., & Nelson, R. P. 2010, MNRAS, 401, 1691 1
Menou, K., & Goodman, J. 2004, ApJ, 606, 520 7
Meyer-Vernet, N., & Sicardy, B. 1987, Icarus, 69, 157 7
Migaszewski, C., Słonina, M., & Goździewski, K. 2012, MNRAS, 427, 770 2
Mihalas, D., & Weibel Mihalas, B. 1999, Foundations of Radiation Hydrodynamics (New York: Dover) 7
Millot, M., Dubrovinskaia, N., Černok, A., Blaha, S., Dubrovinsky, L., Braun, D. G., Celliers, P. M., Collins, G. W., Eggert, J. H., & Jeanloz, R. 2015, Science, 347, 418 31
Minton, D. A., & Levison, H. F. 2014, Icarus, 232, 118 8
Morard, G., Andrault, D., Antonangeli, D., & Bouchet, J. 2014, Comptes Rendus Geoscience, 346, 130 29
Mordasini, C., Alibert, Y., Georgy, C., Dittkrist, K.-M., Klahr, H., & Henning, T. 2012, A&A, 547, A112 1
Movshovitz, N., Bodenheimer, P., Podolak, M., & Lissauer, J. J. 2010, Icarus, 209, 616 9
Mullally, F., Coughlin, J. L., Thompson, S. E., Rowe, J., Burke, C., Latham, D. W., Batalha, N. M., Bryson, S. T., Christiansen, J., Henze, C. E., Ofir, A., Quarles, B., Shporer, A., Van Eylen, V., Van Laerhoven, C., Shah, Y., Wolfgang, A., Chaplin, W. J., Xie, J.-W., Akeson, R., Argabright, V., Bachtell, E., Barclay, T., Borucki, W. J., Caldwell, D. A., Campbell, J. R., Catanzarite, J. H., Cochran, W. D., Duren, R. M., Fleming, S. W., Fraquelli, D., Girouard, F. R., Haas, M. R., Helminiak, K. G., Howell, S. B., Huber, D., Larson, K., Gautier, III, T. N., Jenkins, J. M., Li, J., Lissauer, J. J., McArthur, S., Miller, C., Morris, R. L., Patil-Sabale, A., Plavchan, P., Putnam, D., Quintana, E. V., Ramirez, S., Silva Aguirre, V., Seader, S., Smith, J. C., Steffen, J. H., Stewart, C., Stober, J., Still, M., Tenenbaum, P., Troeltzsch, J., Twicken, J. D., & Zamudio, K. A. 2015, ApJS, 217, 31 1
Murray-Clay, R. A., Chiang, E. I., & Murray, N. 2009, ApJ, 693, 23 5
Nimmo, F., Price, G. D., Brodholt, J., & Gubbins, D. 2004, Geophysical Journal International, 156, 363 28, 29
Ogihara, M., Morbidelli, A., & Guillot, T. 2015, A&A, 578, A36 2
Owen, J. E., & Wu, Y. 2016, ApJ, 817, 107 6
Paardekooper, S.-J., Baruteau, C., & Kley, W. 2011, MNRAS, 410, 293 8
Phillips, R. J., & Malin, M. C. 1983, in Venus, ed. D. M. Hunten, L. Colin, T. M. Donahue, an V. I. Moroz (Tucson, AZ: University of Arizona Press), 159–214 27
Pollack, J. B., Hubickyj, O., Bodenheimer, P., Lissauer, J. J., Podolak, M., & Greenzweig, Y. 1996, Icarus, 124, 62 3, 4, 19
Pringle, J. E. 1981, ARA&A, 19, 137 7
Redmer, R., Mattsson, T. R., Nettelmann, N., & French, M. 2011, Icarus, 211, 798 27
Rein, H. 2012, MNRAS, 427, L21 2
Reynard, B., & Price, G. D. 1990, Geophysical Research Letters, 17, 689 25
Ribas, I., Guinan, E. F., Güdel, M., & Audard, M. 2005, ApJ, 622, 680 5
Righter, K., Drake, M. J., & Scott, E. R. D. 2006, in Meteorites and the Early Solar System II, ed. D. S. Lauretta, and H. Y. McSween (Tucson, AZ: University of Arizona Press), 803–828 27
Rogers, L. A., Bodenheimer, P., Lissauer, J. J., & Seager, S. 2011, ApJ, 738, 59 1, 5
Safronov, V. S. 1969, Evolution of the Protoplanetary Cloud and Formation of the Earth and Planets (Moscow: Nauka Press) 1, 4
Salpeter, E. E., & Zapolsky, H. S. 1967, Physical Review, 158, 876 26
Sasaki, S., & Nakazawa, K. 1986, J. Geophys. Res., 91, 9231 25, 26
Saumon, D., Chabrier, G., & van Horn, H. M. 1995, ApJS, 99, 713 3
Schlichting, H. E. 2014, ApJL, 795, L15 2, 9, 21
Seager, S., Kuchner, M., Hier-Majumder, C. A., & Militzer, B. 2007, ApJ, 669, 1279 5, 20, 26
Seagle, C. T., Cottrell, E., Fei, Y., Hummer, D. R., & Prakapenka, V. B. 2013, Geophysical Research Letters, 40, 5377 25
Shakura, N. I., & Sunyaev, R. A. 1973, A&A, 24, 337 12
Siess, L., Dufour, E., & Forestini, M. 2000, A&A, 358, 593 5, 6, 16, 19
Sohl, F., & Schubert, G. 2007, in Treatise on Geophysics, ed. G. Schubert (Amsterdam: Elsevier), 27–68 5, 27
Sohl, F., Solomonidou, A., Wagner, F. W., Coustenis, A., Hussmann, H., & Schulze-Makuch, D. 2014a, Journal of Geophysical Research: Planets, 119, 1013 27
Sohl, F., Spohn, T., Breuer, D., & Nagel, K. 2002, Icarus, 157, 104 25, 27

Sohl, F., Wagner, F. W., & Rauer, H. 2014b, in IAU Symp. 293, Formation, Detection, and Characterization of Extrasolar Habitable Planets, ed. N. Haghighipour (Cambridge: Cambridge University Press), 350 5, 20
Sola, E., & Alfè, D. 2009, Phys. Rev. Lett., 103, 078501 29
Sotin, C., Grasset, O., & Mocquet, A. 2007, Icarus, 191, 337 5, 20, 29
Sotin, C., & Tobie, G. 2004, Comptes Rendus Physique, 5, 769 27
Soubiran, F., & Militzer, B. 2015, ApJ, 806, 228 23
Spada, F., Demarque, P., Kim, Y.-C., & Sills, A. 2013, ApJ, 776, 87 5, 6, 19
Stacey, F. D., & Davis, P. M. 2008, Physics of the Earth (Cambridge, UK: Cambridge University Press) 5, 25, 26, 28, 29
Stamenković, V., Breuer, D., & Spohn, T. 2011, Icarus, 216, 572 25, 26, 29, 30
Stevenson, D. J. 1982, Planet. Space Sci., 30, 755 9
Stewart, S. T., & Ahrens, T. J. 2005, Journal of Geophysical Research: Planets, 110, E03005 25
Stixrude, L., & Bukowinski, M. S. T. 1990, Journal of Geophysical Research: Solid Earth, 95, 19311 25, 26
Sun, J., Clark, B. K., Torquato, S., & Car, R. 2015, Nature Communications, 6, 753 27
Tachinami, C., Senshu, H., & Ida, S. 2011, ApJ, 726, 70 26
Tan, J. C., Chatterjee, S., Hu, X., Zhu, Z., & Mohanty, S. 2015, arXiv:1510.06703 1, 2
Tanaka, H. 1998, The Journal of Chemical Physics, 108, 4887 25
Tanaka, H., Takeuchi, T., & Ward, W. R. 2002, ApJ, 565, 1257 8
Tanaka, H., & Ward, W. R. 2004, ApJ, 602, 388 8
Tateno, S., Hirose, K., Sata, N., & Ohishi, Y. 2009, Earth and Planetary Science Letters, 277, 130 25
Terasaki, H., & Fischer, R. A. 2016, Deep Earth: Physics and Chemistry of the Lower Mantle and Core (Hoboken, NJ: Wiley) 29
Thomas, S. W., & Madhusudhan, N. 2016, MNRAS, 458, 1330 29
Tobie, G., Grasset, O., Lunine, J. I., Mocquet, A., & Sotin, C. 2005, Icarus, 175, 496 27
Turcotte, D. L., & Schubert, G. 2014, Geodynamics (Cambridge, UK: Cambridge University Press) 25, 28, 29
Valencia, D., O'Connell, R. J., & Sasselov, D. 2006, Icarus, 181, 545 5, 20, 25, 28
van den Berg, A. P., D.A. Yuen, D. A., G.L. Beebe, G. L., & Christiansen, M. D. 2010, Physics of the Earth and Planetary Interiors, 178, 136 26, 30
Vočadlo, L. 2015, in Treatise on Geophysics, ed. G. Schubert (Oxford, UK: Elsevier), 117–147 28, 29
Wagner, F. W., Sohl, F., Hussmann, H., Grott, M., & Rauer, H. 2011, Icarus, 214, 366 25, 26, 28
Wagner, F. W., Tosi, N., Sohl, F., Rauer, H., & Spohn, T. 2012, A&A, 541, A103 25, 26, 29, 30
Wagner, W., & Pruß, A. 2002, Journal of Physical and Chemical Reference Data, 31, 387 25, 26
Ward, W. R. 1997, Icarus, 126, 261 2, 7
Watson, A. J., Donahue, T. M., & Walker, J. C. G. 1981, Icarus, 48, 150 5
Weber, R. C., Lin, P.-Y., Garnero, E. J., Williams, Q., & Lognonné, P. 2011, Science, 331, 309 27
Weidenschilling, S. J. 1977, Astrophysics and Space Science, 51, 153 21
Williams, J. P., & Cieza, L. A. 2011, ARA&A, 49, 67 12
Wilson, H. F., Wong, M. L., & Militzer, B. 2013, Phys. Rev. Lett., 110, 151102 27
Winn, J. N., & Fabrycky, D. C. 2015, ARA&A, 53, 409 1
Zapolsky, H. S., & Salpeter, E. E. 1969, ApJ, 158, 809 26
Zhang, P., Cohen, R. E., & Haule, K. 2015, Nature, 517, 605 26